Spring 2019

Developing and evaluating a partition-cavity solar thermochemical reactor for syngas production via computational fluid dynamics

Han Zhang

Department: Chemical and Biochemical Engineering

DEVELOPING AND EVALUATING A PARTITION-CAVITY SOLAR THERMOCHEMICAL REACTOR FOR SYNGAS PRODUCTION VIA COMPUTATIONAL FLUID DYNAMICS

by

HAN ZHANG

A DISSERTATION

Presented to the Faculty of the Graduate School of the

MISSOURI UNIVERSITY OF SCIENCE AND TECHNOLOGY

In Partial Fulfillment of the Requirements for the Degree

DOCTOR OF PHILOSOPHY

in

CHEMICAL ENGINEERING

2019

Approved by:

Dr. Joseph D. Smith, Advisor
Dr. Muthanna H. Al-Dahhan
Dr. Douglas K. Ludlow
Dr. Xinhua Liang
Dr. Fatih Dogan

PUBLICATION DISSERTATION OPTION

This dissertation consists of the following three articles, formatted in the style used by the Missouri University of Science and Technology:

Paper I: Pages 21-62 have been submitted to ***Renewable Energy***.

Paper II: Pages 63-105 have been submitted to ***Solar Energy***.

Paper III: Pages 106-146 are intended for submission to ***Energy***.

ABSTRACT

Solar thermochemical processes are attractive since they have the advantages of storing solar energy as chemical fuels. In this dissertation, a partition-cavity solar thermochemical reactor was developed, and the heat and mass transfer of the solar thermochemical processes were numerically analyzed in this directly-irradiated reactor.

The reduction reaction of two-step $CeO_2/CeO_{2-\delta}$ solar redox process was investigated using the coupling of computational fluid dynamics (CFD) and discrete element method (DEM). The reduction rate was studied based on the catalyst textual properties and the reaction condition. The results revealed that the increase of catalyst specific surface area and the rise of the catalyst temperature are favorable to the reduction of CeO_2.

The geometric factors of the partition-cavity solar thermochemical reactor were investigated with the uniform and concentrated radiant fluxes. The results indicated that a thinner catalyst with an appropriate partition gap size is beneficial for the temperature distribution. The result of the CeO_2 endothermic reduction showed that the larger catalyst loading quantity can derive a higher solar-to-fuel efficiency.

The different periodic open cellular structured (POCS) catalysts were studied in the solar thermochemical reactor for the dry reforming of methane (DRM) process. The heat transfer results revealed that the conduction of the strut is dominant for the temperature distribution in the catalyst region. The diversified shapes of POCS have little influences on the methane conversion under the assumption of equal active sites. Microkinetics with site reactions is promising for a further detailed study.

ACKNOWLEDGMENTS

First of all, I would like to thank Dr. Joseph D. Smith, my Ph.D. advisor, for giving me the precious opportunity to accomplish my Ph.D. in his group. I am very grateful to him for giving me research liberty and trusting my decisions. I thank him for making the time to guide me and share his expertise in hybrid energy systems and process modeling with me, even he is an extremely busy person. I really appreciate him for giving me the chances to present my research in scientific conferences. It has been my greatest honor to work with him.

I sincerely express my gratitude to the rest of my committee members, Dr. Muthanna H. Al-Dahhan, Dr. Fatih Dogan, Dr. Xinhua Liang, and Dr. Douglas Ludlow for their professional suggestions. I would like to thank the faculty and staff in Chemical and Biochemical Engineering department for their help. I would like to acknowledge Ms. Frieda Adams, the former secretary of Energy Research & Development Center. I also want to thank Mrs. Eileen Smith for her help in my writing skills and my life.

I greatly appreciate Dr. Vivek Rao for his help with my research. I also would like to thank my other colleagues in Dr. Smith's group and my friends.

I would like to show my greatest gratitude to my family for their support through my Ph.D. program and in the rest of my life. Finally, I would like to thank Dr. Zeyu Shang, the love of my life, for his unconditional support on my hard times.

TABLE OF CONTENTS

Page

LIST OF ILLUSTRATIONS

SECTION Page

PAPER II

PAPER III

LIST OF TABLES

NOMENCLATURE

Symbol	Description
POCS	Periodic open cellular structure
DRM	Dry reforming of methane
δ	Equilibrium value of non-stoichiometric coefficient of CeO_2
x	Non-equilibrium value of non-stoichiometric coefficient of CeO_2
A_{red}	Pre-exponential factor of reduction
A_{ox}	Pre-exponential factor of oxidation
E_{red}	Activation energy of reduction
E_{ox}	Activation energy of oxidation
α	CeO_2 reduction reaction fraction
$k(T)$	Temperature-dependent reaction rate constant
$f(\alpha)$	Function of reaction fraction
Y_{oxid}	Mole fraction of the oxidant
γ	Reaction order of the oxidant
Ce_{Ce}^{x}	Cerium on the cerium lattice sites
$Ce_{Ce}^{'}$	Electrons on the cerium lattice sites
O_{O}^{x}	Oxygen on the oxygen sites
$V_{O}^{''}$	Oxygen vacancies
K	Equilibrium constant
m	Power-law CH_4 rate coefficient
n	Power-law CO_2 rate coefficient

CFD	Computational fluid dynamics
FDM	Finite difference method
FEM	Finite element method
FVM	Finite volume method
m_i	Particle mass
$\boldsymbol{r}_i$	Particle position
$\boldsymbol{f}_i$	Total contact forces
$\boldsymbol{g}$	Gravitational acceleration
I_i	Moment of inertia
$\boldsymbol{\omega}_i$	Angular velocity
$\boldsymbol{t}_i$	Total torque
κ	Absorption coefficient
β	Extinction coefficient
Φ	Scattering phase function

1. INTRODUCTION

1.1. SOLAR THERMOCHEMICAL PROCESS

Solar energy is an attractive renewable energy source that possesses abundant and ubiquitous power. It is reported the energy provided by solar radiation on the earth surface in one hour is much more than that needed worldwide yearly [1]. Presently, solar photovoltaics (PV) is the most extensive application of solar energy to generate electricity, followed by solar-aided process heat, and residential solar hot water applications [2-4]. As solar energy has apparent intermittency, the ultimate objective is to store it in stable and efficient approaches, like batteries and fuels. Solar thermochemical process provides a promising potential to convert solar energy to chemical fuels, which is beneficial for storage and transportation.

1.1.1. Background of Solar Thermochemical Process. Generally, solar thermochemical processes can be classified as three groups based on the feedstocks and reaction mechanisms for fuel production, which are solar thermolysis, hydrocarbon solar thermochemical processes, solar thermochemical cycles [5]. Solar thermolysis is a conceptual process that directly decomposes water via solar energy. The extremely high reaction temperature (over 2500 K), difficult products separation, and low conversion (less than 5%) are dominant issues that limit its development [6, 7]. Hydrocarbon solar thermochemical processes and solar thermochemical cycles are mainstream study directions in recent decades. Hydrocarbon solar thermochemical processes are mostly solar-aided hydrocarbon reforming processes. One of the representatives is solar methane reforming. Compared with hydrocarbon solar thermochemical processes, solar

thermochemical cycles are favorable on the reactants (carbon dioxide and water). As carbon dioxide is an environmental-unfriendly green gas and water has low economic value, the solar thermochemical cycles provide an opportunity to convert solar energy with low-value gases to salutary chemical fuels, which can be directly used or working as feedstock for further liquid hydrocarbon production [8].

1.1.2. Two-Step Solar Thermochemical Cycles. Solar thermochemical cycles are two-step processes based on metal oxide redox pairs. The first step is oxidized compound endothermic reduction at high temperature and release oxygen. The second step is low-temperature oxidation that reduced compound reacts with carbon dioxide or water to acquire oxygen and oxidized back to the higher-valence state. Carbon dioxide and water in the oxidation step are split into carbon monoxide and hydrogen. The cyclic scheme is presented below:

$$MO_{oxidized} + (\Delta H) \rightarrow MO_{reduced} + 1/2\, O_2 \quad (1)$$

$$MO_{reduced} + CO_2 \rightarrow MO_{oxidized} + CO + (\Delta H) \quad (2)$$

$$MO_{reduced} + H_2O \rightarrow MO_{oxidized} + H_2 + (\Delta H) \quad (3)$$

As metal-oxide is recycled in the process, the net reactions for solar thermochemical cycles are simplified as:

$$CO_2 \rightarrow CO + 1/2\, O_2 \quad (4)$$

$$H_2O \rightarrow H_2 + 1/2\, O_2 \quad (5)$$

The fuel production highly depends on the oxygen yield during metal oxide reduction. The high-valence metal oxide can be reduced to lower-valence oxide or even to metal with zero-valence. Based on this principle, a variety of metal oxide redox pairs are applied in the cycles.

1.1.3. Metal Oxides for Solar Thermochemical Cycles. These metal oxide redox pairs can be typically divided into two types based on their volatilities. The most conspicuous characteristic of volatile redox cycle is that the metal oxide has a solid-to-gas phase transition, due to the higher reduction temperature [9]. Normally, the reduction temperature exceeds metal oxide vaporization temperature, which causes phase conversion. Another feature of volatile redox pairs is the reaction obeys the law of stoichiometry, which means the metal oxide can be reduced to corresponding lower-valence oxide or metal. Some representative redox pairs, including ZnO/Zn [9-12], CdO/Cd [13, 14], SnO_2/SnO [15-18], and GeO_2/GeO [19], can reduce in the temperature range over 1723 K. Due to the phase transition issue, large-scale implementation of volatile redox pairs faces the challenges of separation and recombination, which requires rapid quenching procedures [20]. Nonvolatile redox pairs avoid the phase transition issue during high-temperature reduction. Based on the chemical properties of metal oxides, nonvolatile redox pairs are classified as stoichiometric reactions and nonstoichiometric reactions. In nonvolatile stoichiometric reactions, there is a crystal structure change of metal oxide with a valence reducing of cation, a reduced metal oxide is achieved after reduction [21]. Ferrite systems [22-26] and hercynite systems [27-29] are two representative nonvolatile stoichiometric redox group. As stoichiometric reactions have integer valence change, they have larger oxygen exchange capacity than nonstoichiometric reactions, which is beneficial for fuel production. However, the element stability of metal oxides limits the performances of nonvolatile stoichiometric redox pairs. For example, $Fe^{3+/2+}$ shows unstable and poor thermal properties in ferrites system, which can be solved by adding ceramic materials, such as ZrO_2 or YSZ, but

sacrificing the thermal efficiency [30-33]. Additionally, stoichiometric reactions normally have relatively slower reaction kinetics that is not expected in solar thermochemical cycles [34]. Nonstoichiometric reactions partially reduce metal oxides, like CeO_2 or $LaMnO_3$ perovskites, to form transient state metal oxides without changing crystallographic structures [35-39]. Since the solid structure can be maintained in nonstoichiometric reactions, the morphologic properties, such as pore size, porosity, and specific surface area, can also be preserved for better reaction rates. Even though greater entropy change can be derived in volatile and non-volatile stoichiometric reactions due to the phase change, nonstoichiometric redox pairs still have advantages on solar thermochemical cycles based on the outstanding thermal stability.

1.1.4. Cerium Oxide Redox Pair for Solar Thermochemical Cycles. Cerium dioxide redox pair shows remarkably thermal and chemical properties for solar thermochemical cycles, including stable crystallographic structure, high solid thermal conductivity, and fast redox kinetics, which is recognized as a promising nonstoichiometric material for solar syngas production. The redox reactions for CeO_2 are shown as follows:

$$CeO_2 \rightarrow CeO_{2-\delta} + 0.5\delta O_2 \quad (6)$$

$$CeO_{2-\delta} + \delta CO_2 \rightarrow CeO_2 + \delta CO \quad (7)$$

$$CeO_{2-\delta} + \delta H_2O \rightarrow CeO_2 + \delta H_2 \quad (8)$$

During the last decades, a bunch of studies focused on improving the oxygen exchange capacity and energy conversion efficiency. Chueh et al. [40] initially proposed the results of splitting CO_2 and H_2O via non-stoichiometric CeO_2 redox pair under 1.9 kW simulated solar power for cycling production. The average efficiency is 0.4%

compared with the predicted efficiency of 15% without heat recovery [34]. Furler et al. [41] presented porous CeO_2 felt structure and tested under a 3.6 kW solar simulator. However, the average efficiency is 0.15% caused by inhomogeneous temperature distributions and uneven reaction rate distributions. For the purpose to solve the above issue, Furler et al. [42] further reported an improved CeO_2 reticulated porous ceramic foam structure, which has an efficiency of 1.73% under 3.8 kW power input. As the oxidation kinetics is limited heat and mass transfer in the material, Marxer et al. proposed a dual-scale porous structure, which raises the energy conversion efficiency to 5.25% [43]. Due to the high reduction temperature of CeO_2, transient metal doping is introduced to tune the thermodynamic properties of CeO_2. Presently, Zr^{4+}, La^{3+}, Sm^{3+}, Gd^{3+}, Y^{3+}, Ca^{2+}, Sr^{2+}, and some other elements are reported to use as doping composition of CeO_2 [44-46].

1.1.5. Solar Thermochemical Reactors. Based on the radiation integration mode, solar thermochemical reactors can be divided into indirectly-irradiated reactors and directly-irradiated reactors. The heat transfer type is the distinguishing criteria of indirect-irradiated reactors and irradiated reactor. For indirectly-irradiated reactors, reactants are inside an opaque chamber. Solar radiation can only reach the surface of the opaque wall to increase the temperature. Heat transfer between reactants and the chamber is conduction. Most of the indirectly-irradiated reactors are applied in the area of hydrocarbon solar reforming in tubes, as common tubular reactor materials can afford the reforming temperature [47-49]. Recent years, indirectly-irradiated reactors are also applied to solar thermochemical cycles with double chamber design. In order to suffer

high reduction temperature, some ceramic materials, such as silicon carbide and alumina, are served as opaque tube materials [50, 51].

For the directly-irradiated reactor, the incoming solar radiation can reach the reactants region either directly or through a transparent quartz glass window. Since radiation participates heat transfer in the reactive region, a higher reactants temperature is expected, which is profitable for high-temperature reduction of the solar thermochemical cycle.

Typically, directly-irradiated reactors are categorized as entrained beds, fluidized beds, and packed beds base on the movement of reactants [52]. Entrained beds are one group of the earliest directly-irradiated reactors, which most show as cyclonic geometry with vortex flow paths. It is reported that the cyclonic type reactor can heat up reactants in the range of 1300 K – 1800 K, which is most suitable for reactions that need gas-solid separation [53]. Cyclone geometry and gas injection are two crucial factors that affect reactor performances. Based on the reported work, entrained beds are major applied in volatile solar thermochemical cycles (ZnO/Zn) or methane reforming via ZnO or $CaCO_3$ [54-56]. Fluidized beds have enormous advantages on heat transfer, as the gas-solid contact time and particle residence time are effectively increased [53]. As particles are fluidized in the reactor, it is easier to get homogenous heat transfer between gas and solid, which also leads to a higher temperature. Some directly-irradiated fluidized reactors are developed and applied in the reforming and gasification process. Packed beds are the largest group in directly-irradiated reactors, as such kind of reactors are favorable for solar catalytic reactions, like hydrocarbon reforming and solar thermochemical cycles [52]. Fixed beds, moving front beds, and rotary beds are primary packed beds that have

reported in solar thermochemical cycles. All the directly-irradiated packed beds are based on a cavity-receiver structure, which provides adequate space for receiver radiation. The most remarkable benefit of the rotary reactor is that the axial of the reactants bed is perpendicular to that of the cavity, which enhances the irradiated surface area. Several rotary reactors are proposed for solar thermochemical cycles under 10 – 30 kW input power [57-59]. Moving front beds use a piston to support and push packed bed explore under radiation in the cavity. Generally, this type of reactors is used for volatile redox pairs [60-62], which the solid reactants are consumed, and new reactants need to supplement. Fixed beds are the most common type for laboratory-scale on solar thermochemical processes, as the reactor construction and operation are relatively economical and easy to accomplish. Since fixed beds have stationary reactants space, they are widely used in the study of nonvolatile solar thermochemical cycles. Among the reported fixed bed reactors, the annular CeO2 structured cavity-receiver reactor developed by Chueh et al. [63] shows prominent advantages on radiative absorption surface compared with traditional cylindrical catalyst block.

1.1.6. Modeling of Solar Thermochemical Cycles. The chemical reaction mechanisms of the CeO_2 redox cycles play a crucial role in the modeling of solar thermochemical cycles. Presently, the representative reaction mechanisms can be classified as the equilibrium model, the kinetics based on the Arrhenius equation, and the crystal site relations.

The equilibrium model is a principle which considering the reduction and oxidation of the CeO_2 at the equilibrium state, which the forward and backward reactions have an equal reaction rate. The non-stoichiometric coefficient of CeO_2 is expressed

based on the reaction temperature and oxygen partial pressure. The general expression of the thermodynamic equilibrium model is shown below [64]:

$$\frac{\delta}{x-\delta} = \frac{A_{red}}{A_{ox}} P_{O_2}^{-n} \exp\left(\frac{-(E_{red}-E_{ox})}{RT}\right) \quad (9)$$

where δ is the equilibrium value of the deviation from stoichiometry of CeO_2, x is the studied deviation from stoichiometry of CeO_2, A_{red}, A_{ox}, E_{red}, and E_{ox} are the pre-exponential factor and the activation energy for the reduction and oxidation reactions. Bulfin et al. [64] experimentally studied parameters in the above equation and the results showed a satisfactory agreement with the equilibrium values in the literature [65].

The chemical reaction kinetic model is one of the initial models that have been investigated for the CeO_2 reduction reaction. Ishida et al. [66] proposed the basic formula for the CeO_2 reduction rate, which can be represented as:

$$\frac{d\alpha}{dt} = k(T) f(\alpha) \quad (10)$$

where α is the reaction fraction, $k(T)$ is the temperature-dependent rate constant, and $f(\alpha)$ is the function related to the reaction fraction. Based on the selection of the nucleation models, $f(\alpha)$ has various expressions. However, the accuracy of this model needs to be improved due to the coefficient values of the Arrhenius equation. An improved model based on the solid-state kinetic theory [67] was used for the combined reaction rate of the thermochemical cycles, which has the expression as:

$$\frac{d\alpha}{dt} = k(T)[Y_{oxid}(t)]^{\gamma} f(\alpha) \quad (11)$$

where $Y_{oxid}(t)$ is the time-dependent mole fraction of the oxidant, γ is the reaction order of the oxidant. The model accuracy was enhanced by adjusting the parameters in the formula.

The site reaction of CeO_2 reduction can be ideally expressed as [68]:

$$2Ce_{Ce}^{x} + O_{o}^{x} \rightarrow 2Ce_{Ce}' + V_{O}'' + \frac{1}{2}O_2(g) \tag{12}$$

where, Ce_{Ce}^{x}, Ce_{Ce}', O_{o}^{x} and V_{O}'' represent the cerium on the cerium lattice sites, the electrons on the cerium lattice sites, the oxygen on the oxygen sites, and the oxygen vacancies. The reaction rate can be expressed in the form of the enthalpy flux equation on the control interface. The relation is based on the Gibbs free energy. The formula for the equilibrium constant (K) is

$$K = \frac{[Ce_{Ce}']^2[V_{O}'']P_{O_2}^{1/2}}{[Ce_{Ce}^{x}]^2[O_{o}^{x}]} \tag{13}$$

The concentrations of the sites above have relations with the CeO_2 non-stoichiometric coefficient δ. Bader et al. [69] applied this theory in their study of the CeO_2 reduction reaction in a fluidized-bed reactor.

1.2. SOLAR THERMOCHEMICAL DRY REFORMING OF METHANE

1.2.1. Background of Dry Reforming of Methane. The development of natural gas applications is quite flourishing during these years. Methane is a primary component in the natural gas attracts plenty of attention in the direction of producing higher value chemicals. Methane reforming processes are promising in the industrial applications since the syngas is the main product, which can be widely used as the feedstock for the

generation of liquid hydrocarbon chemicals, like Fisher-Tropsch process [70]. Steam reforming and dry reforming are two common types for the methane reforming process distinguished by the different reactants:

$$CH_4 + H_2O \leftrightarrow CO + 3H_2 \quad (14)$$

$$CH_4 + CO_2 \leftrightarrow 2CO + 2H_2 \quad (15)$$

Both the two reforming reactions are an endothermic process. For the dry reforming process, the reverse water-gas shift reaction (RWGS) occurs simultaneously with the CO_2 reforming:

$$CO_2 + H_2 \leftrightarrow CO + H_2O \quad (16)$$

The steam reforming of methane can get a 3:1 ratio of H_2/CO, which is favorable for hydrogen production. However, hydrogen production requires a higher H_2O/CH_4 ratio and a larger energy contribution, which causes the catalyst deactivation [71]. Moreover, the introduction of steam in the process leads to the corrosion issue of the operating units, which is unfavorable to the production [72].

Due to the RWGS, the products ratio of dry reforming of methane (DRM) is slightly lower than 1:1. This lower H_2/CO ratio could increase the C_{5+} selectivity in Fischer-Tropsch synthesis [73, 74]. Besides the advantages of production of higher value chemicals, dry reforming of methane also has a significant environmental benefit for the removal of greenhouse gases.

1.2.2. Solar Thermochemical Dry Reforming of Methane. Due to the dry reforming methane is an endothermic process, solar thermochemical dry reforming process not only provides enough energy for the reaction but also offers an opportunity for the storage of solar energy.

To stimulate the reforming reaction, the solar radiation needs to heat up the reformer either directly or indirectly. For the directly-irradiated reformer, the heat transfer of the reformer is dominated by the radiation. Therefore, the reactor shells are generally optical materials, which do not prohibit the radiation transfer into the reactor. In this case, the temperature in the reactor can reach over 1273 K, which leads to the reforming reactions work as rate limited [75]. On the contrary, the heat transfer of the indirectly-irradiated reformer is not radiation dominated. In other words, the reformer is headed by the conduction or the convection. Based on the configuration of the reactors, the reformer can be classified as three types: indirectly heated reactor with agent fluid, tubular reformer, and volumetric reformer [76]. The agent fluid, generally with high heat capacity, works as the direct radiation acceptor and absorb the solar energy. Then the energy is transfer to the core reformer. Due to the advantages of the heat approach, the indirect heat reformer has advantages for commercial applications, since the capital cost and the operating conditions are easy to control. The tubular reformer can either works as indirectly-irradiated or directly irradiated reactor due to the transparency of the reactor wall. The most remarkable benefit of the tubular reformer is that it reduces the energy loss during the heat transfer from the solar radiation to the catalyst. The volumetric reformer is a directly-irradiated reactor with low capital cost. However, the main topic of the research is the matching of the reactor structure and the concentrated solar fluxes to maximize energy efficiency.

The noble or transient metal catalysts (Rh, Ru, Ni, etc.) are the most common catalysts for the dry reforming of methane [77-79]. The Ni-based catalysts are popular during recent years, as it is low cost and easy to obtain compared with noble metals.

However, one noteworthy drawback of the Ni-based catalyst is the deactivation due to the carbon deposition [80]. Noble metal promoted Ni-based catalyst is one of the effective methods to increase the stability of the catalyst [81, 82]. The metallic or ceramic foams are used as the catalyst support, which is favorable for the absorption of radiation in the solar thermochemical process. The interaction between the catalyst and the support also influence the performance of the reforming. It is reported that the weaker interaction between the metal catalyst and the inert supports is favorable for enhancing the interactions between metal catalysts [83].

1.2.3. Modeling of Dry Reforming of Methane. During the past few decades, several reaction kinetic models were proposed for the dry reforming of methane process. Overall, the three representative models are the power-law (PL) model, the Eley Rideal (ER) model, and the Langmuir Hinshelwood (LH) model.

The PL model represents the reaction rate of the DRM reaction as [84]:

$$r = k\left[P_{CH_4}\right]^m\left[P_{CO_2}\right]^n \tag{17}$$

where *k* represents the rate constant, P_{CH_4} and P_{CO_2} partial pressures of CH_4 and CO_2, *m* and *n* are the rate coefficients. The PL can be used to roughly estimate the reaction rate of the DRM due to its limitation of the accuracy.

The ER model can be further classified as ER I and ER II based on the reference composition. The equations are shown as follows [85]:

$$r_{ER\ I} = \frac{kK_{CH_4}P_{CH_4}P_{CO_2}}{1 + K_{CH_4}P_{CH_4}} \tag{18}$$

$$r_{ER\ II} = \frac{kK_{CO_2}P_{CH_4}P_{CO_2}}{1 + K_{CO_2}P_{CO_2}} \tag{19}$$

where K_{CH_4} and K_{CO_2} are the equilibrium constants. In the ER models, the reaction between reactants is regarded as the rate-determining step (RDS) with the assumption that the adsorption reaching an equilibrium on the catalyst surface.

The LH model is the most common model that utilized to describe the reaction rate of the DRM, which is presented as [82]:

$$r = \frac{kK_{CH_4}K_{CO_2}P_{CH_4}P_{CO_2}}{(1 + K_{CO_2}P_{CO_2} + K_{CH_4}P_{CH_4})^2} \tag{20}$$

The RDS of the LH model is the reactants react with the catalyst sites. Based on the numerical and experimental studies of the DRM, the LH model best predicts the reaction rate with the appropriate parameters for various catalysts.

1.3. NUMERICAL APPROACHES

1.3.1. Computational Fluid Dynamics. Computation fluid dynamics (CFD) is a computer-based system prediction, simulation, and analysis approach that involves fluid flow, heat transfer, and associated phenomena such as chemical reactions by using numerical methods to solve mathematical models via software solvers. Since discretization is the core mechanism of CFD, the major procedures of discretization are geometry discretization, space discretization, and time discretization.

Geometry discretization is also called mesh generation, which decomposes the research object to a number of cells. Based on the model dimensions, common cell shapes are triangle and quadrilateral (2D); tetrahedron, pyramid, triangular prism, hexahedron, and polyhedron (3D). The mesh cells consist of grids (structured, unstructured, or hybrid), which describe the connectivity among cells. As the research

object is decomposed to discrete cells, the mesh size, cell number, and cell quality all affect the further calculation.

Space discretization is used to numerically address spatial derivatives in partial differential conservation equations. Finite difference, finite volume, and finite element are three fundamental methods that commonly used in CFD. Finite difference method (FDM) has the longest history in CFD codes, which can date back as early as 1910 [86]. Due to the simple algorithm and efficient calculation speed, FDM was popular in the early years. However, FDM has an extremely restricted requirement for grid type and mesh quality due to the algorithm, only structured grids with fine meshes are acceptable in FDM [87]. Because of the limitation on the research domain, FDM is seldom applied in current decades, especially for complicated geometry cases. Finite element method (FEM) is commonly applied for solid domains and non-Newtonian viscoelastic fluid, which is initially proposed by Courant in 1943 and prosperously developed during the 1960s and 1970s [88]. Compared with other methods, FEM has better accuracy, especially on poor mesh quality, but the calculation speed and memory occupation influence the application. Additionally, FEM is not suitable for turbulent flow. Among all three methods, finite volume method (FVM) is the most common and widely used approach and was reported around the 1960s [89, 90]. FVM has unbeatable advantages on addressing a variety of situations even with coarse grids in an efficient way. However, the less accuracy is non-negligible among the advantages. FVM regards each cell as a control volume. By integrating the conservation equations of each control volume, a set of linear algebraic equations can be derived [91]. Generally, the integral form of transport equation can be written as

$$\frac{\partial}{\partial t}\iiint Q\ dV + \iint F\ dA = \iiint S\ dV \tag{21}$$

where Q is the vector of the conserved variable, F is the vector of fluxes, V is the volume of the control volume, A is the surface area of the control volume, S is the source term variable.

Time discretization is used for unsteady state problems by adding the integration of a certain time step in Eq. (21). Explicit scheme and implicit scheme are two major approaches to numerically solve time discretization. The explicit scheme is a low-cost time discretization approach, which requires a small time step for stabilizing the calculation. Since the reconditioning of governing equations is omitted in an explicit scheme, it is not appropriate for incompressible flow cases [92]. Implicit scheme is more popular in common studies of convection and diffusion processes. For implicit scheme, each time step involves several inner iterations so that a convergence can be reached at the certain time. Due to the calculation mechanism, the implicit scheme is more stable for large time steps, however, the result accuracy strongly depends on the time size, which may tremendously increase calculation cost.

1.3.2. Discrete Element Model. Discrete element model (DEM) is a numerical approach to compute the dynamics of a group of simple or complicated geometric solid particles with discrete contact points among particles. This method was originally proposed by Cundall and Strack in 1979 based on the study of rock mechanical behavior at the microscopic level [93]. In the following decades, DEM is applied in different areas. A sketchy of DEM calculation mechanism is introduced in Figure 1.1. The calculation begins with the particle contact detection. When the contact point and the length of particle overlapping are figured out, the force-displacement law is applied to each contact

points to calculate interaction forces. Since interaction forces are derived, they are functionalized on the particle centers. With the combination of Newton's second law of motion, the particles have momentum changes, which leads to a displacement of particle positions and velocities. The derived values are used for the next iteration until objective total steps are reached [94]. The basic transitional and rotational governing equation of particle motions are as follows [95].

$$m_i \frac{d^2}{dt^2} \boldsymbol{r}_i = \boldsymbol{f}_i + m_i \boldsymbol{g} \tag{22}$$

$$I_i \frac{d}{dt} \boldsymbol{\omega}_i = \boldsymbol{t}_i \tag{23}$$

where m_i is particle mass, $\boldsymbol{r}_i$ is its position, $\boldsymbol{f}_i$ is the total contact forces, $\boldsymbol{g}$ is gravitational acceleration, I_i is the moment of inertia, $\boldsymbol{\omega}_i$ is angular velocity, $\boldsymbol{t}_i$ is total torque.

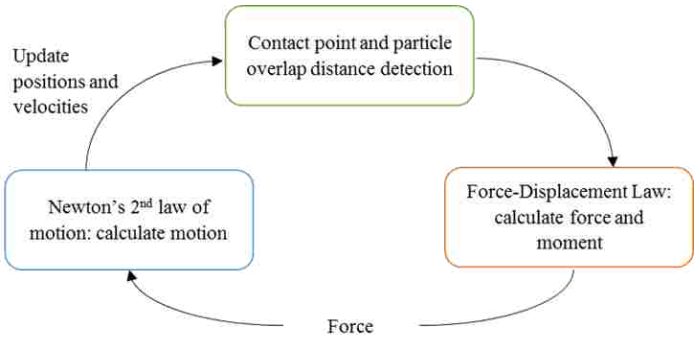

Figure 1.1 DEM calculation mechanism.

The core components of DEM are the elements and the contacts between them. The elements in DEM can be either simple or complicated. Spheres and cylinders are the most common elements in DEM. As the geometry is relatively perfect and causes

unrealistic behaviors, irregular elements are also required in DEM. Three major approaches can solve the irregular element issue. The first approach is set up a clump of spherical particles based on bonded–particle method, which has a comparable rigid body shape with real element [96]. The second approach has simplified the element with polygons [97]. The third approach is using simple geometries including rolling resistant moment on the contact surface [98]. Hertz-Mindlin model and linear elastic model are two common models that solve particle contact forces. The linear elastic model provides a linear relation between force and displacement. Since the model has a simple mathematical expression, it has a huge advantage on calculation speed. However, when the spherical shape is taken into consideration, the Hertz-Mindlin contact model is better to describe the mechanical behaviors between particles [99].

1.3.3. Monte Carlo Ray Tracing. Monte Carlo ray tracing is a computational algorithm to solve radiative heat transfer by tracking the transfer of a great number of energy rays from emission points through the medium. Since this method does not depend on the coordinate system, which has a great advantage in applying to complex geometries. In the domain, the boundary and medium are discretized to surface or volume elements, which have radiative properties (absorbing, emitting, and scattering). The energy emission point is one of the elements in the domain, which shows as an arbitrary number of bundles with equally weighted power. During the transfer process, the bundles may lose or gain power, which reflects as an energy source in the medium due to radiation. By tracing the paths of each bundle, an accumulated power result can be derived. In Monte Carlo ray tracing, random numbers are the fundament of calculation, which commonly generated by the programming language. The numbers are used to

define emission position, bundle directions, and radiative properties during interactions. The surface heat flux and radiation source term are derived from the synthesizing of the tracing results of each bundle. The accuracy of Monte Carlo ray tracing is controllable by adjusting the total number of bundles. As the random number is generated under statistical probabilities, the standard error during calculation is a term that can be ignored. Since Monte Carlo ray tracing is a geometry friendly approach and has low memory consumption, it is a desired method for solar radiation distribution. The estimated integrations of the Monte Carlo method are presented as:

$$S = \int_a^b f(x)p_x(x)dx = E(f(X)) \tag{24}$$

$$s_N = \frac{1}{N}\sum_{i=1}^{N} f(x_i) \tag{25}$$

where x is a series of independent random variables (x_1, x_2, …, x_N), p_x is a probability density function with the expression of $p_x(x) = \frac{1}{b-a}$, s_N represents the Monte Carlo estimate ($E(s_N)=S$).

1.3.4. Discrete Ordinate Model. Discrete ordinate model (DOM) is an approach to solve the radiative transfer equation via discretizing the Cartesian coordinate variables and angular variables to specify the radiation directions, which is firstly proposed by Chandrasekhar [100]. In DOM, the 4π solid angle is divided into n different direction. The radiation transfer equation is solved by numerical quadrature shown below:

$$\frac{dI(\boldsymbol{r},\boldsymbol{s}_i)}{ds} = \kappa I_b(\boldsymbol{r}) - \beta I(\boldsymbol{r},\boldsymbol{s}_i) + \frac{\sigma_s}{4\pi}\sum_{j=1}^{n} w_j I(\boldsymbol{s}_j)\Phi(\boldsymbol{s}_i,\boldsymbol{s}_j) \tag{26}$$

where κ is absorption coefficient, β is extinction coefficient, w_j are quadrature weights associated with the directions, Φ is scattering phase function [101]. Level symmetric quadrature (S_N) is a common approach to arrange the discrete ordinates on the unit sphere, as the latitudes distance among x, y, and z are equal. S_N is used to apply the order of approximation of DOM, where the relation between N and n is $n = N(N+2)$. With the increase of N, the calculation accuracy is improved. The one-eighth discrete ordinates sketch of S4 is shown in Figure 1.2. The ordinates are defined by angular ordinates $\boldsymbol{s}_j = \xi\boldsymbol{i} + \eta\boldsymbol{j} + \mu\boldsymbol{k}$ and angular weights w_j, whose values are derived by Lathrop and Carlson (1965) [102]. Based on the direction function, there are three directions should appear in one eighth of sphere.

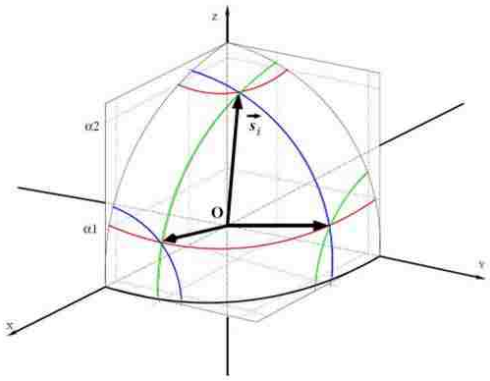

Figure 1.2 One-eighth DOM sketch of S4.

1.4. DISSERTATION SUMMARY

Section 1 includes three papers. In Paper Ⅰ, the numerical study of the reduction reaction of the two-step solar thermochemical cycles with cerium oxide catalyst in a solar

thermochemical reactor. The DEM approach was utilized to simulate the porous catalyst structure in the reactor. The reduction performances were studied via varying the catalyst textures (void fraction and particle size) and the operating condition (gas flow rate and input solar power).

In Paper Ⅱ, the heat transfer performances of the self-designed partition-cavity solar thermochemical reactor were studied by varying the values of some critical geometric factors of the reactor. The MCRT radiation model was used to simulate the concentrated solar energy via a parabolic-dish solar collector. The cerium oxide reduction rate was investigated in the optimized solar thermochemical reactor and showed a good solar-to-fuel efficiency.

In Paper Ⅲ, three conceptual shapes of the periodic open cellular structured (POCS) catalyst lattices from the additive manufacturing were investigated for the dry reforming of methane process in the partition-cavity solar thermochemical reactor. The heat and mass transfer were separately discussed based on the POCS strut parameters and the reaction operating conditions.

In Section 2, it summarizes the conclusions of this dissertation and some promising work directions in the future.

PAPER

I. MODELING OF CERIA REDUCTION IN A SOLAR THERMOCHEMICAL REACTOR VIA DEM METHOD

Han Zhang and Joseph D. Smith

Department of Chemical and Biochemical Engineering, Missouri University of Science and Technology, 1101 North State Street, Rolla, MO 65409, United States

ABSTRACT

Solar thermochemical reactor provides an attractive approach that utilizes the most common solar radiation as the thermal driving force to motivate the reaction between CO_2 and metal oxides, which is also called metal oxide redox pair-based thermochemical cycles. The $CeO_2/CeO_{2-\delta}$ is widely used in the two-step redox process due to its advantages including fast-redox kinetics, high crystallographic stability of a wide range of reacting oxygen non-stoichiometry, and relatively high oxygen solid-state conductivity. In this work, a three-dimensional transient numerical analysis has been completed to study the performance of a CeO_2 reduction reaction in a $1/8^{th}$ segment region of a novel partition cavity-receiver reactor. The porous CeO_2 catalyst was analyzed using the discrete element method (DEM) to capture the heat transfer and reactive performances. The catalyst textural properties (particle size and void fraction) and reaction conditions (gas flow rate and radiative power input) were investigated in the CeO_2 reduction reaction. The results indicated that increasing the catalyst specific surface area and the temperature are beneficial to the O_2 production and further CO_2 conversion.

Keywords: Solar Thermochemical Reactor, Ceria Reduction, Radiation, Transient, DEM, Chemical Energy Storage

NOMENCLATURE

Symbols

A	surface area
D	diameter
f_b	body force (gravity)
F_s	Particle surface force (N)
F_b	Particle body force (N)
h	Enthalpy (J kg^{-1})
I	Radiative intensity (W m^{-2})
I	Identity matrix
k	thermal conductivity (W m^{-1} K^{-1})
k_a	absorption coefficient (m^{-1})
k_{pa}	particle absorption coefficient (m^{-1})
k_{ps}	particle scattering coefficient (m^{-1})
k_{red}	reduction rate coefficient
k_s	Scattering coefficient (m^{-1})
m_f	final particle mass
m_i	initial particle mass
$\dot{m}_p$	rate of mass transfer to particle
q_r	re-radiation (W m^{-2})
Q	heat transfer (W)
$Q_{a,p}$	absorption efficiency of particle
Q_t	Surface heat transfer (W)
s	distance in Ω direction
S_E	energy source (W m^{-2} or W m^{-3})
S_m	mass source (mol m^{-3} s^{-1})
t	time (s)

T	temperature (K)
v	velocity (m s^{-1})
x	reaction fraction
Y_i	component concentration

Greek Symbols

β	Extinction coefficient
δ	non-stoichiometric coefficient
ρ	Density (kg m^{-3})
σ	Stefan-Boltzmann constant
Ω	solid angle

Subscripts

b	black body
conv	convection
f	fluid
fs	fluid-solid interphase
p	particle
part	partition
pb	Particle black body
rad	radiation
reac	reaction (reduction)
s	Insulation

Abbreviation

DEM	Discrete Element Method
DOM	Discrete Ordinates Model
i.d.	Inner diameter
Nu	Nusselt number
o.d.	Outer diameter
ppm	part per million
Pr	Prandtl number
Re	Reynold’s number

1. INTRODUCTION

With the growing energy demands in the world, environmental protection issues have attracted a lot of attention related to energy technology development. Among various energy resources, fossil fuel remains the primary and stable energy source. Along with the use of fossil fuels, carbon dioxide emission rate is a serious factor that affects climate change and the global environment. Figure 1 shows global carbon dioxide emissions from 1980 to 2016 [1].

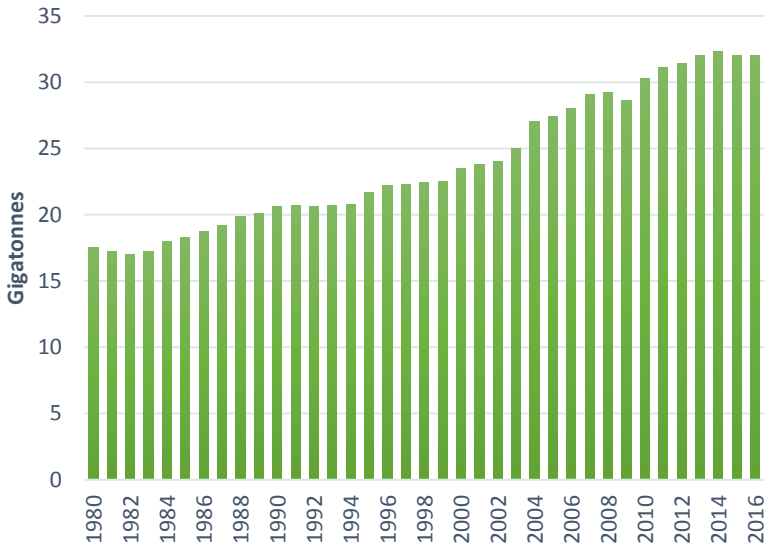

Figure 1. Global carbon dioxide emissions from 1980 to 2016 [1].

From this figure, it is seen that CO_2 emissions continue at a high level, even though there has been no prominent increase in recent five years. In order to reduce the carbon emission, numerous studies focusing on using clean energies or novel technologies are proposed to solve this issue [2–6]. Since CO_2 is also a carbon source and

can be converted into useful and variable materials, work has been focused on finding efficient technology to accomplish this process. Decades ago, people began studying water electrolysis to produce hydrogen, since water is a cheap and available resource. However, hydrogen storage is an issue due to its high volatile property [7]. Compared with water electrolysis, syngas production from CO_2 and H_2O does not only provide an option for environmental protection and transportation safety but also offers an attractive energy fuel for further applications during the chemical process, like Fischer-Tropsch technology [8,9]. Solar energy is essentially a green technology with inexhaustible power production potential. Under the concentrated energy from the sun, CO_2 and H_2O can be converted to syngas using proper metal oxide redox pairs such as ZnO/Zn [10–13], Fe_3O_4/FeO [14–16], and many more advanced couples [17–20]. The appearance of producing syngas via solar energy provides a brand-new idea for both solar energy application and chemical fuel production.

The two-step solar thermochemical process is a redox cycle based on metal oxide redox. This chemical process is represented as the high-temperature reduction (see Eq. (1)) and low-temperature oxidation (see Eq. (2) and (3)).

High-temperature reduction: $$M_xO_y \rightarrow M_xO_{y-\delta} + \frac{\delta}{2} O_2 \quad (1)$$

Low-temperature oxidation: $$M_xO_{y-\delta} + \delta CO_2 \rightarrow M_xO_y + \delta CO \quad (2)$$

$$M_xO_{y-\delta} + \delta H_2O \rightarrow M_xO_y + \delta H_2 \quad (3)$$

In the first step, the metal oxide is reduced to form pure metal or reductive metal oxide that releases oxygen at temperature 1000 °C [17]. This reaction is endothermic, so excess energy must be supplied using concentrated solar energy. In the second step, the oxidation reactions are exothermic and occur at a lower temperature (<1000 K). The feed

CO_2/H_2O react with metal or reduced metal oxide and lose oxygen to form CO/H_2. Correspondingly, the metal or reduced metal oxide is oxidized to the former oxidation state. Compared with syngas production cycles, the most remarkable advantage of the two-step solar thermochemical process is that the water splitting and carbon dioxide splitting share the same reaction mechanism, which provides a great convenience for further analysis [21].

The metal oxide pairs for the two-step solar thermochemical redox process can be divided into two groups, volatile and non-volatile, based on physical properties and boiling temperature [22]. Since the temperature requirement for reduction is up to 2300 K, possibly higher than the boiling temperature of the reduced species, the volatile metal oxide may experience a phase change. There are some representative metal oxide pairs, including ZnO/Zn, CdO/Cd, SnO_2/SnO, GeO_2/GeO, and so forth [23–26]. Even though the volatile redox pair results in an extra entropy gain for the system due to the phase transition, the recombination of oxygen and reduced metal or metal oxide has a significant impact on fuel production of volatile pairs [27]. Non-volatile redox pairs (e.g. ferrites, ceria, hercynite, and perovskites) [17,28,29] can maintain their solid state at high temperatures, which avoid the recombination issue. Other morphology characteristics of non-volatile redox pairs, such as pore size, porosity, and specific surface area, also affect the reaction rate.

Cerium oxide is a representative redox catalyst used to produce carbon monoxide and hydrogen in the early 1980s due to its excellent performance in releasing and recovering oxygen [30]. With the development of renewable energy, solar energy has become an attractive energy provider to power the redox reactions of CeO_2 due to the

photocatalysis of ceria [31]. The application of the non-stoichiometric CeO_2 redox pair for solar thermochemical reactions flourished in the last decade. In 2006, Flamant et al. [32] proposed the application of CeO_2/Ce_2O_3 redox pair to split water. The reduction of CeO_2 was proceeded at 2000 °C, 100~200 mbar, followed by the oxidation step in the temperature range of 400-600 °C. Since reduction temperature is high enough to transfer CeO_2 to a molten state, which strongly reduces the catalyst activity and quality, the study of CeO_2 was focused on how to avoid the phase transfer under a high reduction temperature. Non-stoichiometric CeO_2 ($CeO_{2-\delta}$) was proposed to solve the issue of melting at high temperature. Based on the two-step thermochemical process, the reactions can be represented by

$$CeO_2 \rightarrow CeO_{2-\delta} + \frac{\delta}{2} O_2 \quad (4)$$

$$CeO_{2-\delta} + \delta CO_2 \rightarrow CeO_2 + \delta CO \quad (5)$$

$$CeO_{2-\delta} + \delta H_2O \rightarrow CeO_2 + \delta H_2 \quad (6)$$

The solar-to-fuel efficiency (see Eq. (7)) is used to show the reaction performance [33].

$$\eta_{solar-to-fuel} = \frac{\dot{n}_{fuel} HHV}{\dot{Q}_{solar}} \quad (7)$$

Chueh et al. [21] presented the application of porous monolithic ceria on the two-step solar thermochemical CO_2/H_2O splitting. The results showed that porous monolith ceria can reach a stable fuel generation state after 500 redox cycles with an estimated 0.8% peak solar-to-fuel efficiency. Furler et al. [34] proposed using porous ceria felt as the catalyst to support solar CO_2/H_2O splitting. The O_2 and fuel production are 2.89 ± 0.27 mL g^{-1} CeO_2 and 5.88 ± 0.43 mL g^{-1} CeO_2. Furler et al. [35] also proposed a reticulated

porous ceria (RPC) foam structure for redox reactions, which derived a 3.53% peak solar-to-fuel efficiency. The efficiency improved more than four times compared with former porous monolithic ceria. Venstrom et al. [36] presented a novel morphology of CeO_2, three-dimensional-ordered macroporous (3DOM) CeO_2, which has both higher specific surface area and effective pore interconnections. The fuel production rate was enhanced by as much as 260% and 175% compared with traditional low porosity ceria and non-ordered mesoporous ceria.

Based on the difference of heat transfer type, solar thermochemical reactors can be classified as indirectly-irradiated reactors and directly-irradiated reactors. For indirectly-irradiated reactors, the reactor chamber material is generally made from opaque metals. Incoming solar radiant flux to the external wall of the reactor is transferred to heat conduction to raise the temperature of the metal oxide. For directly-irradiated reactors, the solar radiation can directly touch the surface of the metal oxide and use the incident radiation to heat up the oxide. Since the radiation term in the energy conservation equation also participates in heat transfer in directly-irradiated reactors, the reactor can achieve a higher temperature. To fully utilize the solar radiation, the cavity-receiver reactor is commonly used for directly-irradiated solar thermochemical processes. In a cavity-receiver reactor, the space provided in the cavity provides or enhances radiation to the catalyst inner surface, which forms an approximate blackbody. Different types of cavity-receiver reactors have been discussed and used over the past several years to prove that direct irradiation has a huge advantage on the two-step solar H_2O/CO_2 splitting process [37–40].

To better predict and validate the CeO_2 supported solar thermochemical two-step redox cycle, several chemical kinetics were studied and utilized to model the solar thermochemical process performances in recent years. Thermodynamic equilibrium model is a representative reaction model that widely used in the simulations of CeO_2 two-step redox reactions. Calle et al. [41], Groehn et al. [42], Bulfin et al. [43] introduced the relation between non-stoichiometric coefficient with oxygen partial pressure and temperature [44] in their process simulation and reactor modeling, respectively. It was proved that the model has a higher agreement with the model of Zinkevich et al. [45]. The most basic chemical kinetics reaction model is based on the Arrhenius equation proposed by Ishida et al. [46]. This model was applied in different tubular reactor studies [47–49]. However, the accuracy needs to be improved, due to the limitation of the current reported values of coefficients in the Arrhenius equation [47]. Arifin et al. [50] and McDaniel et al. [29] used the improved solid-state kinetic model, which includes the influences of reaction order of the oxidant mole fraction and the progress of the rate of oxidation [51], With their studies, the solid-state kinetic model is further parametrized for accurately evaluating the reaction rates. Based on the theory of Kröger et al. [52], the crystal site relations of CeO_2 reduction was discussed in the work of Scheffe et al. [53] and corresponding reaction mechanism was applied in the work of Bader et al. [54] to study the CeO_2 reduction performances in a particle suspension system.

Gas-solid performance plays a vital role in the numerical simulation of solar thermochemical processes. The Eulerian-Lagrangian (CFD-DEM) method, which uses the DEM method to solve the transfer performances of particles individually in the gas continuum phase, is a representative approach to capture the variations of the dispersed

phase. It was widely used in the simulations of fluidized bed reactors [55–58], however, the application in the solar thermochemical processes for high-temperature chemical reactions is still in the infantile stage. Bellan et al. did a series of work on the heat transfer performances in different types of fluidized bed reactors for solar gasification and solar thermochemical cycles using the CFD-DEM method and the results showed high agreement between the experimental and simulation results [59–63]. Morris et al. used CFD-DEM method to study the heat transfer performances in the novel solar receiver designed by the National Renewable Energy Laboratory and proved that the improved continuum model has a high accuracy to predict the heat transfer coefficient [64]. Although some studies have been reported to focus on the heat transfer performances in the solar fluidized bed reactors using the CFD-DEM method, very few works consider the reactions in the solar thermochemical two-step metal redox cycles. Additionally, the transfer performances in the porous catalyst simulated by the DEM methods are worthy of discussing intensively.

In this paper, a three-dimensional (3D) transient multi-physics computational fluid dynamics model is applied to study heat and mass transfer of a high-temperature CeO_2 reduction process in a novel partition cavity solar thermochemical reactor. The model uses the discrete element method (DEM) [65] to approximate the structure of a CeO_2 layer as a packed bed. Several parameters defining the operating conditions and the catalyst layer formation have been studied to investigate the performance of the CeO_2 reduction in the novel partition-cavity thermochemical reactor.

2. REACTOR DESIGN CONCEPT

The reactor (shown in Figure 2) consists of a cylindrical cavity and a solar radiation receiver. An annular cylindrical catalyst region (60 mm i.d., 100 mm o.d., and 150 mm height) is integrated into the cavity section. The reactive region is separated from the cavity center by a transparent quartz partition (145 mm height). A 5 mm gap between the bottom of the transparent partition and cavity bottom leaves space for fluid to pass through the entire length of the reactive packed bed. Additionally, the transparent quartz allows solar radiation to enter the reactive region. With the partition design, the reactive cavity not only provides a relatively long path for contact of gas and solid but also enhance radiation heat transfer to the reactive region.

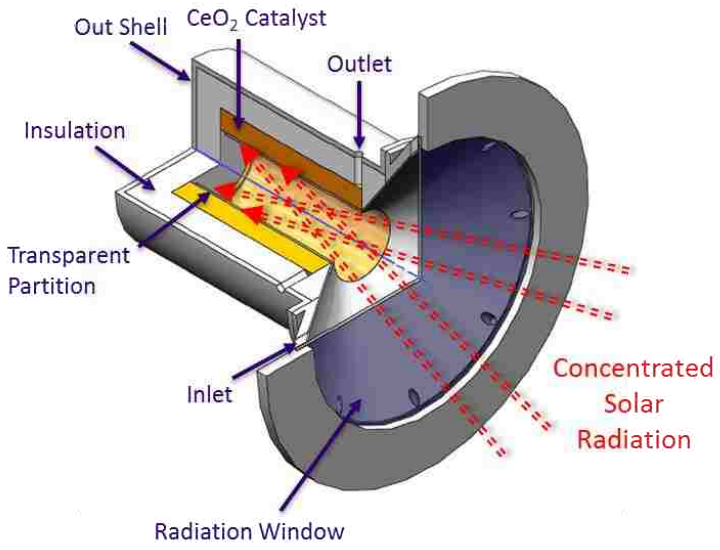

Figure 2. Partition-cavity solar reactor schematic diagram.

The reactive region is surrounded by a ceramic insulation material inside the stainless-steel outer shell. Concentrated solar radiation enters the reactor through the 240

mm receiver window and focuses on the interface of the solar receiver and reactive cavity. Concentrated radiation distributes over the inner cavity surface and enters the reactive region. Eight inlets and outlets, each with a diameter of 8 mm, are evenly distributed around the top edge of the solar receiver and reactive cavity side walls (see Figure 2 and 3).

3. APPROACH

3.1. REACTOR MODEL

Figure 3 shows the solar reactor modeling geometry in top view and cross-section. Since the reactor has a symmetric structure, only one-eighth of the entire geometry is simulated, with the assumption that radiation distribution and thermal losses are symmetric. Plane MN and MP are periodic boundary conditions with a 45^{o} rotational angle. The stainless-steel housing and receiver are considered insignificant resistances, which are included in the wall boundary conditions to approximate heat loss from the reactor. Cerium dioxide (CeO_2) is packed in the reactive region to form a porous media structure approximated by the DEM method. By controlling the DEM injecting conditions, the catalyst particles are uniformly distributed through the entire reactive region that creates the appropriate gas flow paths to effectively mimic the structure of a porous media region. The reactive section is sheathed by ceramic insulation material Al_2O_3-SiO_2 with surfaces to exchange radiation heat transfer. Radiative heat transfer is implemented using the discrete ordinates model (DOM) [65] with gray thermal radiation model, which considers the radiative properties of participated media and the surrounding

surfaces are identical for all wavelengths [66]. CeO_2 is assumed to be a black body radiator and Al_2O_3-SiO_2 layer is assumed to be a good thermal insulator with an emittance of 0.28. The receiver side wall is highly reflective material with a reflectance of 0.9. The incident solar power is assumed to be evenly distributed on the partition surface for simplification. Argon (Ar), entering the reactor from radial inlets on the solar receiver, works as an inert purge gas during preheating and reduction processes to improve the heat convection and accelerates the motion of generated oxygen.

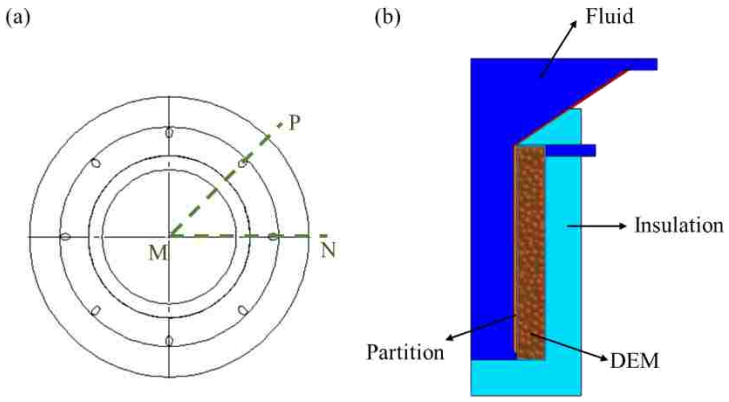

Figure 3. Simulation reactor model. (a) top view; (b) cross-section.

3.2. NUMERICAL ANALYSIS AND VALIDATION

The simulated reactor schematic diagram in Figure 3 (b) represents the computational domains considered in the reactor model. Generally, the domains can be divided into non-reactive regions and reactive regions. Non-reactive domains include the solar receiver, the reactor cavity, and the inlets and outlets, which are simulated as fluid regions with laminar flow and ideal gas mixture. The transparent quartz partition and Al_2O_3-SiO_2 insulation are considered as solid walls with corresponding thermal

properties (conductivity and emittance). The reactive domain is a multiphase region gas mixture flowing through a packed bed of CeO_2 particles. To set up the link between the particles and fluid phases, a two-way coupling method is introduced that solves the heat and mass transfer conservation equations in both phases [65].

3.2.1. Non-Reactive Regions. The continuity, momentum, energy, and mass conservation equations of fluid regions areas follow:

$$\frac{\partial \rho_f}{\partial t} + \nabla \cdot \left(\rho_f \boldsymbol{v}\right) = 0 \tag{8}$$

$$\frac{\partial (\rho_f \boldsymbol{v})}{\partial t} + \nabla \cdot \left(\rho_f \boldsymbol{v}\boldsymbol{v}\right) = -\nabla p + \nabla \cdot \mu \left(\nabla \boldsymbol{v} + (\nabla \boldsymbol{v})^T - \frac{2}{3}\boldsymbol{I}\nabla \cdot \boldsymbol{v}\right) + \boldsymbol{f_b} \tag{9}$$

$$\frac{\partial (\rho_f h)}{\partial t} + \nabla \cdot \left(\rho_f h \boldsymbol{v}\right) = \nabla \cdot (k \nabla T) \tag{10}$$

$$\frac{\partial (\rho_f Y_i)}{\partial t} + \nabla \cdot \left(\rho_f \boldsymbol{v} Y_i\right) = 0 \tag{11}$$

where ρ_f is fluid density, $\boldsymbol{v}$ is velocity vector, p is pressure, μ is fluid dynamic viscosity, $\boldsymbol{I}$ is identity matrix, $\boldsymbol{f_b}$ is momentum body force (gravity), h is fluid enthalpy, k is fluid thermal conductivity, and Y_i is component concentration [65].

Since there is no flow in the solid regions, only the energy conservation equation is considered. Eq. (12) and (13) show the energy conservation of partition and insulation:

$$\frac{\partial (\rho_{part} h_{part})}{\partial t} + \nabla \cdot \left(\rho_{part} h_{part} \boldsymbol{v}\right) = \nabla \cdot \left(k_{part} \nabla T\right) + S_{E,rad} \tag{12}$$

$$\frac{\partial (\rho_s h_s)}{\partial t} + \nabla \cdot (\rho_s h_s v) = \nabla \cdot (k_s \nabla T) + \nabla q_r \tag{13}$$

where ρ_{part} is partition density, ρ_s is insulation density, h_{part} is partition enthalpy, h_s is insulation enthalpy, k_{part} is partition thermal conductivity, k_s is insulation thermal conductivity, $S_{E,rad}$ is source term of radiation, ∇q_r is re-radiation term. The input radiation and the re-radiation are included in $S_{E,rad}$, which can be solved from the radiative transfer equation:

$$\frac{dI}{ds} = -\beta I + k_a I_b + \frac{k_s}{4\pi}\int_{4\pi} I(\Omega)d(\Omega) + k_{pa} I_{pb} + \frac{k_{ps}}{4\pi}\int_{4\pi} I(\Omega)d(\Omega) \quad (14)$$

where I is radiative intensity, k_a is absorption coefficient, k_s is scattering coefficient, I_b is black body intensity, Ω is solid angle, k_{pa} is particle absorption coefficient, k_{ps} is particle scattering coefficient, I_{pb} is particle black body intensity, β is extinction coefficient, and s is distance in the Ω direction. Re-radiation is used to couple the fluid and radiant energy field, which is shown as:

$$\nabla q_r = k_a(4\pi I_b - \int_{4\pi} I\, d\Omega) \quad (15)$$

3.2.2. Reactive Region. The multiphase domain is the core-reactive region in the reactor consisting of two phases: gas mixture fluid phase and CeO_2 particle Lagrangian phase. The fluid continuous phase should consider the interaction between gas mixture and CeO_2 particles, which can be conveyed as source terms in governing equations. The conservation equations are as follows:

$$\frac{\partial(\rho_f)}{\partial t} + \nabla \cdot (\rho_f \boldsymbol{v}) = S_{m,\,O_2} \quad (16)$$

$$\frac{\partial(\rho_f \boldsymbol{v})}{\partial t} + \nabla \cdot (\rho_f \boldsymbol{v}\boldsymbol{v}) \quad (17)$$

$$\frac{\partial(\rho_f h)}{\partial t} + \nabla \cdot (\rho_f h \boldsymbol{v}) = \nabla \cdot (k\nabla T) + h_{fs} A_{fs}(T_s - T_f) + \nabla q_r + S_E \quad (18)$$

$$\frac{\partial(\rho_f Y_{O_2})}{\partial t} + \nabla \cdot (\rho_f \boldsymbol{v} Y_{O_2}) = S_{m,\,O_2} \quad (19)$$

where $S_{m,\,O_2}$, S_V, and S_E are the binary phase coupling mass source term, momentum source term, and energy source term, respectively. These terms can be expanded and shown as:

$$S_V = -\frac{1}{\Delta t}\sum\nolimits_{\pi}\left(\int_t^{t+\Delta t}\int_{V_c} \delta(\boldsymbol{r} - \boldsymbol{r_\pi}) n_\pi (\boldsymbol{F_s} + \dot{m}_p \boldsymbol{v_p}) dV dt\right) \quad (20)$$

$$S_E = -\frac{1}{\Delta t}\sum\nolimits_{\pi}\left(\int_{t}^{t+\Delta t}\int_{V_c}\delta(\boldsymbol{r}-\boldsymbol{r_\pi})n_\pi\left(Q_t + \boldsymbol{F_s}\cdot v_p + \frac{1}{2}\dot{m}_p{\boldsymbol{v_p}}^2\right.\right. \tag{21}$$

$$S_{m,O_2} = -\frac{1}{\Delta t}\sum\nolimits_{\pi}\left(\int_{t}^{t+\Delta t}\int_{V_c}\delta(\boldsymbol{r}-\boldsymbol{r_\pi})n_\pi\dot{m}_p dV dt\right) \tag{22}$$

where $\boldsymbol{F_s}$ is particle surface force and $\dot{m}_p$ is particle mass transfer rate. The volume integral is based on cells. The Dirac delta function accounts for the parcels not represented in the cell. The concrete formations of $\boldsymbol{F_s}$ and $\dot{m}_p$ are discussed with the governing equations for DEM particles. By taking the particle motion, energy, and mass influences into consideration, the fluid governing equations approximate fluid/particle interactions using the DEM packing conditions.

Since CeO_2 particles work as discrete elements, the momentum conservation is shown based on surface and body force. Particle mass and heat transfer happen on interphase, which should be considered together. The governing equations are represented below:

$$m_p\frac{d\boldsymbol{v_p}}{dt} = \boldsymbol{F_s} + \boldsymbol{F_b} \tag{23}$$

$$m_p c_p\frac{dT_p}{dt} = Q_{conv} + Q_{rad} + Q_{reac} \tag{24}$$

$$\frac{dm_p}{dt} = \dot{m}_p \tag{25}$$

where $\boldsymbol{F_s}$ is surface force including drag force and pressure gradient, $\boldsymbol{F_b}$ is body force including gravity and contact force, Q_{conv} is convective heat transfer from the fluid phase to the particle, Q_{rad} is radiative heat transfer rate, Q_{reac} is heat of reduction reaction. Eq. (26) shows how Q_{conv} can be formulated:

$$Q_{conv} = h_{fp}A_s(T - T_p) \tag{26}$$

where h_{fp} is heat transfer coefficient, A_s is particle surface area, T is fluid temperature, T_p is particle temperature. Heat transfer coefficient h_{fp} can be derived from the relation of particle Nusselt number [65]:

$$Nu_p = \frac{h_{fp} D_p}{k} \tag{27}$$

where k is particle thermal conductivity and D_p is particle diameter. Since $Re_p < 5000$, the Ranz-Marshall correlation [67] can be applied to determine the particle Nusselt number:

$$Nu_p = 2(1 + 0.3 Re_p^{1/2} Pr^{1/3}) \tag{28}$$

where Pr is from the fluid phase.

The particle participated radiative heat transfer Q_{rad} is defined as:

$$Q_{rad} = \frac{A_s}{4} Q_{a,p}(G - 4\sigma T_p^4) \tag{29}$$

where $Q_{a,p}$ is absorption efficiency of particles, G is incident radiative heat flux, and σ is the Stefan-Boltzmann constant. In this paper, CeO_2 is assumed to have a 90% absorption efficiency. Reaction enthalpy of CeO_2 reduction Q_{reac} in Eq. (4) is around 475 kJ per 1/2 mole of O_2 [68].

3.2.3. Chemical Reaction. In our study, the mixed chemical kinetic and equilibrium model was applied to simulate the CeO_2 reduction of DEM particles. The reaction was set up based on the DEM particle phase and combined the mass transfer with the fluid phase via the former introduced source term ($\boldsymbol{S_{m,O_2}}$). Based on the thermodynamic equilibrium model, which combines the crystal site model with the standard Gibbs free energy equation [53], the non-stoichiometric coefficient δ is a function of temperature and oxygen partial pressure [44]:

$$\frac{\delta}{0.35-\delta} = \left(\frac{106{,}000\ Pa}{P_{O_2}}\right)^{0.217} \exp\left(\frac{-195.6\ kJ/mol}{RT}\right) \quad (30)$$

The reaction rate in the DEM particle phase is expressed as $\dot{m}_p$ in Eq. (25). To describe the reaction in the particle phase, the CeO_2 reduction was regarded as the form of particle devolatilization. As the CeO_2 reduction process is a non-stoichiometric reaction, the user reaction rate method (Eq. (31) is applied instead of the default first order rate method (Eq.(32)) [66].

$$\dot{m}_p = \frac{dm}{dt} = -r_{user\ rate} \quad (31)$$

$$\frac{dm}{dt} = -km \quad (32)$$

Based on the study of Ishida et al. [44], the CeO_2 reduction rate can be expressed as:

$$\frac{dx}{dt} = k_{red}(1-x) \quad (33)$$

where k_{red} is the reduction rate constant, x is the reaction fraction. The reaction fraction can be conveyed as

$$x = \frac{m-m_i}{m_f-m_i} \quad (34)$$

where m, m_i, and m_f are time-dependent particle mass, initial particle mass, and final particle mass, respectively.

Since Ce is conserved in the CeO_2 reduction process, the concentration of vacant oxygen ($[O_{vac}]$) and the concentration of cerium ($[Ce]$) have the following relation:

$$\frac{[O_{vac}]}{[Ce]} = \delta \quad (35)$$

Based on the above conservation between the concentration of oxygen and the concentration of cerium, the time-dependent particle mass m in Eq. (31) can be shown as a function of δ:

$$m = m_i - \delta n_{CeO_2} M_{O_2}/2 \tag{36}$$

where n_{CeO_2} is the moles of CeO_2 and M_{O_2} is the molecular weight of oxygen.

By substituting Eq. (30) and (33) into Eq.(31), the production generation rate is

$$r_{user\ rate} = \frac{dm}{dt} = (m_f - m_i) \cdot k_{red} \cdot (1 + \frac{\delta \frac{m_i}{M_{CeO_2}} M_{O_2}}{2(m_f - m_i)}) \tag{37}$$

The particle devolatilization rate based on Eq. (31) can be expressed as:

$$\dot{m}_p = -(m_f - m_i) \cdot k_{red} \cdot (1 + \frac{\delta \frac{m_i}{M_{CeO_2}} M_{O_2}}{2(m_f - m_i)}) \tag{38}$$

3.2.4. Boundary and Initial Conditions. The boundary conditions are summarized in Table 1. A no-slip boundary condition is assumed on all fluid-solid interfaces. All the outer wall surfaces are adiabatic. The inlet surfaces are set as velocity inlet condition with the velocity taken from the volume flow rate. The outlets operate under atmospheric pressure. The boundary condition of the partition inner surface is taken as a diffuse radiation flux condition, which is determined by input radiation power. The radiative properties of partition and insulation boundaries depend on the material properties (listed in Table 1).

The entire reduction process can be divided into two sections: 1) preheating and 2) reaction. The initial conditions are distinguished for each section. The preheating process is initiated from room temperature (298 K) and atmospheric pressure (1 atm) with pure Ar purge gas. The particle devolatilization is deactivated. After 20 mins

radiation under 1.5 kW power, the preheating process is terminated. In the reaction stage, the initial conditions are taken from the preheating stage, except the inlet oxygen mole fraction is set as 10 ppm.

Table 1. Boundary conditions.

Surface	**Boundary Conditions**
Inlets	$v_{inlet} = \frac{\dot{V}}{A_{inlets}}; T_{inlet} = T_{room}$
Outlets	$p_{out} = p_{atm}$
Partition inner surface	$k_{part}\frac{\partial T}{\partial n} = S_{rad} + h_{part}\Delta T$
Insulation inner surface	$k_s\frac{\partial T}{\partial n} = \Delta q_r + h_s\Delta T$
All other surfaces	$\frac{\partial T}{\partial n} = 0$

3.2.5. Parameters. The material properties of gas components, catalyst, and solid components are listed in Table 2. In this paper, four important parameters are studied to compare the performance via the control variable method. The four parameters can be classified into two groups. One is related to operating conditions, like radiant power and gas flow rate. The other is related to CeO_2 particle packings, such as void fraction and particle size. To expand the study rationally, a base case is defined with a void fraction of 0.65, a particle size of 5 mm, under radiant power of 3.5 kW in the reaction stage, and the gas flow rate is set to 1.8 L/min (specific parameters listed in Table 3).

Table 2. Material properties.

Material	Property	Expression	T(K)
CeO_2	Density (kg m^{-3}) [69]	7220	298
	Molecular weight (g mol^{-1})	172.12	
	Specific heat capacity (J kg^{-1} K^{-1}) [69]	$-0.0001271 \cdot T^2 + 0.2697656 \cdot T + 299.8695684$	280-1100
		444.27	>1100
	Thermal conductivity (W $m^{-1}K^{-1}$) [70]	$-1.7234232 \cdot 10^{-9} \cdot T^3 + 1.1203174 \cdot 10^{-5} \cdot T^2 - 0.024019964 \cdot T + 17.800409$	280-2000
	Enthalpy of formation (J $kmol^{-1}$) [71]	$-1.0887 \cdot 10^9$	298
Quartz Glass	Density (kg m^{-3}) [72]	2500	298
	Specific heat capacity (J mol^{-1} K^{-1}) [73]	$-0.0001 \cdot T^2 + 0.1791 \cdot T - 0.173$	273-847
		$0.0072 \cdot T + 61.717$	847-2000
	Thermal Conductivity (W $m^{-1}K^{-1}$) [74]	$1.18 + 3.14 \times 10^{-3} \cdot T + 17966/T^2$	273-2000
	Emissivity [75]	0.06	273-2000
	Transmissivity [75]	0.86	273-2000
Al_2O_3-SiO_2	Density (kg m^{-3}) [69]	560.65	298
	Specific heat capacity (J kg^{-1} K^{-1}) [69]	$4 \cdot 10^{-7} \cdot T^3 + 1.3797 \cdot 10^{-3} \cdot T^2 + 1.5987289 \cdot T + 447.6996$	≤1480
		1118.44	>1480
	Thermal Conductivity (W $m^{-1}K^{-1}$) [69]	$0.00012926 \cdot T + 0.019654$	280-2200
	Emissivity [69]	0.28	
Argon	Density (kg m^{-3}) [72]	1.634	298
	Viscosity (Pa · s) [72]	$2.277 \cdot 10^{-5}$	298
	C_p/R [76]	2.5	298-5000
	Thermal Conductivity (W $m^{-1}K^{-1}$) [77]	$0.004834 + 4.83706 \cdot 10^{-5} \cdot T - 1.29 \cdot 10^{-8} \cdot T^2 + 2.3533 \cdot 10^{-12} \cdot T^3$	290-2400
Oxygen	Density (kg m^{-3})	1.30878	298
	Viscosity (Pa · s)	$2.054 \cdot 10^{-5}$	298
	C_p/R [76]	$3.7825 - 2.9967 \cdot 10^{-3} \cdot T + 9.8473 \cdot 10^{-6} \cdot T^2 - 9.6813 \cdot 10^{-9} \cdot T^3 + 3.2437 \cdot 10^{-12} \cdot T^4$	200-1000
		$3.6610 + 6.5637 \cdot 10^{-4} \cdot T - 1.4115 \cdot 10^{-7} \cdot T^2 + 2.0580 \cdot 10^{-11} \cdot T^3 - 1.2991 \cdot 10^{-15} \cdot T^4$	1000-5000
	Thermal Conductivity (W $m^{-1}K^{-1}$) [78]	$7 \cdot 10^{-5} \cdot T + 0.007$	270-2500

3.2.6. Numerical Implementation. The transport conservation equations are solved by the finite volume method with approximately 400,000 hexagonal cells in an unstructured mesh using STAR-CCM+ v. 12.02 [66]. A first-order implicit unsteady scheme is used for time integration with a time step of 2.0 s. The second-order segregated flow/energy/species algorithms are applied in the computation of conservation equations. The DEM solver is introduced to solve the governing equations of discrete CeO_2 particles [79]. The non-stoichiometric CeO_2 reduction is defined via user-defined field functions as a source term. The transient simulations are performed on a high-performance cluster "FLARE" (6 x (1 Lenovo NeXtScale nx360m5 compute node, 64 GB RAM)).

Table 3. Studied reactor parameters.

Case	**Parameter**	**Other Conditions**	
Gas Flow Rate (L/min)	1.8, 2.5, 3.2	ε	0.65
		d_p	5 mm
		P	3.5 kW
Solar Radiant Power (kW)	3.0, 3.5, 4.0, 4.5	ε	0.65
		d_p	5 mm
		$\dot{V}$	1.8 L/min
CeO_2 Void Fractions	0.50, 0.60, 0.65	d_p	5 mm
		P	3.5 Kw
		$\dot{V}$	1.8 L/min
CeO_2 Particle Size (mm)	3.0, 5.0, 6.0	ε	0.65
		P	3.5 Kw
		$\dot{V}$	1.8 L/min

3.2.7. Validation. To reduce the influences of mesh number and quality on the simulation results, the mesh independency analysis was applied to this study. Three different cell base sizes were selected to study the average temperature of the catalyst region for 10 minutes pre-heating process. The relation between cell numbers and temperatures is shown in Figure 4. With the mesh number increasing, the temperature differences between 400,000 case and 960,000 cases are almost negligible, especially for the gas phase. Therefore, the mesh number reaches a stable level. Considering the accuracy and calculation cost for the transient model, the mesh with 400,000 cells was selected in the following study.

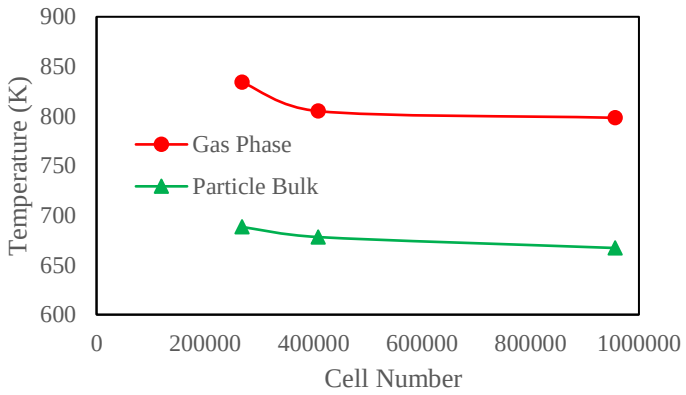

Figure 4. Mesh independency analysis.

The time-spatial analysis was applied to this model to ensure the time step is accurate enough to describe the processes in the reactor. Four different time steps (0.5s, 1s, 2s, and 3s) were used in the 20 minutes pre-heating process. The temperature was monitored by adding a vertical line probe in the center of the catalyst. Figure 5 shows the relation between temperature and position at the moment of 20 minutes under various

time steps. The spatial-dependent temperature profiles have the same shape and the maximum difference is less than 4%, which is in the tolerable range. Comprehensively considering the transient simulation target, the accuracy, and the calculation cost, 2s time step was chosen in the following simulations.

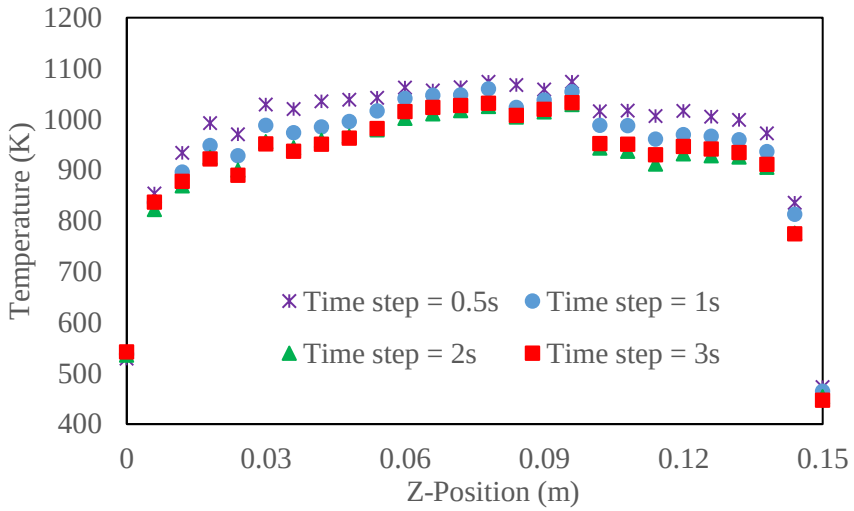

Figure 5. Time-spatial analysis.

The thermodynamic and CeO_2 reduction models were validated against the experimental results obtained by Bulfin et al. [44], which used 100 W concentrated radiation power on a CeO_2 pellet (5 mm diameter and 1 mm height) with 65% void fraction. It is visible from Figure 5 that the temperature and non-stoichiometric coefficient of CeO_2 derived from the numerical model demonstrate comparable values to those derived from the experiment, with slight differences caused by influences of experimental setups and operating limitations [44].

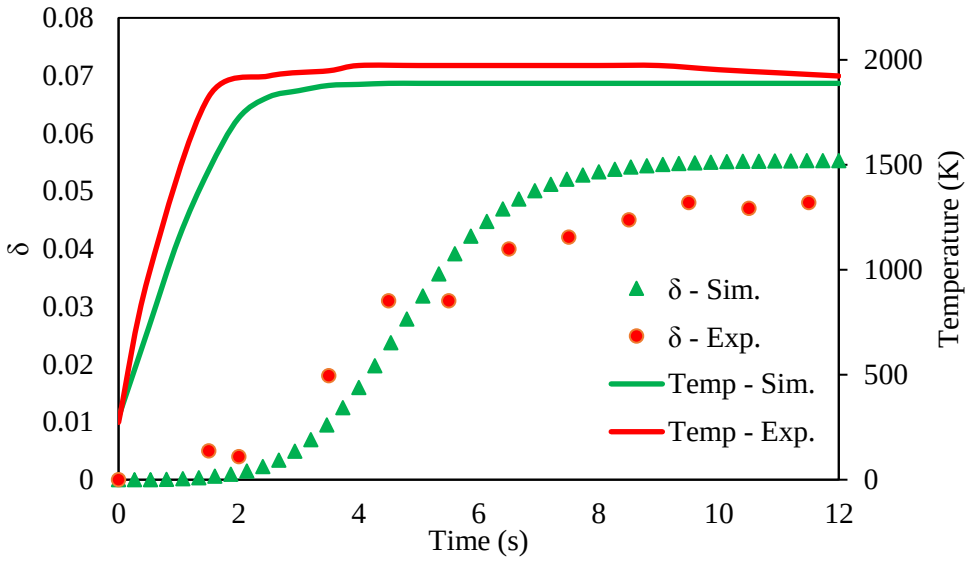

Figure 6. Validation of thermodynamic and chemical reaction models.

4. MODELING RESULTS AND DISCUSSIONS

4.1. GAS FLOW RATE

The purge gas is essential in CeO_2 reduction to remove generated O_2 from the particle surface to avoid the recombination with reduced CeO_2. In this work, the influences of the inlet gas flow rate are discussed. Inlet gas consists of Ar and 10 ppm O_2, which was applied to stimulate reduction. Three different flow rates were studied to compare the impacts on the temperatures and the O_2 evolution rates during the reduction process. The transient temperature profiles of the gas and the particle phase are shown in Figure 7. The results reveal that the temperature differences are too small to distinguish under the given 15 mins reaction time. To clarify the results, temperature distributions between 10 mins and 15 mins are enlarged. From the enlarged temperature profiles, the 1.8 L/min inlet gas flow rate shows relatively higher average temperatures in both phases.

As slow gas flow rate takes less cold fluid to the reactive region, the convection losses are smaller than that of large gas flow rate. However, the temperature differences between 1.8 L/min and 3.2 L/min are 5 K and 0.5 K for gas phase and particle phase, respectively. This result reveals that various inlet gas flow rates have a negligible influence on temperature distribution under the current range. Since the input radiant power is large enough to control the temperature distribution, the influence on convection caused by gas flow changes small and may be ignored. The O_2 evolution rate reveals a similar result (Figure 8). The peak reaction rates between 1.8 L/min and 3.2 L/min is less than 0.01 mL min^{-1} g^{-1} CeO_2. Even though the gas flow rate may impact the O_2 evolution rate, the result is not obvious under current operating conditions.

4.2. SOLAR RADIANT POWER

Solar radiant power is a significant factor in CeO_2 reduction rate since it supplies the required thermal energy to support the endothermic reduction reaction. Four various radiant power levels between 3.0 kW and 4.5 kW were selected to investigate their influence on the reactive region, including incident radiation, temperature distribution, and reduction rate. Figure 9 (a) shows the scattering distribution of the radiant flux of the catalyst region's inner surface after 15 mins. The Z positive direction is towards the solar receiver window. Higher input power results in higher radiant flux (as high as $4\times 10^6\ W\ m^{-2}$), which also shows that the radiant flux is lower at the ceria top, even though the power is uniformly distributed on the surface. This phenomenon is caused by the diffuse radiation property. In this case, it is assumed that diffuse radiation works in the domains. Since the view factors are evenly distributed in all directions, less radiation

accumulates at the top of the ceria domain, which results in a low radiant flux. Additionally, the radiant flux intervals for the different input power levels are nearly equal (consistent with Eq. (15)). The variations of radiant flux on radial direction can be reflected via temperature distribution, as shown in Figure 9 (b). Here, three different levels (top, middle, and bottom) were chosen to investigate the temperature profiles considering both radial and axial influences. At the top level, the temperature is the lowest with a relatively uniform distribution in the radial direction. This is due to the fluid not directly contacting the radiation absorption solid with a low-radiant flux. At the middle and bottom levels, the temperature profile distributions gradually decrease. Since incident radiation decreases due to absorption by solid particles which then radiate radiation, the radiation term in Eq. (18) decreases in the radial direction, which is consistent with a decrease temperature. Due to the high radiant flux to the middle level, the temperature is also higher.

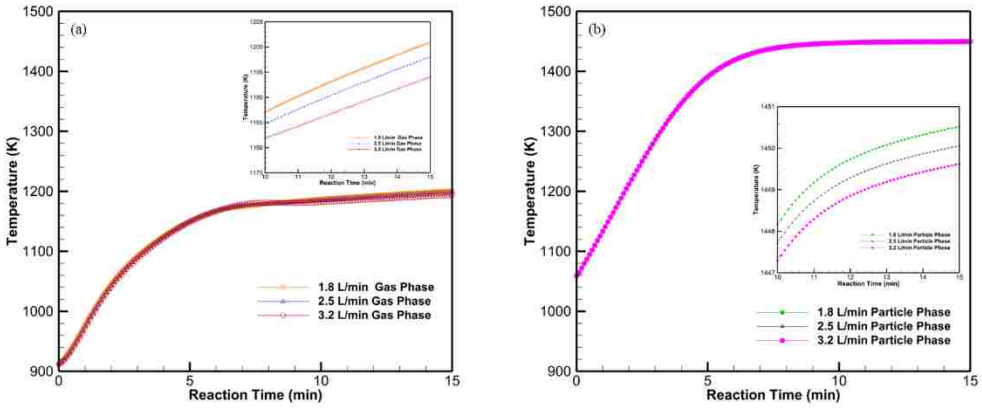

Figure 7. Temperature profiles of various inlet gas flow rate: (a) gas phase; (b) particle phase.

The transient results under different input power are shown in Figure 9 (c) and (d). Figure 9 (c) shows the average temperature variations of the gas and particle phase in their respective domain during the 15 min reaction time. Since particles have higher specific heat and have better radiant properties compared with gases (Ar and O2 are weak radiation absorbing species [80]), the particle phase temperatures are higher than the gas phases (the difference between gas phase and particle phase is around 300 K).

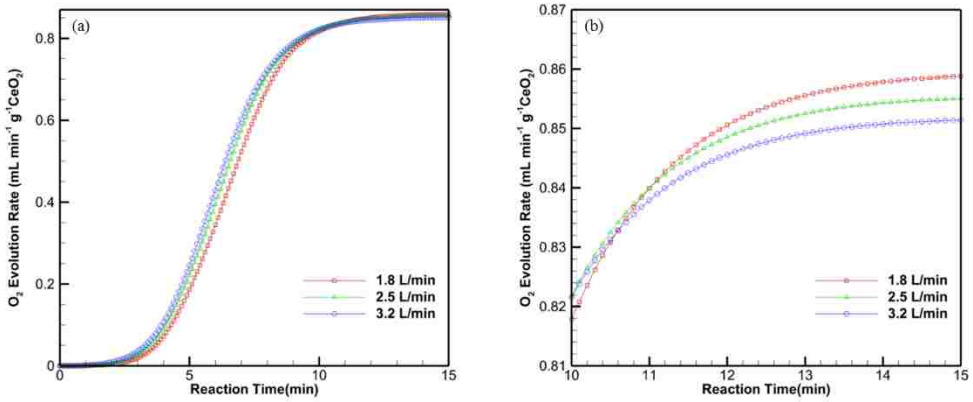

Figure 8. Oxygen evolution rates of various inlet gas flow rate.

Figure 9 (d) presents that reactive region under a 4.5 kW power input which produces the highest O_2 formation rate due to its high temperature. Additionally, reaction rates sharply increase after 5 mins, due to temperature exceeds the minimum required reduction temperature (higher than 1000 °C, shown in Figure 9 (c)). After 10 mins, the average gas and particle phase temperatures of the reactive region stabilize, which provides a constant reaction rate. Under 3.5 kW power input, the peak O_2 evolution rate reaches 0.8 mL min^{-1} g^{-1} CeO_2, which is comparable to that reported in the literature [81].

With 4.5 kW power input, the peak O_2 evolution rate reaches 1.18 mL min^{-1} g^{-1} CeO_2. The results show that higher power input provides a higher temperature in the reactive domain and correspondingly leads to higher O_2 production. However, this observation does not mean the power input can continue to be increased without bound. An optimal power input should also consider solar-to-fuel efficiency. Eq. (7) shows the theoretical solar-to-fuel efficiency ignoring the energy of purge gas [33].

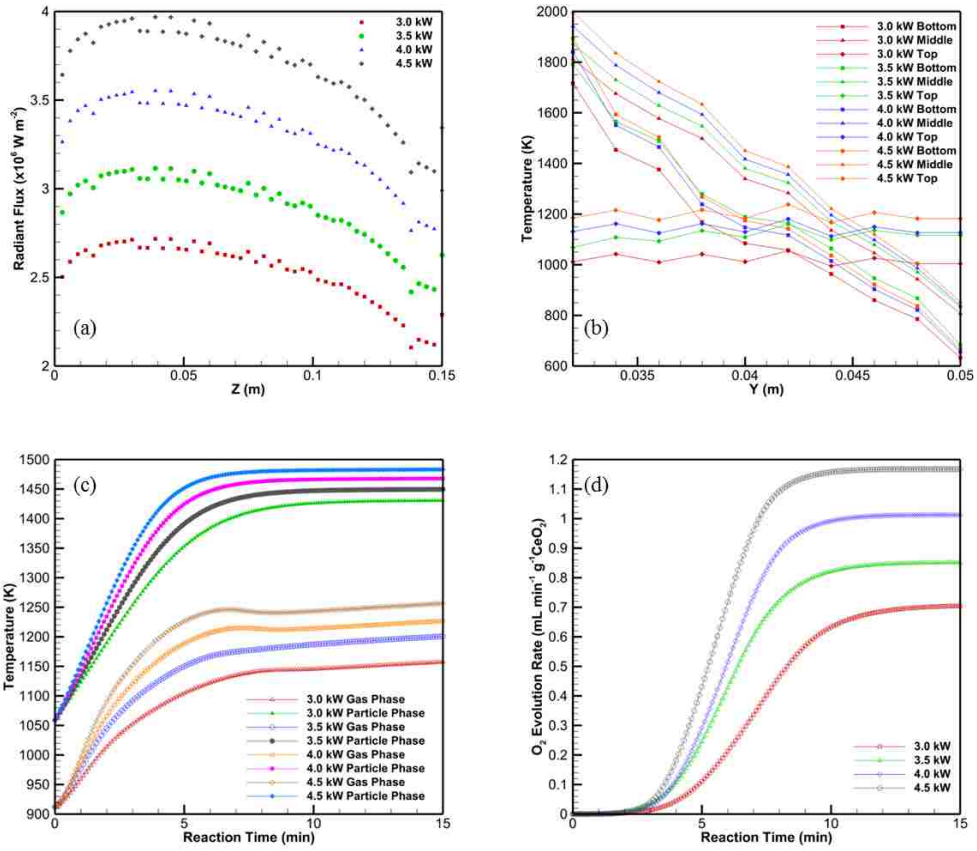

Figure 9. Profiles of various radiant powers: (a) radiant flux distributions along the axial direction; (b) temperature distributions along the radial direction; (c) transient temperature of fluid and particles; (d) oxygen evolution rates.

4.3. CeO_2 VOID FRACTION

Besides the influences caused by the operating condition, CeO_2 morphology is also extremely important in the reduction process. In this work, DEM particles are used to approximate porous media via random injection, which provided similar gas paths among particles. Heat and mass transfer are considered macroscopically, which only occurs on the surface of particles by neglecting particles pores.

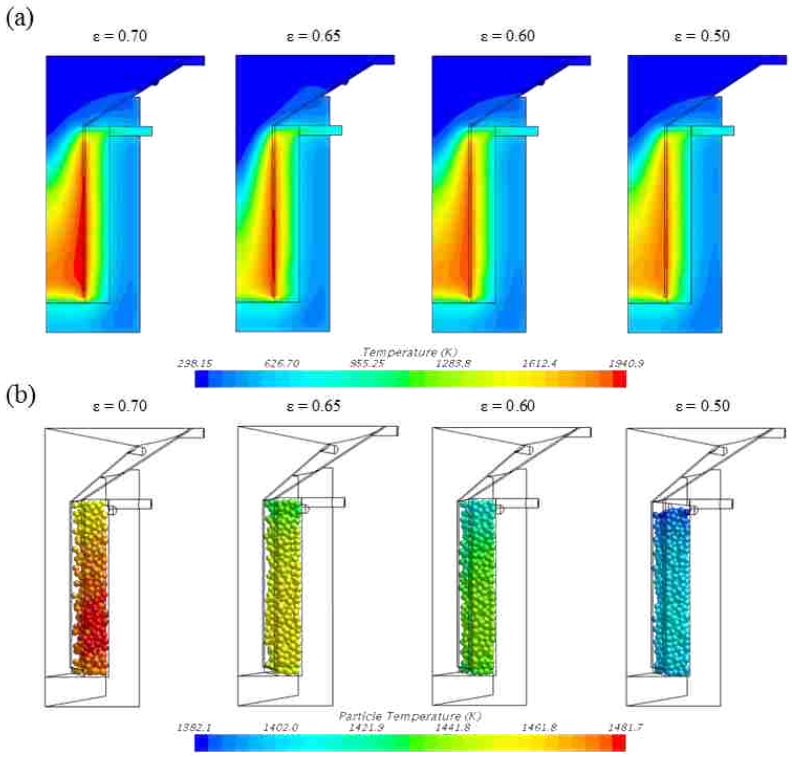

Figure 10. Simulated (a) gas phase and (b) particle phase temperature profiles under various CeO_2 void fractions.

In this work, four different void fractions (0.7, 0.65, 0.6, and 0.5) were considered to study temperature distributions and corresponding O_2 evolution rates. Using the same

particle size to fill the reactor's reactive region, a large void fraction implies that the packing is less dense, which provides less pressure drop in the packed section. Also, a larger void fraction allows incident radiation to penetrate deeper into the reactor radial direction, which results in higher reaction temperature. The resulting temperature distributions for the gas and particle phases are shown in Figure 10 which confirms that tighter (lower void fraction) packing results in low-temperature distributions for the gas and particle phases consistent with expectation, while higher void fraction (less tightly packed section) results in a higher temperature.

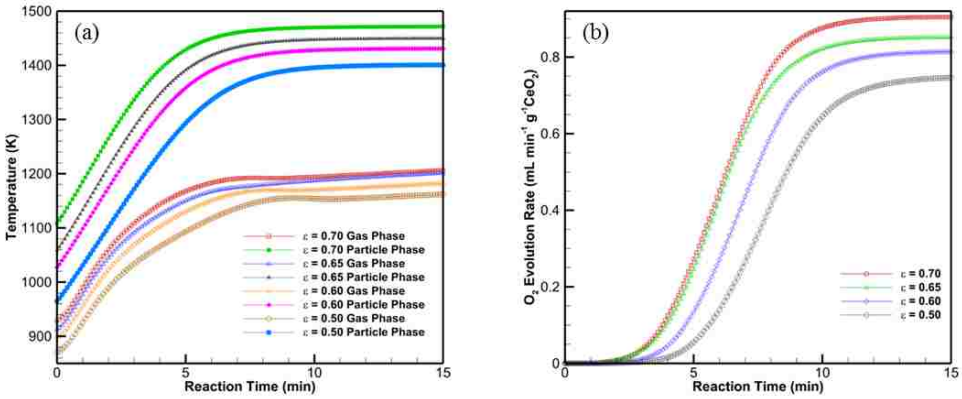

Figure 11. Time-dependent variable profiles under different void fractions: (a) average temperature; (b) O_2 evolution rates.

Figure 11 shows the time-dependent temperature profiles and O_2 evolution rates. As discussed above, the average temperatures of gas and particle phases are different due to the physical and material properties. In Figure 11 (a), particle temperature increases with an increased void fraction. However, the gas phase temperatures remain essentially constant for void fractions between ε=0.7 and ε=0.65 during the reduction process. From

Eq. (18) and (21), the primary heat transfer mechanism is convection from both the fluid-wall exchange and fluid-particle convection. When ε=0.65, the fluid-wall convection is greater but has a smaller energy source term for the particle phase. Under the current geometry, the fluid-wall convection and fluid-particle source term are balanced, which results in the close temperature distribution with ε=0.70. A similar temperature distribution leads to a similar O_2 evolution rate in a section with increasing temperature. In Figure 11 (b), the O_2 evolution rate is almost the same in the initial 7 mins for the void fractions between ε=0.7 and ε=0.65 due to a uniform temperature profile. After that, the temperatures are stable, which reflects a stable oxygen generation rate with a slight difference. Since O_2 evolution rate is based on per gram CeO_2, ε=0.70 has a higher rate caused by the lower mass amount of CeO_2 under a similar temperature condition. In order words, the catalyst with a void fraction of 0.7 can provide better heat transfer and achieve higher temperature distribution, which leads to a higher O_2 evolution rate.

4.4. CeO_2 PARTICLE SIZE

CeO_2 particle size is another important factor that affects the structure of the reactive section. Under the same void fraction, smaller particles provide a more total specific surface area in the reactor. As O_2 evolution reaction occurs on the surface of CeO_2 particles, the larger specific surface area is beneficial to the reaction rate. However, smaller particles mean tighter packing, which is adverse to radiative heat transfer. Therefore, the influence of particle sizes may be dual directions. Figure 12 shows the temperature profiles of the gas phase and particle phase with ε=0.65 under various particle diameters. The result reveals that larger particles have advantages of deriving

higher temperature since more incident radiation can reach particle surfaces due to the larger interspace between particles, which is shown in Figure 12 (b).

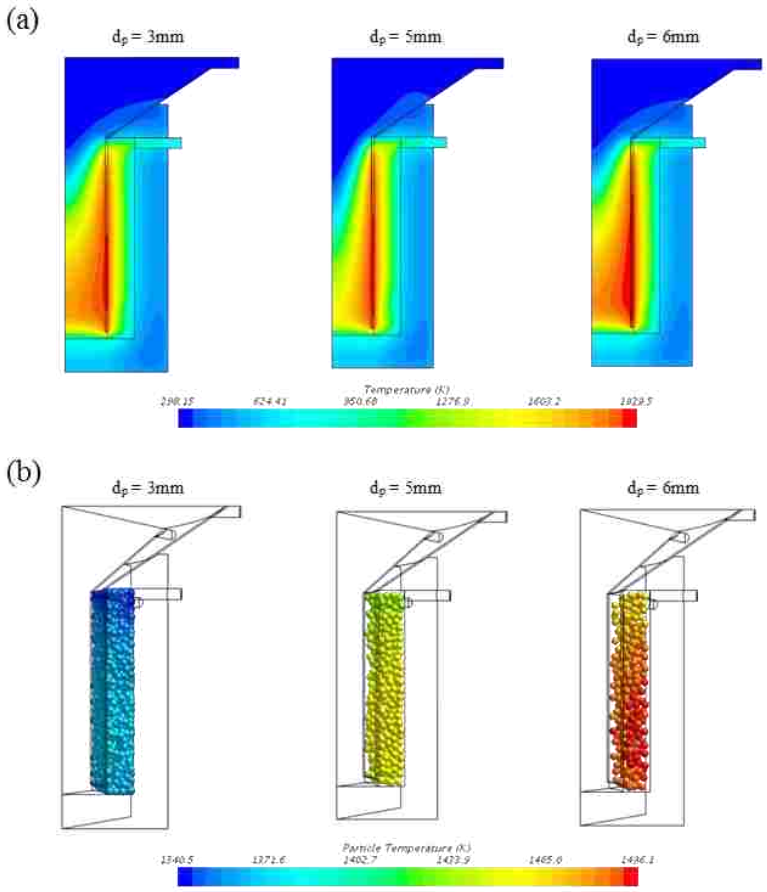

Figure 12. Simulated (a) gas phase and (b) particle phase temperature profiles under different particle sizes.

The transient variations of temperatures and O_2 evolution rates are presented in Figure 13. From Figure 13 (a), the particle temperature differences between d_p=3 mm and d_p=6 mm are distinct. The particle diameter d_p=3 mm gets a 150 K lower average particle temperature than that of d_p=6 mm. Compared with the temperature profile with other

cases, d_p=3 mm derives the lowest temperature than other cases, which reveals that particle size has a stronger influence on temperature than other factors. Even though the temperature differences between different particle sizes are obvious, the gas phase temperatures seem discrepant. The gas phase temperature seems very close under different conditions, especially for d_p=5 mm and d_p=6 mm. The result illustrates that the influence of particle-gas convection is weaker than that of gas-wall convection. In Figure 13 (b), d_p=3 mm shows the highest O_2 evolution rate under these three cases, which is opposite to temperature results. As discussed above, specific surface area and temperature are both significant to the reaction rate. Under the CeO_2 reduction process, the specific surface area is dominant.

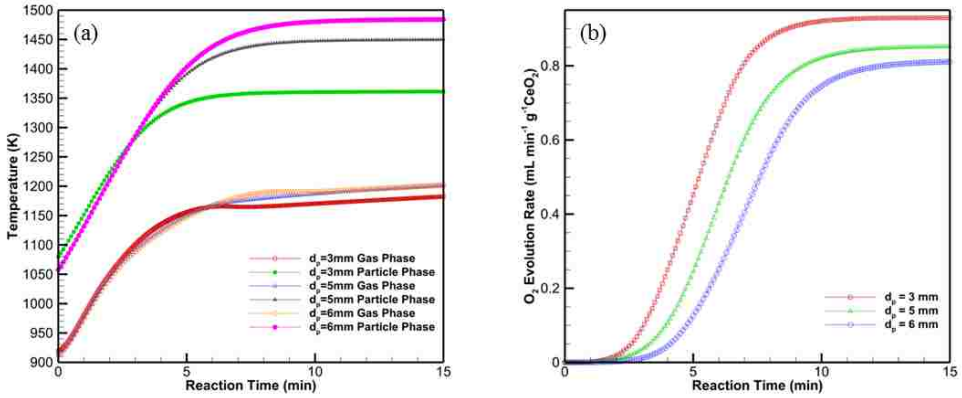

Figure 13. Time-dependent variable profiles under different particle sizes: (a) average temperature; (b) O_2 evolution rates.

5. CONCLUSIONS

The DEM method was successfully employed to simulate the porous CeO_2 structure in the transient CFD modeling of CeO_2 reduction in a solar thermochemical reactor. Model validation was accomplished according to previously reported experimental data. The effects of the catalyst textures (particle size and void fraction) and reaction conditions (gas flow rate and radiative power input) on the temperature profiles and reaction rate were investigated. The gas flow rate showed slightly influences on both the temperature distribution and reaction rates. The temperature is higher at a lower flow rate leading to a higher reaction rate. The higher solar radiant power input results in higher temperature and O_2 evolution rate. A larger void fraction of the catalyst is advantageous to improve the thermal performances and CeO_2 reduction rate. The reaction rate is remarkably enhanced by shrinking the particle size to derive more specific surface area of the catalyst. Further studies will focus on the study of CO_2 splitting via reduced CeO_2 and experimental validation of the thermal and reactive performances.

ACKNOWLEDGEMENT

We gratefully acknowledge the financial support from the Wayne and Gayle Laufer Foundation.

REFERENCES

[1] IEA Finds CO2 Emissions Flat for Third Straight Year Even as Global Economy Grew in 2016, (2017). https://www.iea.org/newsroom/news/2017/march/iea-finds-co2-emissions-flat-for-third-straight-year-even-as-global-economy-grew.html.

[2] C. Breyer, D. Bogdanov, A. Aghahosseini, A. Gulagi, M. Child, A.S. Oyewo, J. Farfan, K. Sadovskaia, P. Vainikka, Solar photovoltaics demand for the global energy transition in the power sector, Prog. Photovoltaics Res. Appl. 26 (2018) 505–523.

[3] T. Zhu, K. Swaminathan-Gopalan, K. Stephani, E. Ertekin, Thermoelectric phonon-glass electron-crystal via ion beam patterning of silicon, Phys. Rev. B. 97 (2018) 174201.

[4] I. Dincer, C. Acar, A review on clean energy solutions for better sustainability, Int. J. Energy Res. 39 (2015) 585–606.

[5] J. Xu, F. Wang, C. Lv, H. Xie, Carbon emission reduction and reliable power supply equilibrium based daily scheduling towards hydro-thermal-wind generation system: A perspective from China, Energy Convers. Manag. 164 (2018) 1–14.

[6] N.E. Vaughan, C. Gough, S. Mander, E.W. Littleton, A. Welfle, D.E.H.J. Gernaat, D.P. Van Vuuren, Evaluating the use of biomass energy with carbon capture and storage in low emission scenarios, Environ. Res. Lett. 13 (2018) 44014.

[7] V.N. Nguyen, L. Blum, Syngas and synfuels from H2O and CO2: Current status, Chemie Ing. Tech. 87 (2015) 354–375.

[8] T. Fu, Z. Li, Review of recent development in Co-based catalysts supported on carbon materials for Fischer–Tropsch synthesis, Chem. Eng. Sci. 135 (2015) 3–20.

[9] D.B. Bukur, B. Todic, N. Elbashir, Role of water-gas-shift reaction in Fischer–Tropsch synthesis on iron catalysts: A review, Catal. Today. 275 (2016) 66–75.

[10] P.G. Loutzenhiser, A. Steinfeld, Solar syngas production from CO 2 and H 2 O in a two-step thermochemical cycle via Zn/ZnO redox reactions: thermodynamic cycle analysis, Int. J. Hydrogen Energy. 36 (2011) 12141–12147.

[11] D. Dardor, R.R. Bhosale, S. Gharbia, A. Kumar, F. AlMomani, Solar carbon production via thermochemical ZnO/Zn carbon dioxide splitting cycle, J. Emerg. Trends Eng. Appl. Sci. 6 (2015) 129–135.

[12] P.G. Loutzenhiser, M.E. Gálvez, I. Hischier, A. Graf, A. Steinfeld, CO2 splitting in an aerosol flow reactor via the two-step Zn/ZnO solar thermochemical cycle, Chem. Eng. Sci. 65 (2010) 1855–1864.

[13] R. Müller, A. Steinfeld, H2O-splitting thermochemical cycle based on ZnO/Zn-redox: Quenching the effluents from the ZnO dissociation, Chem. Eng. Sci. 63 (2008) 217–227.

[14] M.E. Galvez, P.G. Loutzenhiser, I. Hischier, A. Steinfeld, CO2 splitting via two-step solar thermochemical cycles with Zn/ZnO and FeO/Fe3O4 redox reactions: thermodynamic analysis, Energy & Fuels. 22 (2008) 3544–3550.

[15] S. Abanades, H.I. Villafan-Vidales, CO 2 and H 2 O conversion to solar fuels via two-step solar thermochemical looping using iron oxide redox pair, Chem. Eng. J. 175 (2011) 368–375.

[16] A. Stamatiou, P.G. Loutzenhiser, A. Steinfeld, Solar syngas production via H2O/CO2-splitting thermochemical cycles with Zn/ZnO and FeO/Fe3O4 redox reactions, Chem. Mater. 22 (2009) 851–859.

[17] J.R. Scheffe, A. Steinfeld, Oxygen exchange materials for solar thermochemical splitting of H 2 O and CO 2: a review, Mater. Today. 17 (2014) 341–348.

[18] S. Abanades, P. Charvin, F. Lemont, G. Flamant, Novel two-step SnO2/SnO water-splitting cycle for solar thermochemical production of hydrogen, Int. J. Hydrogen Energy. 33 (2008) 6021–6030.

[19] A. Iwase, S. Yoshino, T. Takayama, Y.H. Ng, R. Amal, A. Kudo, Water splitting and CO2 reduction under visible light irradiation using Z-scheme systems consisting of metal sulfides, CoOx-loaded BiVO4, and a reduced graphene oxide electron mediator, J. Am. Chem. Soc. 138 (2016) 10260–10264.

[20] T. Kawada, S. Hinokuma, M. Machida, Structure and SO3 decomposition activity of nCuO–V2O5/SiO2 (n= 0, 1, 2, 3 and 5) catalysts for solar thermochemical water splitting cycles, Catal. Today. 242 (2015) 268–273.

[21] W.C. Chueh, C. Falter, M. Abbott, D. Scipio, P. Furler, S.M. Haile, A. Steinfeld, High-flux solar-driven thermochemical dissociation of CO2 and H2O using nonstoichiometric ceria, Science (80-.). 330 (2010) 1797–1801.

[22] M. Romero, A. Steinfeld, Concentrating solar thermal power and thermochemical fuels, Energy Environ. Sci. 5 (2012) 9234–9245.

[23] P.G. Loutzenhiser, A. Meier, A. Steinfeld, Review of the two-step H2O/CO2-splitting solar thermochemical cycle based on Zn/ZnO redox reactions, Materials (Basel). 3 (2010) 4922–4938.

[24] J. Nie, Y. Chen, B. Wong, L.C. Brown, Numerical modeling of vapor condensation during cadmium quenching process in a solar receiver, in: ASME 2009 3rd Int. Conf. Energy Sustain. Collocated with Heat Transf. InterPACK09 Conf., American Society of Mechanical Engineers, 2009: pp. 943–950.

[25] S. Abanades, P. Charvin, F. Lemont, G. Flamant, Novel two-step SnO 2/SnO water-splitting cycle for solar thermochemical production of hydrogen, Int. J. Hydrogen Energy. 33 (2008) 6021–6030.

[26] K.-S. Kang, C.-H. Kim, W.-C. Cho, K.-K. Bae, S.-H. Kim, C.-S. Park, Novel two-step thermochemical cycle for hydrogen production from water using germanium oxide: KIER 4 thermochemical cycle, Int. J. Hydrogen Energy. 34 (2009) 4283–4290.

[27] P. Charvin, S. Abanades, G. Flamant, F. Lemort, Two-step water splitting thermochemical cycle based on iron oxide redox pair for solar hydrogen production, Energy. 32 (2007) 1124–1133.

[28] C.L. Muhich, B.D. Ehrhart, I. Al ‐ Shankiti, B.J. Ward, C.B. Musgrave, A.W. Weimer, A review and perspective of efficient hydrogen generation via solar thermal water splitting, Wiley Interdiscip. Rev. Energy Environ. 5 (2016) 261–287.

[29] A.H. McDaniel, A. Ambrosini, E.N. Coker, J.E. Miller, W.C. Chueh, R. O'Hayre, J. Tong, Nonstoichiometric perovskite oxides for solar thermochemical H2 and CO production, Energy Procedia. 49 (2014) 2009–2018.

[30] K. Otsuka, M. Hatano, A. Morikawa, Hydrogen from water by reduced cerium oxide, J. Catal. 79 (1983) 493–496.

[31] G.R. Bamwenda, H. Arakawa, Cerium dioxide as a photocatalyst for water decomposition to O 2 in the presence of Ce aq 4+ and Fe aq 3+ species, J. Mol. Catal. A Chem. 161 (2000) 105–113.

[32] S. Abanades, G. Flamant, Thermochemical hydrogen production from a two-step solar-driven water-splitting cycle based on cerium oxides, Sol. Energy. 80 (2006) 1611–1623.

[33] R. Bader, R.B. Chandran, L.J. Venstrom, S.J. Sedler, P.T. Krenzke, R.M. De Smith, A. Banerjee, T.R. Chase, J.H. Davidson, W. Lipiński, Design of a solar reactor to split CO2 via isothermal redox cycling of ceria, J. Sol. Energy Eng. 137 (2015) 31007.

[34] P. Furler, J.R. Scheffe, A. Steinfeld, Syngas production by simultaneous splitting of H2O and CO 2 via ceria redox reactions in a high-temperature solar reactor, Energy Environ. Sci. 5 (2012) 6098–6103.

[35] P. Furler, J. Scheffe, M. Gorbar, L. Moes, U. Vogt, A. Steinfeld, Solar thermochemical CO2 splitting utilizing a reticulated porous ceria redox system, Energy & Fuels. 26 (2012) 7051–7059.

[36] L.J. Venstrom, N. Petkovich, S. Rudisill, A. Stein, J.H. Davidson, The effects of morphology on the oxidation of ceria by water and carbon dioxide, J. Sol. Energy Eng. 134 (2012) 11005.

[37] L.O. Schunk, P. Haeberling, S. Wepf, D. Wuillemin, A. Meier, A. Steinfeld, A receiver-reactor for the solar thermal dissociation of zinc oxide, J. Sol. Energy Eng. 130 (2008) 21009.

[38] N. Gokon, H. Murayama, A. Nagasaki, T. Kodama, Thermochemical two-step water splitting cycles by monoclinic ZrO2-supported NiFe2O4 and Fe3O4 powders and ceramic foam devices, Sol. Energy. 83 (2009) 527–537.

[39] M. Chambon, S. Abanades, G. Flamant, Thermal dissociation of compressed ZnO and SnO2 powders in a moving‐front solar thermochemical reactor, AIChE J. 57 (2011) 2264–2273.

[40] J. Lapp, J.H. Davidson, W. LipiĹ, Heat transfer analysis of a solid-solid heat recuperation system for solar-driven nonstoichiometric redox cycles, J. Sol. Energy Eng. 135 (2013) 31004.

[41] A. de la Calle, A. Bayon, Annual performance of a thermochemical solar syngas production plant based on non-stoichiometric CeO2, Int. J. Hydrogen Energy. 44 (2019) 1409–1424.

[42] A.J. Groehn, A. Lewandowski, R. Yang, A.W. Weimer, Hybrid radiation modeling for multi-phase solar-thermal reactor systems operated at high-temperature, Sol. Energy. 140 (2016) 130–140.

[43] B. Bulfin, F. Call, M. Lange, O. Lubben, C. Sattler, R. Pitz-Paal, I. V Shvets, Thermodynamics of CeO2 thermochemical fuel production, Energy & Fuels. 29 (2015) 1001–1009.

[44] B. Bulfin, A.J. Lowe, K.A. Keogh, B.E. Murphy, O. Lubben, S.A. Krasnikov, I. V Shvets, Analytical model of CeO2 oxidation and reduction, J. Phys. Chem. C. 117 (2013) 24129–24137.

[45] M. Zinkevich, D. Djurovic, F. Aldinger, Thermodynamic modelling of the cerium–oxygen system, Solid State Ionics. 177 (2006) 989–1001.

[46] T. Ishida, N. Gokon, T. Hatamachi, T. Kodama, Kinetics of thermal reduction step of thermochemical two-step water splitting using CeO2 particles: Master-plot method for analyzing non-isothermal experiments, Energy Procedia. 49 (2014) 1970–1979.

[47] J. Valle-Hernández, H. Romero-Paredes, C.A. Arancibia-Bulnes, H.I. Villafan-Vidales, G. Espinosa-Paredes, Modeling of a CeO2 thermochemistry reduction process for hydrogen production by solar concentrated energy, in: AIP Conf. Proc., AIP Publishing, 2016: p. 120008.

[48] P.J. Valades-Pelayo, H.I. Villafán-Vidales, H. Romero-Paredes, C.A. Arancibia-Bulnes, Modeling of a tubular solar reactor for continuous reduction of CeO2: The effect of particle size and loading on radiative heat transfer and conversion, Chem. Eng. Sci. 162 (2017) 77–87.

[49] J. Valle-Hernández, H. Romero-Paredes, A. Pacheco-Reyes, Modeling of the steam hydrolysis in a two-step process for hydrogen production by solar concentrated energy, in: AIP Conf. Proc., AIP Publishing, 2017: p. 100016.

[50] D. Arifin, A.W. Weimer, Kinetics and mechanism of solar-thermochemical H2 and CO production by oxidation of reduced CeO2, Sol. Energy. 160 (2018) 178–185.

[51] J.R. Scheffe, A.H. McDaniel, M.D. Allendorf, A.W. Weimer, Kinetics and mechanism of solar-thermochemical H 2 production by oxidation of a cobalt ferrite–zirconia composite, Energy Environ. Sci. 6 (2013) 963–973.

[52] F.A. Kröger, H.J. Vink, Relations between the concentrations of imperfections in crystalline solids, in: Solid State Phys., Elsevier, 1956: pp. 307–435.

[53] J.R. Scheffe, A. Steinfeld, Thermodynamic analysis of cerium-based oxides for solar thermochemical fuel production, Energy & Fuels. 26 (2012) 1928–1936.

[54] R. Bader, L. Gampp, T. Breuillé, S. Haussener, A. Steinfeld, W. Lipiński, Unsteady Radiative Heat Transfer Model of a Ceria Particle Suspension Undergoing Solar Thermochemical Reduction, J. Thermophys. Heat Transf. 33 (2018) 63–77.

[55] Y. Tsuji, T. Kawaguchi, T. Tanaka, Discrete particle simulation of two-dimensional fluidized bed, Powder Technol. 77 (1993) 79–87.

[56] X. Ku, T. Li, T. Løvås, CFD–DEM simulation of biomass gasification with steam in a fluidized bed reactor, Chem. Eng. Sci. 122 (2015) 270–283.

[57] H. Ma, L. Xu, Y. Zhao, CFD-DEM simulation of fluidization of rod-like particles in a fluidized bed, Powder Technol. 314 (2017) 355–366.

[58] G. Zhang, M. Gutierrez, M. Li, A coupled CFD-DEM approach to model particle-fluid mixture transport between two parallel plates to improve understanding of proppant micromechanics in hydraulic fractures, Powder Technol. 308 (2017) 235–248.

[59] S. Bellan, K. Matsubara, H.S. Cho, N. Gokon, T. Kodama, A CFD-DEM study of hydrodynamics with heat transfer in a gas-solid fluidized bed reactor for solar thermal applications, Int. J. Heat Mass Transf. 116 (2018) 377–392.

[60] S. Bellan, K. Matsubara, C.H. Cheok, N. Gokon, T. Kodama, CFD-DEM investigation of particles circulation pattern of two-tower fluidized bed reactor for beam-down solar concentrating system, Powder Technol. 319 (2017) 228–237.

[61] S. Bellan, N. Gokon, K. Matsubara, H.S. Cho, T. Kodama, Numerical and experimental study on granular flow and heat transfer characteristics of directly-irradiated fluidized bed reactor for solar gasification, Int. J. Hydrogen Energy. 43 (2018) 16443–16457.

[62] S. Bellan, N. Gokon, K. Matsubara, H.S. Cho, T. Kodama, Heat transfer analysis of 5kWth circulating fluidized bed reactor for solar gasification using concentrated Xe light radiation, Energy. 160 (2018) 245–256.

[63] S. Bellan, T. Kodama, K. Matsubara, N. Gokon, H.S. Cho, K. Inoue, Thermal performance of a 30 kW fluidized bed reactor for solar gasification: A CFD-DEM study, Chem. Eng. J. 360 (2019) 1287–1300.

[64] A.B. Morris, Z. Ma, S. Pannala, C.M. Hrenya, Simulations of heat transfer to solid particles flowing through an array of heated tubes, Sol. Energy. 130 (2016) 101–115.

[65] STAR-CCM+ Theory Guid v. 12.02, Siemens AG, 2017.

[66] STAR-CCM+ User Mannul v. 12.02, 2017.

[67] W.E. Ranz, W.R. Marshall, Evaporation from drops, Chem. Eng. Prog. 48 (1952) 141–146.

[68] D. Marxer, P. Furler, M. Takacs, A. Steinfeld, Solar thermochemical splitting of CO 2 into separate streams of CO and O 2 with high selectivity, stability, conversion, and efficiency, Energy Environ. Sci. 10 (2017) 1142–1149.

[69] P. Furler, A. Steinfeld, Heat transfer and fluid flow analysis of a 4 kW solar thermochemical reactor for ceria redox cycling, Chem. Eng. Sci. 137 (2015) 373–383.

[70] Y.S. Touloukian, Thermophysical Properties of High Temperature Solid Materials. Volume 4. Oxides and Their Solutions and Mixtures. Part 1. Simple Oxygen Compounds and Their Mixtures, THERMOPHYSICAL AND ELECTRONIC PROPERTIES INFORMATION ANALYSIS CENTER LAFAYETTE IN, 1966.

[71] C.L. Yaws, Thermophysical properties of chemicals and hydrocarbons, William Andrew, 2008.

[72] STAR-CCM+ Material Databases, Siemens AG, 2017.

[73] P. Richet, Y. Bottinga, L. Denielou, J.P. Petitet, C. Tequi, Thermodynamic properties of quartz, cristobalite and amorphous SiO2: drop calorimetry measurements between 1000 and 1800 K and a review from 0 to 2000 K, Geochim. Cosmochim. Acta. 46 (1982) 2639–2658.

[74] S. Andre, A. Degiovanni, A theoretical study of the transient coupled conduction and radiation heat transfer in glass: phonic diffusivity measurements by the flash technique, Int. J. Heat Mass Transf. 38 (1995) 3401–3412.

[75] V.P. Nicolau, M. Borges, L.M.S. Silva, Radiative properties of glass and coatings, in: 3rd Eur. Conf. Energy Perform. Indoor Clim. Build., 2002: pp. 835–840.

[76] B.J. McBride, S. Gordon, M.A. Reno, Coefficients for calculating thermodynamic and transport properties of individual species, (1993).

[77] D. Zimmermann, Flow Modeling of a Solar Thermogravimeter, Master Thesis ETH Zurich, 2012.

[78] H.J.M. Hanley, R.D. McCarty, J. V Sengers, Viscosity and thermal conductivity coefficients of gaseous and liquid oxygen, (1974).

[79] P.A. Cundall, O.D.L. Strack, A discrete numerical model for granular assemblies, Geotechnique. 29 (1979) 47–65.

[80] M.Q. Brewster, Thermal radiative transfer and properties, John Wiley & Sons, 1992.

[81] L.J. Venstrom, R.M. De Smith, R. Bala Chandran, D.B. Boman, P.T. Krenzke, J.H. Davidson, Applicability of an equilibrium model to predict the conversion of CO2 to CO via the reduction and oxidation of a fixed bed of cerium dioxide, Energy & Fuels. 29 (2015) 8168–8177.

II. INVESTIGATING INFLUENCES OF GEOMETRIC FACTORS ON A SOLAR THERMOCHEMICAL REACTOR FOR TWO-STEP CARBON DIOXIDE SPLITTING VIA CFD MODELS

Han Zhang and Joseph D. Smith

Department of Chemical and Biochemical Engineering, Missouri University of Science and Technology, 1101 North State Street, Rolla, MO 65409, United States

ABSTRACT

Solar thermochemical processes offer pathways to store solar energy as chemical fuels. Some elevated temperature reactions, like production of syngas and methane reforming, are anticipated in solar reactors which can provide extremely high temperatures. A novel partition cavity-receiver reactor concept is proposed in this paper. In order to provide a longer pathway of interaction between the catalyst and reactants, a partition is introduced in this cavity-receiver reactor. A numerical computational fluid dynamics (CFD) analysis is performed to study the influences of geometric factors (e.g., gap size between partition and bottom, inlets/outlets position, catalyst thickness) under both uniform and concentrated radiant fluxes. A two-step solar thermochemical redox reaction using ceria as a catalyst to split CO_2 was modeled in the partition cavity-receiver reactor to investigate the relationship between geometric factors and reaction rates. Based on the comparisons and analysis of results, the reactor structure with thinner catalyst region and higher catalyst loading quantity is favorable for obtaining a higher solar-to-fuel efficiency.

Keywords: *Solar energy, Solar thermochemical reactor, Radiative transfer, DEM, CeO_2 reduction.*

NOMENCLATURE

Symbols		**Greek Symbols**	
A	area (m^2)	β	extinction coefficient
d	collector aperture diameter (m)	δ	non-stoichiometric coefficient
f	focal length (m)	η	efficiency
$\boldsymbol{F}$	force (N)	μ	dynamic viscosity (Pa·s)
$\boldsymbol{F_s}$	particle surface force (N)	ρ	density (kg m^{-3})
$\boldsymbol{g}$	gravitational acceleration (m s^{-2})	σ	Stefan-Boltzmann constant
G	Incident radiative heat flux (W m^{-2})	ψ	angle (rad)
h	collector height (m)	Ω	solid angle
h	enthalpy (J kg^{-1})	**Subscripts**	
I	radiative intensity (W m^{-2})	b	body
$\boldsymbol{I}$	identity matrix	conv	convection
k	thermal conductivity (W m^{-1} K^{-1})	E	energy
k_a	absorption coefficient (m^{-1})	f	fluid
k_{pa}	particle absorption coefficient (m^{-1})	fp	fluid-particle interphase
k_{ps}	particle scattering coefficient (m^{-1})	fs	fluid-solid interphase
k_{red}	reduction rate coefficient	fuel	chemical fuel

k_s	scattering coefficient (m^{-1})	m	mass
m_f	final particle mass (kg)	p	particles
m_i	initial particle mass (kg)	pb	particle black body
M	molecular weight ($kg.mol^{-1}$)	q	quartz glass
n	amount of substance (mol)	rad	radiation
p	pressure (Pa)	reac	reaction
q_r	re-radiation ($W\ m^{-2}$)	rim	rim
Q	heat amount (J)	s	solid
$Q_{a,p}$	absorption efficiency of particle	solar	solar energy
r	reaction rate ($mol\ s^{-1}$)	t	total
s	distance in Ω direction	th	thermal
S	source term	V	momentum
t	time (s)		
T	temperature (K)	**Abbreviation**	
$\boldsymbol{v}$	velocity ($m\ s^{-1}$)	CFD	Computational Fluid Dynamics
V	volume (m^3)	DEM	Discrete Element Method
x	material reacted ratio	DNI	Direct Normal Irradiance
Y_i	component concentration	DOM	Discrete Ordinate Method
		HHV	Higher Heating Value
		MCRT	Monte Carlo Ray Tracing

1. INTRODUCTION

With the development of renewable energy, solar energy is more and more popular in the commercial market. Thanks to the Solar Investment Tax Credit (ITC), solar energy growth has experienced an explosive increase, which keeps an average installation growth rate of 59% yearly (SEIA, 2018). Solar photovoltaics is the most

important application among numerous solar applications (Energysage, 2018). The main reason is that solar photovoltaics is one of the earliest solar energy branches and directly provides energy conversion from solar power to electricity. However, as the renewable energy application is no longer confined to power generation, more and more demands are based on energy storage.

Solar thermochemical processes provide the opportunity to store solar energy in chemical fuels, which conquers the limitations of intermittence and locality. Additionally, concentrated solar power can provide extremely high heat flux, a promising approach for replacing traditional heating methods used in elevated temperature chemical reactions that produce fuels.

Solar thermochemical processes can be briefly divided into two types based on applications: fuel production and industrial utilization. Solar thermochemical processes generally implement endothermic industrial processes that require high energy, like metal, lime, and ammonia production (Balomenos et al., 2009; Meier et al., 2005; Michalsky et al., 2012; Steinfeld et al., 1993; Wieckert et al., 2009).

The applications of the solar thermochemical processes in the fuel production, especially for hydrogen and syngas, primarily have three aspects: solar thermolysis, hydrocarbon feed processes, and thermochemical cycles (Yadav and Banerjee, 2016). Solar thermolysis is one of the earliest methods to decompose water to hydrogen and oxygen by a single step. However, the reaction requires an extremely high temperature, normally higher than 2500 K, with a relatively low yield of 2.69% (Baykara, 2004). Since the reaction conditions are so strict, and hydrogen and oxygen are hard to separate, solar thermolysis of water is still in the conceptual stage. Hydrocarbon feed fuel production is

another attractive solar thermochemical process. One of the representatives is solar methane reforming. Based on the reactor types and catalytic materials, a great many projects have contributed to the development of solar methane reforming (Gokon et al., 2014; Möller et al., 2006; Muir et al., 1993; Petrasch and Steinfeld, 2007). Except for gaseous hydrocarbon feed, solar thermochemical processes are also used in the gasification of complex hydrocarbon materials, like coal and biomass (Piatkowski et al., 2011; Vidal et al., 2010; Wieckert et al., 2013). Solar thermochemical cycles were proposed based on the idea of solar thermolysis. Due to the difficulties of decomposition temperature and product separation, solar thermochemical cycles utilize catalysts (metal oxides) to accomplish CO_2/H_2O splitting in two steps. In this way, the reduction temperature can be remarkably decreased, as the decomposition of metal oxide requires lower energy than water thermolysis. Besides, as O_2 is released in reduction and exits the reactor with the carrier gas, it maximally reduces the O_2 that is mixed with fuel gases.

Cerium dioxide is an outstanding catalyst in two-step solar thermochemical cycles due to its fast-redox kinetics and stable solid structure at high temperatures (Chueh et al., 2012; Zinkevich et al., 2006). The ceria two-step solar thermochemical cycles can be represented by the following equations.

High-temperature endothermic reduction:
$$CeO_2 \rightarrow CeO_{2-\delta} + \frac{\delta}{2} O_2 \quad (1)$$

Low-temperature exothermic oxidation:
$$CeO_2 \rightarrow CeO_{2-\delta} + \frac{\delta}{2} O_2 \quad (2)$$

$$CeO_{2-\delta} + \delta H_2O \rightarrow CeO_2 + \delta H_2 \quad (3)$$

During the solar thermochemical cycle, ceria is reduced to a non-stoichiometric status by using δ to represent the reduced level. It is reported that δ is up to 0.2 due to the

crystal structure (Panlener et al., 1975). An inertial carrier gas is essential to purge generated O_2 out of the reactor during the reduction to avoid recombination. CeO_2 reduction is activated when the temperature rises above1273 K with concentrated solar power (Scheffe and Steinfeld, 2014). Since reduction is an endothermic process, the input solar source needs to cover the heat requirements of both reactor temperature rising and reaction enthalpy. The splitting of CO_2/H_2O is an exothermic oxidation process in which CO_2/H_2O reacts with non-stoichiometric CeO_2 and loses oxygen. This reduced ceria ($CeO_{2-\delta}$) oxidizes to CeO_2 and releases CO/H_2. The oxidation typically happens when the temperature is lower than 1273 K (Furler et al., 2012). As CO_2 and H_2O splitting are two independent processes, the products can be CO, H_2, or syngas based on the feedstock. The solar-to-fuel efficiency of the entire process can be theoretically expressed as

$$\eta_{th} = \frac{n_{fuel} HHV_{fuel}}{Q_{solar}} \tag{4}$$

where n_{fuel} is the amount of product, HHV_{fuel} is the fuel higher heating value, and Q_{solar} is the input solar energy. In this case, the energy from inertial gas is ignored.

Solar thermochemical reactors can be classified as directly-irradiated reactors and indirectly-irradiated reactors based on the role of radiation in the reactor, as solar energy is the core heat source. In indirectly-irradiated reactors, the concentrated solar power does not contact the reactive materials. Radiation is absorbed by the opaque outer shell of the catalyst. The main heat transfer approach in the reactive region is convection and conduction. Tubular reactors are the dominant type of indirectly-irradiated reactors, either with a single tube or a group of tubes. Indirectly-irradiated reactors are widely used in the

solar methane reforming process, as traditional tubular reactor material, like stainless steel, can afford only limited reaction temperatures and the fabrication is relatively undemanding (Anikeev and Kirillov, 1991; Gokon et al., 2014; Yu et al., 2017). Indirectly-irradiated reactors are also used in solar thermochemical cycles to split CO_2 and H_2O (Bader et al., 2015; Lichty et al., 2012). However, the development of indirectly-irradiated reactors in solar thermochemical cycles has a non-negligible restriction: the tubular material. Since the reduction of solar thermochemical cycles usually requires the temperature to be as high as 2000K, materials with high melting points like SiC and alumina meet the reaction condition. Due to the weakness of heat transfer and rigorous material requirements, indirectly-irradiated reactors are not the mainstream of solar thermochemical cycles.

Directly-irradiated reactors have experienced a flourishing development in the application of solar thermochemical cycles during the last few decades. Among diversified types of reactors, three typical reactor configurations are meaningful. Moving front reactors use a moving center shaft to hold catalysts exposed in the radiative cavity to decompose under high temperatures. Since the catalysts used in moving front reactors are volatile, such as ZnO/Zn and SnO_2/SnO, the fresh catalyst can be exposed under radiation due to the loss of catalyst in the gas phase (Chambon et al., 2011; Schunk et al., 2008). The obvious shortcoming of moving front reactors is that the catalyst surface exposed under radiation is confined by the center shaft, which severely affects the pilot scale of this type of reactor. Another type of reactor is the traditional packed-bed reactor which has multitudinous advantages for catalyst reactions based on different fields of study. This concept was applied by Chueh et al. (Chueh et al., 2012) to solar

thermochemical cycles with ceria reticulated porous ceramic foam. As it is a cavity-receiver reactor, the catalyst surface can be effectively exposed under the radiation. Instead of the complicated configuration of other directly-irradiated reactors, packed bed reactors provide an opportunity for a pilot scale view of solar thermochemical cycles. As solar thermochemical cycles have two steps with different temperatures, continuous operation can only be accomplished by alternatively using reducing and oxidizing processes. Directly-irradiated rotary reactors run reduction and oxidation simultaneously by adding a rotary monolith catalyst, with the axis perpendicular to the reactor axis, to separate the reactor into two regions for reduction and oxidation (Kaneko et al., 2007; Lapp et al., 2013; Miller et al., 2012). The rotary reactor provides the chance to operate continuously, which is significant for the industrialization of solar thermochemical cycles.

In this paper, a directly-irradiated partition-cavity solar thermochemical reactor is proposed for solar thermochemical cycles. For the purpose of optimizing reactor performance, some geometry factors, such as partition gap size, catalyst thickness, and inlets and outlets position, are studied based on fluid flow and heat transfer performances. A three-dimensional (3D) transient computational fluid dynamics (CFD) model is set up by applying the discrete element method (DEM) to simulate the catalyst structure under the uniform radiative flux and concentrated radiative flux. Monte Carlo Ray Tracing (MCRT) is applied to track the paths of the concentrated rays with a self-designed solar collector. CeO_2 reduction performance is studied in the optimized geometry designs under the concentrated radiative flux in order to show how the geometry performs under reaction.

2. PROBLEM STATEMENT

The schematic diagram of the partition-cavity solar reactor is shown in Figure 1. The reactor consists of a cylindrical reactive chamber and a transparent quartz window at the top. In the reactive chamber, an annular catalyst domain is the core section with a 100 mm outer diameter and 100 mm height. Between the annular catalyst and cavity, a transparent quartz partition separates the catalyst from the cavity with a reasonable gap at the bottom to leave space for fluid entering the catalyst region. This partition not only prolongs contact between the gas mixture and the catalyst but also allows radiation to directly enter the catalyst region with minimum loss. The cavity works as a preheating chamber for the incoming cold fluid to avoid the catalyst contact with the cold gas directly. The concentrated solar radiation enters the reactor from the quartz window at the top, touches the partition inner surface, and is then transferred to the catalyst region (porous ceria). A ceramic insolation material, Al_2O_3-SiO_2, covers the outer layer of the catalyst region to reduce thermal loss. The above regions are sealed in a stainless-steel reactor shell.

Some geometric factors may affect the heat transfer and reaction performance of the reactor. In this paper, three key parameters, partition gap size, inlets/outlets position, and catalyst thickness, are studied to understand their influences. The first two parameters focus on flow pattern effects, but the third focuses on radial heat transfer.

In this study, using CFD, a quarter of the entire reactor was selected to simulate the geometric parameters assuming the two cut surfaces as periodic surfaces. CeO_2 particles were packed into the catalyst region using a random injector which formed a porous structure. The DEM method was introduced to set up the transfer relations with

between fluids and particles. Argon performed as the inert carrier gas for heat transfer and purged O_2, which exited the reactor in the preheating and the reduction processes, respectively. Under uniform radiant flux, the radiation power was assumed to be distributed on the cavity and partition/catalyst interface uniformly. Under the concentrated radiant flux, the solar radiation was concentrated by a self-designed parabolic dish collector via the MCRT approach. The ray distribution results were converted to the radiant flux by post-processing in MATLAB. Then the concentrated radiant flux was used to diffuse the radiant flux boundary condition on the cavity and partition/catalyst interface.

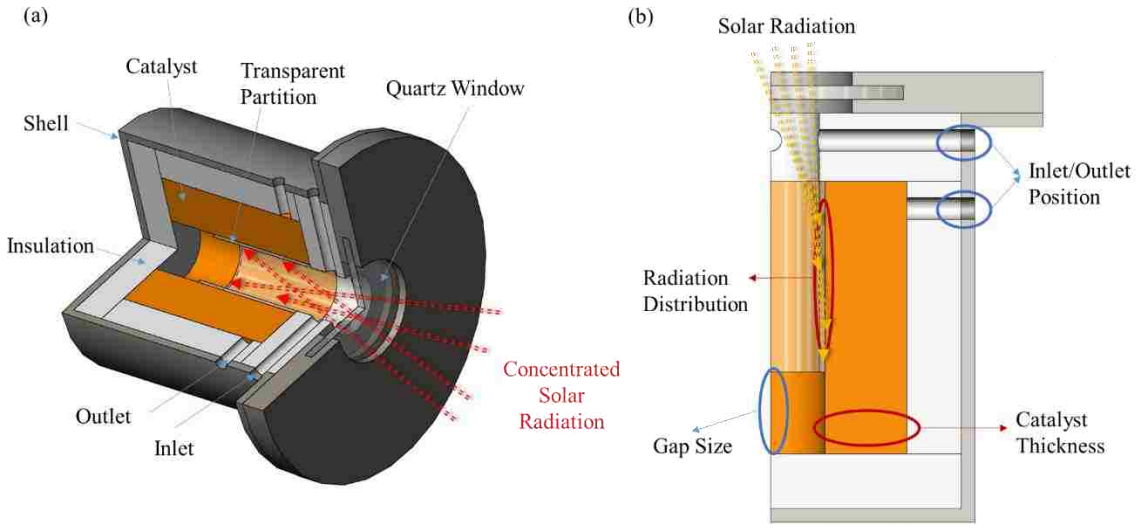

Figure 1. Partition-cavity solar reactor schematic diagram: (a) reactor configuration; (b) quarter reactor model and studied parameters.

3. METHODS

3.1. GOVERNING EQUATIONS

The continuous and discrete domains of the quarter partition-cavity solar reactor are shown in Figure 2 (a) and (b), respectively. For the continuous phase, the inlet, the outlet, and the cavity were non-reactive fluid regions and the catalyst was a reactive fluid region. The partition and insulation were solid phases. The discrete particle phase was coupled with the catalyst fluid phase using DEM. The discrete ordinate method (DOM) of radiation operated in both continuous and discrete phases.

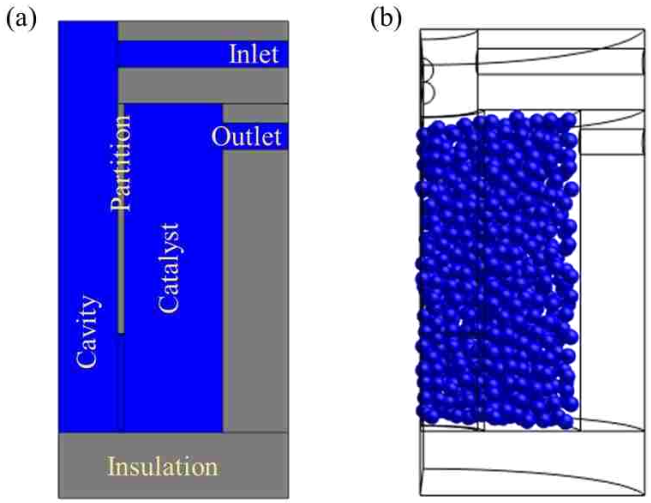

Figure 2. Regions of the reactor model: (a) continuous phase; (b) discrete phase.

3.1.1. Momentum Conservation. The momentum conservation equations for the fluid phase and the discrete phase are as follows:

$$\frac{\partial(\rho_f \boldsymbol{v})}{\partial t} + \nabla \cdot \left(\rho_f \boldsymbol{v}\boldsymbol{v}\right) = -\nabla p + \nabla \cdot \mu \left(\nabla \boldsymbol{v} + (\nabla \boldsymbol{v})^T - \frac{2}{3}\boldsymbol{I}\nabla \cdot \boldsymbol{v}\right) + \rho_f \boldsymbol{g} \quad (5)$$

$$\frac{\partial(\rho_f \boldsymbol{v})}{\partial t} + \nabla \cdot \left(\rho_f \boldsymbol{v}\boldsymbol{v}\right) = -\nabla p + \nabla \cdot \mu \left(\nabla \boldsymbol{v} + (\nabla \boldsymbol{v})^T - \frac{2}{3}\boldsymbol{I}\nabla \cdot \boldsymbol{v}\right) + \rho_f \boldsymbol{g} + S_V \quad (6)$$

$$m_p \frac{d\boldsymbol{v_p}}{dt} = \boldsymbol{F_s} + \boldsymbol{F_b} \quad (7)$$

$$S_V = -\frac{1}{\Delta t}\sum\nolimits_{\pi}\left(\int_t^{t+\Delta t}\int_{V_c} \delta(\boldsymbol{r} - \boldsymbol{r_\pi}) n_\pi \left(\boldsymbol{F_s} + \dot{m}_p \boldsymbol{v_p}\right) dV dt\right) \quad (8)$$

where ρ_f is fluid density, $\boldsymbol{v}$ is fluid velocity vector, p is pressure, μ is fluid dynamic viscosity, $\boldsymbol{I}$ is identity matrix, S_V is momentum source term, m_p is particle mass, $\boldsymbol{v_p}$ is particle velocity vector, $\boldsymbol{F_s}$ is particle surface force, and $\boldsymbol{F_b}$ is particle body force. Eq. (6) and (5) are the momentum conservation equations of the catalyst region and all other fluid regions. Eq. (7) is the momentum conservation of discrete particles with consideration of the interaction source term conveyed in Eq. (8). As particles are discrete, the momentum conservation is expressed based on force form: only drag force, pressure gradient, gravity, and contact force are considered.

3.1.2. Energy Conservation. Since radiation plays an important role in heat transfer in this study, the partition is the only region that has direct radiation. The other regions are only involved in re-radiation. The energy conservation equation for the partition domain is as follows:

$$\frac{\partial(\rho_q h_q)}{\partial t} + \nabla \cdot \left(\rho_q h_q \boldsymbol{v}\right) = \nabla \cdot \left(k_q \nabla T\right) + S_{E,rad} \quad (9)$$

where ρ_q is partition quartz glass density, h_q is partition enthalpy, k_q is partition thermal conductivity, and $S_{E,rad}$ is the energy source term including direct radiation and re-radiation. Since CeO_2 particles are also considered to participate in radiation, the

radiative transfer equation should not only consider the influences on the continuous phase, but also the effects of particle radiation. The radiative transfer equation can be solved as follows:

$$\frac{dI}{ds} = -\beta I + k_a I_b + \frac{k_s}{4\pi}\int_{4\pi} I(\Omega)d(\Omega) + k_{pa} I_{pb} + \frac{k_{ps}}{4\pi}\int_{4\pi} I(\Omega)d(\Omega) \tag{10}$$

where I is radiative intensity, I_b is back body radiative intensity, I_{pb} is particle black body intensity, Ω is solid angle, s is distance in Ω direction, k_a is absorption coefficient, k_s is scattering coefficient, k_{pa} is particle absorption coefficient, k_{ps} is particle scattering coefficient, and β is extinction coefficient. The re-radiation term can be expressed as:

$$\nabla q_r = k_a(4\pi I_b - \int_{4\pi} I\, d\Omega) \tag{11}$$

In the reactive catalyst region, the energy conservation equation including the reaction enthalpy change is given by

$$\frac{\partial(\rho_f h_f)}{\partial t} + \nabla \cdot \left(\rho_f h_f \boldsymbol{v}\right) = \nabla \cdot \left(k_f \nabla T\right) + h_{fs} A_{fs}(T_s - T_f) + \nabla q_r + S_E \tag{12}$$

where h_f is heat transfer coefficient of fluid, k_f is thermal conductivity of fluid, h_{fs} is fluid-solid interface heat transfer coefficient, S_E is the energy source term expressed as a function of particle thermal properties, which can be shown as

$$S_E = -\frac{1}{\Delta t}\sum_{\pi}\left(\int_t^{t+\Delta t}\int_{V_c} \delta(\boldsymbol{r} - \boldsymbol{r_\pi}) n_\pi \left(Q_t + \boldsymbol{F_s}\cdot v_p + \frac{1}{2}\dot{m}_p \boldsymbol{v_p}^2 + \dot{m}_p h\right) dV dt\right) \tag{13}$$

The energy conservation of discrete particle phase is

$$m_p c_p \frac{dT_p}{dt} = Q_{conv} + Q_{rad} + Q_{reac} \tag{14}$$

where Q_{conv} is heat of convection between particle and fluid, Q_{rad} is radiative heat transfer rate, and Q_{reac} is heat of reaction. The expressions of Q_{conv} and Q_{rad} are

$$Q_{conv} = h_{fp} A_p (T - T_p) \tag{15}$$

$$Q_{rad} = \frac{A_p}{4} Q_{a,p} (G - 4\sigma T_p^4) \tag{16}$$

where h_{fp} is heat transfer coefficient between particle and fluid, A_p is particle surface area, $Q_{a,p}$ is particle absorption efficiency, G is incident radiative heat flux, and σ is the Stefan-Boltzmann constant. For the reduction process of ceria shown in Eq. (1), Q_{reac} is around 950 kJ/mol O_2 (Marxer et al., 2017).

3.1.3. Mass Conservation. The mass transfer primarily occurs in the catalyst domain, combining the influences of particles and fluid. The mass conservation equations of non-reactive catalyst and particle domains are as listed:

$$\frac{\partial(\rho_f Y_i)}{\partial t} + \nabla \cdot \left(\rho_f \boldsymbol{v} Y_i\right) = 0 \tag{17}$$

$$\frac{\partial(\rho_f Y_{O_2})}{\partial t} + \nabla \cdot \left(\rho_f \boldsymbol{v} Y_{O_2}\right) = S_{m,\,O_2} \tag{18}$$

$$\frac{dm_p}{dt} = \dot{m}_p \tag{19}$$

where Y_i is component concentration, $S_{m,\,O_2}$ is the mass source term from the reaction, and $\dot{m}_p$ is particle mass transfer rate. Since $S_{m,\,O_2}$ is from two-way coupling of fluid and particle, it can be expressed as:

$$S_{m,O_2} = -\frac{1}{\Delta t} \sum_{\pi} \left(\int_t^{t+\Delta t} \int_{V_c} \delta(\boldsymbol{r} - \boldsymbol{r_\pi}) n_\pi \dot{m}_p dV dt \right) \tag{20}$$

The CeO_2 devolatilization rate is the particle mass transfer rate, whose absolute value also equals O_2 generation rate. The reaction rate expression can be shown based on the particle mass changed fraction (Ishida et al., 2014):

$$\frac{dx}{dt} = k_{red}(1 - x) \tag{21}$$

$$x = \frac{m - m_i}{m_f - m_i} \tag{22}$$

where m, m_i, and m_f are time-dependent, initial, and final particle mass, and k_{red} is the reduction rate coefficient. Since the ratio of oxygen vacancy and Ce keeps a conservation of δ, the expression of *m* can be converted based on the reaction formula in Eq. (1).

$$m = m_i - \delta n_{CeO_2} M_{O_2}/2 \tag{23}$$

By re-arranging Eq. (21), the reaction rate is presented:

$$\frac{dm_p}{dt} = (m_f - m_i) \cdot \ k_{red} \cdot (1 + \frac{\delta \frac{m_i}{M_{CeO_2}} M_{O_2}}{2(m_f - m_i)}) \tag{24}$$

where δ is the reaction non-stoichiometric coefficient, which is a function of temperature and O_2 partial pressure (Bulfin et al., 2013):

$$\frac{\delta}{0.35 - \delta} = (\frac{106{,}000\ Pa}{P_{O_2}})^{0.217} \exp(\frac{-195.6\ kJ/mol}{RT}) \tag{25}$$

3.2. SOLAR COLLECTOR OPTICAL DESIGN

In this study, a parabolic dish solar collector is designed to introduce concentrated solar radiation in the partition-cavity reactor. The parabolic dish reactor can concentrate parallel solar rays to a focal point, which enhances the radiant flux on the reactor partition surface. The paraboloid of the revolution schematic diagram is depicted in Figure 3. The

parallel solar rays enter the paraboloid collector and the rays are concentrated on the focal point *F*. The focal length between the focal point and the vertex of the parabola is *f*. The parabolic rim angle (ψ_{rim}), paraboloid height (h), and aperture diameter (d) determine the collector morphology. The above parameters have the relations listed below:

$$\tan\psi_{rim} = \frac{1}{(d/8h) - (2h/d)} \tag{26}$$

$$h = \frac{d^2}{16f} \tag{27}$$

$$\frac{f}{d} = \frac{1}{4\tan(\psi_{rim}/2)} \tag{28}$$

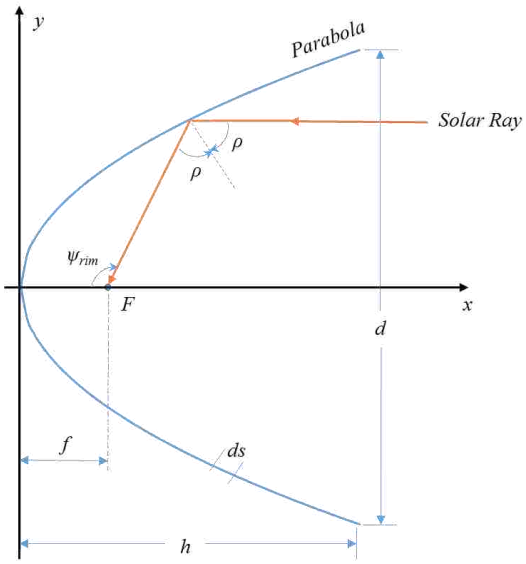

Figure 3. Paraboloid of revolution optical schematic diagram.

The four parameters are dependent on each other: when two of them are given, the others are discernible. In this case, the focal length is assumed to be 0.5 m with a rim angle of 60 degrees. From Eq. (27) and (28), the collector aperture diameter is 1.155 m

and the height is 0.167 m. The geometric concentration ratio is around 3100 with a total effective error of 4 mrad.

3.3. MONTE CARLO RAY TRACING

To simulate the concentrated radiant flux, the solar collector was simulated in an open source code, SolTrace, which utilizes MCRT to trace the path of the rays. The main concept of MCRT is to equally distribute solar power to a large number of rays with specific transmit directions, which are determined based on the sun shape and probability density function (Shuai et al., 2008). Transmissivity, reflectivity, and absorptivity are the key factors that affect the interactions between the rays and the receiver surface. The relations can be described by a group of statistical equations (Craig et al., 2016; Shuai et al., 2008). The radiant fluxes from Soltrace were further processed by a self-developed MATLAB code. This code created solar flux data files that were imported in STAR-CCM+ as radiative flux boundary conditions on the partition inner surface.

3.4. BOUNDARY AND INITIAL CONDITIONS

In this paper, the influences of geometric factors were first studied in the pre-heating condition, which only considered the momentum and heat transfer. Then, the comprehensive reaction case was implemented in the preferable geometries to test the performances of momentum, heat and mass transfer. The boundary and initial conditions of these two stages are listed in Table 1 and Table 2. The preheating and reduction began at 300 K and 1273 K, respectively. In both stages, the reactor operated under 1 atm. In

the preheating stage, pure Ar entered the reactor as carrier gas. In the reduction stage, 10^{-5} mole fraction of O_2 was added to gas mixture for stimulating the reduction. The properties of participated materials are listed in Table 3.

Table 1. Boundary conditions.

Surface	Boundary Conditions
Inlets	$v_{inlet} = \frac{\dot{V}}{A_{inlets}}$; $T_{inlet} = T_{initial}$
Outlets	$p_{out} = p_{atm}$
Partition inner surface	$k_q \frac{\partial T}{\partial n} = S_{E,rad} + h_q \Delta T$; ε=0.08, τ=0.86
Insulation inner surface	$k_s \frac{\partial T}{\partial n} = \Delta q_r + h_s \Delta T$; ε=0.28, τ=0.0
Cavity aperture	$T_{aperture} = T_{initial}$; ε=0.08, τ=0.86
All other surfaces	$\frac{\partial T}{\partial n} = 0$

The catalyst region was filled with 5 mm CeO_2 particles with a void fraction of 0.65. The inlet gas volume flow rate was 1.8 L/min. Inlets work as velocity inlets, whose velocity came from the division of gas volume flow rate and the inlet cross-sectional area. The inlet gas mixture temperature was equal to the initial temperature depending on the operating stage. In the preheating stage, the initial temperature equaled 300 K. In the CeO_2 reduction process, the initial temperature equaled 1273 K. The cavity aperture boundary was assumed isothermal with a temperature of 300 K. Since radiation was considered in both stages, the radiative properties were applied to related boundaries. The boundaries of partition and cavity aperture had a transmissivity of 0.86 and emissivity of

0.06 (Nicolau et al., 2002). For the boundaries of insulation, the transmissivity and emissivity equaled to 0.0 and 0.28, respectively (Furler and Steinfeld, 2015). The outer boundaries of insulation were assumed adiabatic, since the natural convection in the environment has a negligible influence on the heat and mass transfer in the reactive region. In the uniform radiant flux cases, 1 kW of solar power was distributed on the inner surface of the partition. In the concentrated radiant flux cases, the direct normal irradiance (DNI) was assumed to be 1000 W/m^2, which was concentrated by a parabolic dish collector with an aperture area of 1.047 m^2.

Table 2. Initial conditions.

Preheating	
Pressure	1 atm
Temperature ($T_{initial}$)	300 K
Species mole ratio ($Ar:O_2$)	1:0
CeO_2 Reduction	
Pressure	1 atm
Temperature ($T_{initial}$)	1273 K
Species mole ratio ($Ar:O_2$)	$1:10^{-5}$
Reaction Rate	0

The preheating and reduction began at 300 K and 1273 K, respectively. In both stages, the reactor operated under 1 atm. In the preheating stage, pure Ar entered the reactor as a carrier gas. In the reduction stage, 10^{-5} mole fraction of O_2 was added to the gas mixture for stimulating the reduction. The properties of participated materials are listed in Table 3.

Table 3. Material properties.

Component	Property	Expression	T(K)
CeO_2	Density (kg m^{-3}) (Furler and Steinfeld, 2015)	7220	298
	Specific heat (J kg^{-1} K^{-1}) (Furler and Steinfeld, 2015)	$-0.0001271 \cdot T^2 + 0.2697656 \cdot T + 299.8695684$	280-1100
		444.27	>1100
	Thermal conductivity (W $m^{-1}K^{-1}$) (Touloukian, 1966)	$-1.7234232 \cdot 10^{-9} \cdot T^3 + 1.1203174 \cdot 10^{-5} \cdot T^2 - 0.024019964 \cdot T + 17.800409$	280-2000
	Enthalpy of formation (J $kmol^{-1}$) (Yaws, 2008)	$-1.0887 \cdot 10^9$	298
Quartz Glass	Density (kg m^{-3}) (STAR-CCM+, 2017)	2500	298
	Specific heat (J mol^{-1} K^{-1}) (Richet et al., 1982)	$-0.0001 \cdot T^2 + 0.1791 \cdot T - 0.173$	273-847
		$0.0072 \cdot T + 61.717$	847-2000
	Thermal Conductivity (W $m^{-1}K^{-1}$) (Andre and Degiovanni, 1995)	$1.18 + 3.14 \times 10^{-3} \cdot T + 17966/T^2$	273-2000
Al_2O_3-SiO_2	Density (kg m^{-3}) (Furler and Steinfeld, 2015)	560.65	298
	Specific heat (J kg^{-1} K^{-1}) (Furler and Steinfeld, 2015)	$4 \cdot 10^{-7} \cdot T^3 + 1.3797 \cdot 10^{-3} \cdot T^2 + 1.5987289$	≤1480
		1118.44	>1480
	Thermal Conductivity (W $m^{-1}K^{-1}$) (Furler and Steinfeld, 2015)	$0.00012926 \cdot T + 0.019654$	280-2200
Argon	Viscosity (Pa · s) (Hanley and Ely, 1973)	$4.207 \cdot 10^{-6} + 6.85 \cdot 10^{-8} \cdot T - 2.046 \cdot 10^{-11} \cdot T^2 + 3.519 \cdot 10^{-15} \cdot T^3$	298-1000
		$5.55 \cdot 10^{-5}$	1000-2500
	C_p/R (McBride et al., 1993)	2.5	298-5000
	Thermal Conductivity (W $m^{-1}K^{-1}$) (Zimmermann, 2012)	$0.004834 + 4.83706 \cdot 10^{-5} \cdot T - 1.29 \cdot 10^{-8} \cdot T^2 + 2.3533 \cdot 10^{-12} \cdot T^3$	290-2400
Oxygen	Viscosity (Pa · s) (Crane, 1977; Haynes, 2014)	$2.018 \cdot 10^{-5} \cdot \frac{0.689 \cdot T}{T + 127}$	291.96
	C_p/R (McBride et al., 1993)	$3.7825 - 2.9967 \cdot 10^{-3} \cdot T + 9.8473 \cdot 10^{-6} \cdot T^2 - 9.6813 \cdot 10^{-9} \cdot T^3 + 3.2437 \cdot 10^{-12} \cdot T^4$	200-1000
		$3.6610 + 6.5637 \cdot 10^{-4} \cdot T - 1.4115 \cdot 10^{-7} \cdot T^2 + 2.0580 \cdot 10^{-11} \cdot T^3 - 1.2991 \cdot 10^{-15} \cdot T^4$	1000-5000
	Thermal Conductivity (W $m^{-1}K^{-1}$) (Hanley et al., 1974)	$7 \cdot 10^{-5} \cdot T + 0.007$	270-2500

3.5. NUMERICAL IMPLEMENTATION

The conservation equations were solved by the finite volume method with approximately 500,000 unstructured hexagonal mesh in STAR-CCM+ v. 12.06. The transient simulation was implemented by the first order implicit unsteady scheme with a time step of 0.2 s for the preheating and 0.5 s for the reduction. The calculation of transfer equations was executed by segregated flow/energy/species algorithms. The discrete CeO_2 particle phase is solved by the DEM solver (Cundall and Strack, 1979).

The non-stoichiometric CeO_2 reduction rate was solved by the user-defined field functions as a species source term. The concentrated solar collector simulation was implemented in Soltrace v. 2012.7.9. The sun shape was defined as pillbox with a 4.65 half-angle width. The DNI equals 1000 W/m^2 with 10000 desired rays. The radiation in the CFD model was implemented via discrete ordinates methods with 24 ordinates (S4) (Lathrop and Carlson, 1964). Simulations were accomplished on the high-performance cluster “FLARE”.

4. RESULTS AND DISCUSSIONS

4.1. PARTITION GAP SIZE

The purpose of the partition is to provide the preheating region and prolong the gas and catalyst contact path. Thus, the gap between the partition and insulation bottom has crucial influences on the momentum and heat transfer. In this study, four different gas sizes, 10 mm, 20 mm, 30 mm, and 40 mm, were simulated under the preheating setups to compare the results of velocity profiles and temperature distributions. Due to the slow

calculation speed of the 3D DEM model, a 2D model is applied to preliminarily estimate the flow patterns (Figure 4).

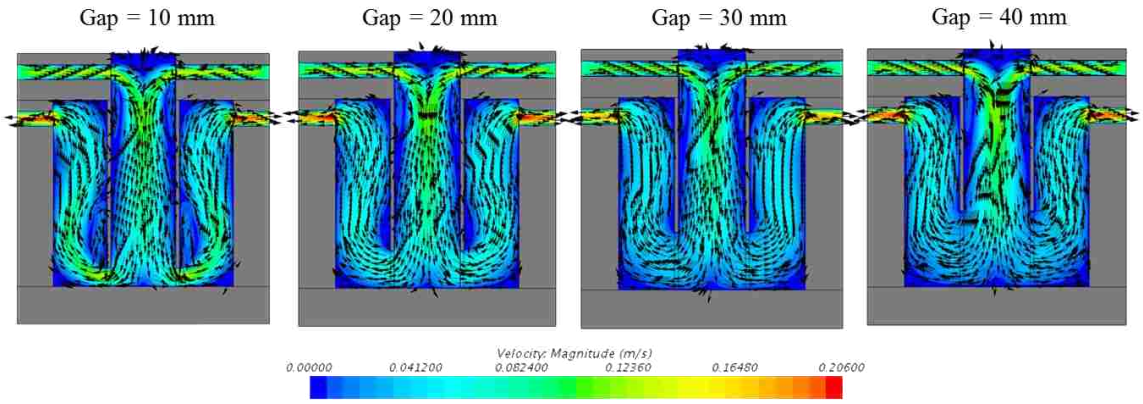

Figure 4. Velocity profiles of various gap sizes – 2D model.

From the contours in Figure 4, it is clearly seen that vortexes exist around the partition and gap connection region. With the gap size increasing, the vortexes diminish. These vortexes were caused by a small gap leading to a relatively high entering velocity speed in the catalyst region. Since the thickness of the catalyst region is finite, the velocity vectors may hit the side wall of the insulation, which changes the vector direction. As the flow streamline is not close to the partition-gap connection region, it forms a proximate dead zone with lower pressure, which also causes the formation of vortexes. Under the 10 mm and 20 mm gap size, the vortex can be clearly seen near the partition; however, the situation meliorates in the 30 mm and 40 mm gaps. Since the vortex is not a promising phenomenon, the 30 mm and 40 mm gaps show better velocity distributions under 2D contour.

To attain more accurate results, the quarter reactor model was simulated under 3D conditions to study the effects of gap size. The velocity contours and gap interface velocity distributions are shown in Figure 5 (a) and (b), respectively. With the consideration of the influence of the third dimension, the vortex does not apparently appear on the velocity profile of the periodic surface. Simultaneously, the velocity profiles of the catalyst region near the gap become less and less obvious from the 10 mm gap to the 40 mm gap. The reason can be explained by the velocity profiles of the gap interface in Figure 5 (b). When gap size equals 10 mm, the velocity shows a high value with relatively symmetric distribution between upper and lower limits. In this case, a narrow gap exerts like a nozzle, injecting high-velocity fluid into the catalyst domain. In the 20 mm, 30 mm, and 40 mm cases, the velocity distributions of the gas interface are no longer symmetric. The velocity is higher near the bottom insulation interface but lower near the partition interface. This phenomenon is caused by Newton's 2nd law of motion. The gas hits bottom insulation and receives an external force to change its momentum; therefore, the velocity shows higher near the bottom (Tait, 1899). Since the average gas velocity entering the catalyst region is lower due to the wider gap size, the velocity distribution in the catalyst region appears less evident but more homogeneous.

The average temperature distributions of the gas phase and particles in 120 s are presented in Figure 6. Figure 6 (a) shows the gas phase temperatures and particle surface temperatures under different gap sizes. Compared the four studied cases, the 10 mm gap case preserves a higher average temperature both in the gas phase and on the particle surfaces. With the gap size increases, the average temperatures gradually decrease in both phases. The gas phase temperature difference is less than 20 K in 120s between 10 mm

gap and 40 mm gap. The particle surface temperatures present as two groups: 10 mm and 20mm gap group and 30 mm and 40 mm group. The temperatures inside each group are extremely close, with only an estimated 10 K difference between the two groups.

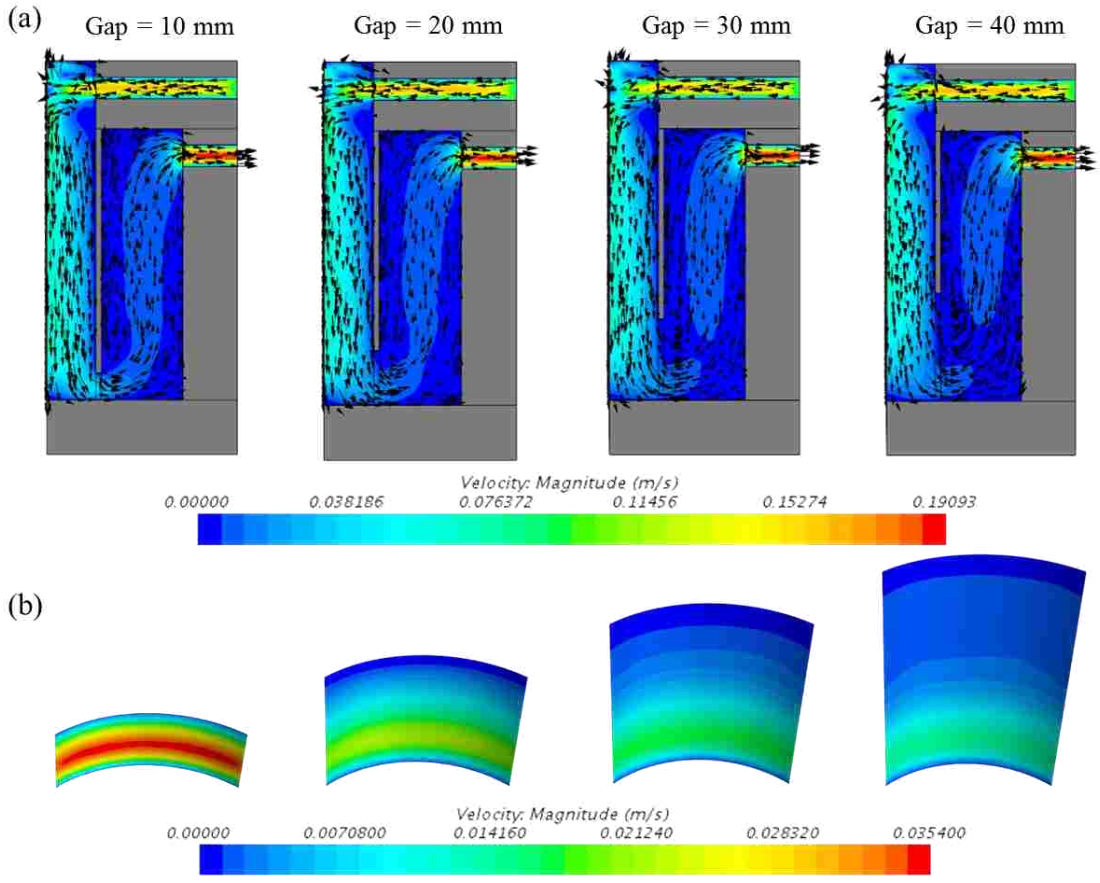

Figure 5. Velocity profiles of various gap sizes – 3D models: (a) velocity contour and vector on the periodic surface; (b) velocity contour on gap interface.

Additionally, the overall particle surface temperatures are higher than those of the gas phase. The reason is that particles participate in radiative transfer and possess higher specific heat capacity. Argon is proved to be weak radiation absorbing material, as the temperature rise is dominated by convection (Brewster, 1992). Since the 10 mm gap has a

longer partition for Ar to convect and absorb energy to increase temperature before entering the catalyst domain, the average temperature of the gas phase and particle surfaces shows higher temperature. The particle surface temperatures appearing in two groups are determined by velocity profiles. From Figure 5 (a), the 10 mm and 20 mm gaps show more clear velocity distributions in the catalyst region, which leads to higher temperatures. Similar velocity results appear for the 30 mm and 40 mm gap cases, which also reveals close temperature profiles.

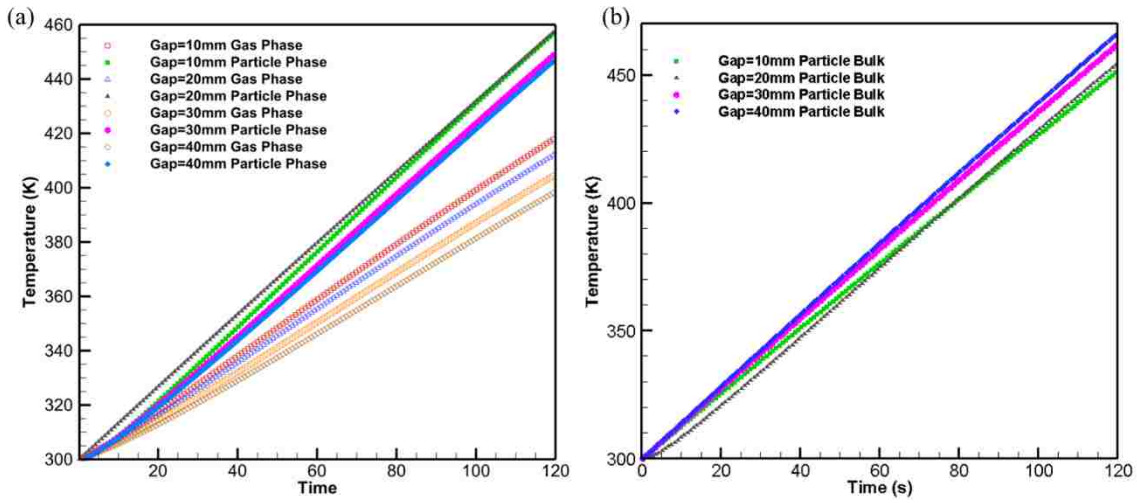

Figure 6. Time-dependent average temperature profiles under various gap sizes: (a) gas phase and particle surface temperature profiles; (b) particle bulk temperature profiles.

The average particle bulk temperature profiles are shown in Figure 6 (b). Different from the temperature profiles of particle surface temperature, the 40 mm gap shows the highest temperature profile and decreases followed with gap size decrease. As particle bulk is solid with the ability to store energy, the radiative energy is the main source of particle bulk temperature increases. Losses only occur during the convection

process. The 40 mm gap has a relatively low average velocity, which corresponds to a low convection energy loss and shows a higher temperature. By taking a comprehensive consideration of convection and radiation, the 30 mm gap is selected for the following study, as it not only has a better ability to obtain higher bulk temperature but also preserves the reasonable length of partition for gas convection and flow path in the catalyst domain.

4.2. INLET AND OUTLET POSITION

Inlet and outlet position is another factor that may affect the flow pattern in the reactor. In this study, top in/out and bottom in/out are discussed to explore the velocity distributions and temperature profiles. The top in/out geometric structure is shown in Figure 1. The configuration of the bottom in/out combines four inlets to only one and moves it to the reactor bottom center. In Figure 7, the contours show velocity and temperature profiles at 120 s. From the velocity contours (Figure 7 (a)), bottom in/out has a higher central velocity. However, the radial velocity distribution is confined, and the graph shows that the flow near the partition interface is almost stagnant. This situation does not appear on the top in/out case since the momentum from evenly distributed top inlets is neutralized and makes a relatively uniform velocity profile in the cavity. As the velocity of the bottom in/out does not fully develop on the partition wall, the velocity distribution also affects the boundary heat convection. The partition boundary interfaces have higher temperatures in the bottom in/out case, which also leads the particles near the partition having higher surface temperatures. The average temperature profiles over 120 s are shown in Figure 8 (a). Even though the boundary temperatures have little difference,

the average temperatures of the gas phase, particle surface, and particle bulk in the catalyst domain are almost the same under the top in/out and bottom in/out cases because the little boundary differences can be neutralized in the catalyst region based on the same operating conditions.

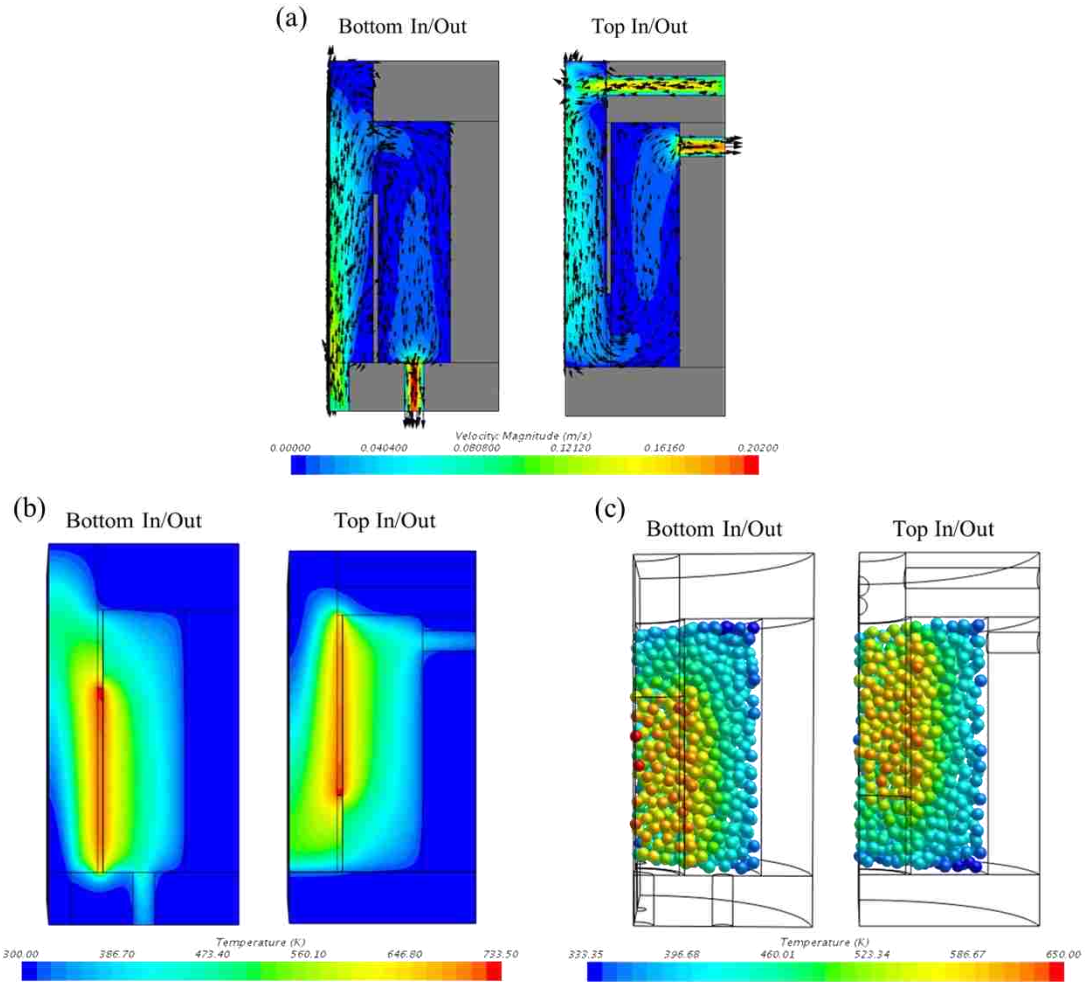

Figure 7. Contours of top in/out and bottom in/out: (a) velocity; (b) gas phase temperature; (c) particle surface temperature.

To investigate the detailed temperature differences between top in/out and bottom in/out, three line probes are placed in the domains, which are cavity centerline, catalyst

center, and catalyst middle. The former two probes focus on the axial temperature distributions shown in Figure 8 (c). From the cavity bottom to the top (0 to 0.125 m), top in/out shows a higher peak value of both probes, which is due to the stronger influences from the radiative properties of insulation. The radial temperature distributions (Figure 8 (d)) show little difference between top in/out and bottom in/out probes, especially in the catalyst domain, as the working properties of catalyst middle probes in the cases are almost the same. Based on the holistic analysis, the inlets/outlets position has little influence on the temperature distributions. Top in/out was selected for the following study after considering its boundary advantages.

4.3. CATALYST THICKNESS

4.3.1. Uniform Radiant Flux. In uniform radiant flux cases, 1 kW radiant power was assumed uniformly distributed on the cavity side interfaces. Since the volume of the reactor chamber is fixed, there is a trade-off between the cavity and catalyst region. Three catalyst thicknesses (20 mm, 30mm, 40 mm) are studied. The velocity contours are shown in Figure 9. As the 20 mm catalyst has the largest cavity space, the fluid from the inlets has a longer path to hit and mix, which causes a dead zone around the connection between the insulation and partition. The larger cavity space makes gas velocity reach a relatively uniform value to enter the catalyst region. With the increase of catalyst thickness, the dead zone near the inlet region disappears and higher cavity velocities arise. An unexpected vortex appears in the 40 mm catalyst near the catalyst/cavity interface due to the uneven incoming velocity.

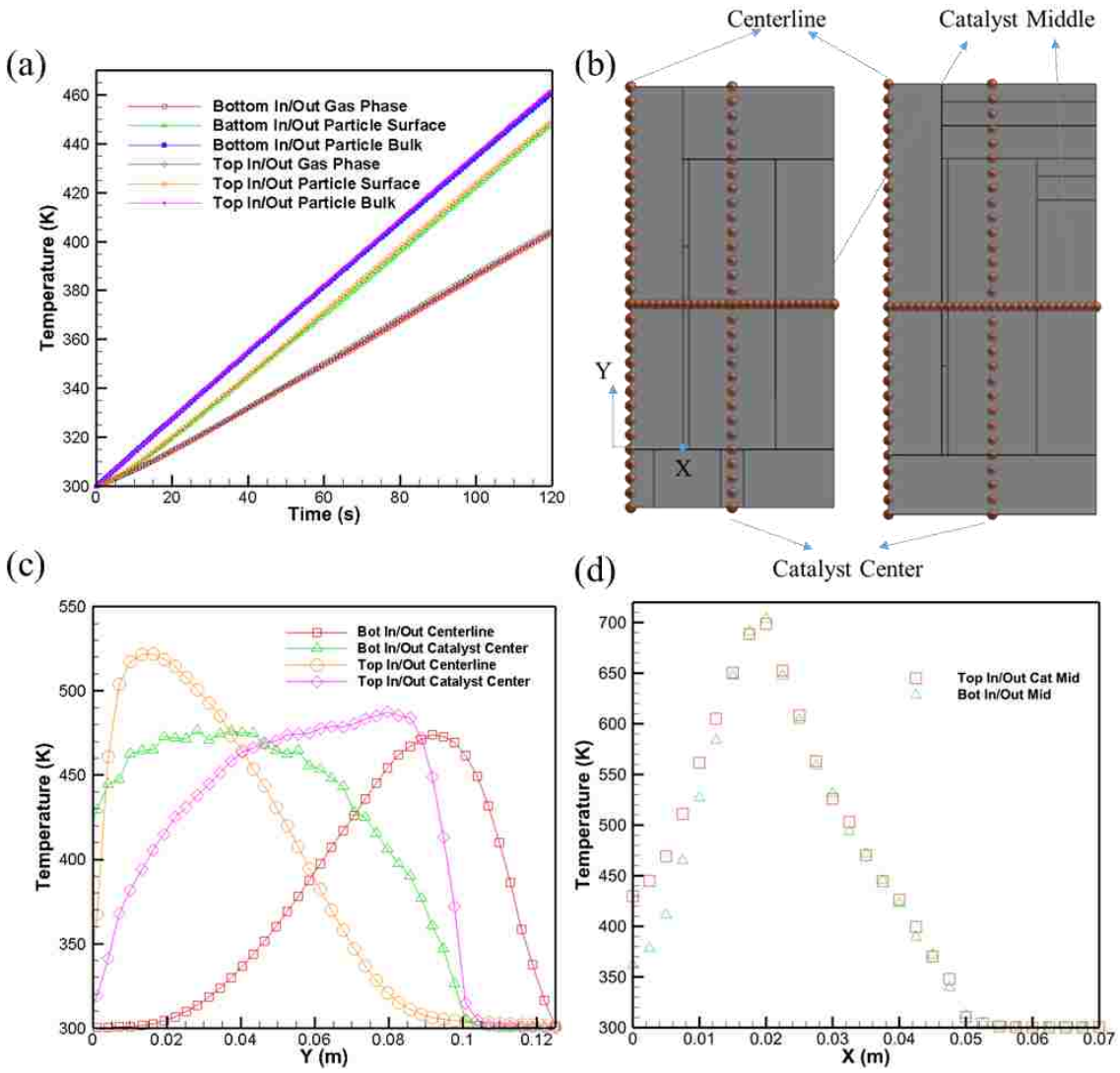

Figure 8. Temperature profiles of different inlets/outlets position: (a) time-dependent average temperatures; (b) Sketches of line probes; (c) axial direction (Y) temperature distributions; (d) radial direction (X) temperature distributions.

The variation of catalyst thickness not only influences the fluid flow but also influences the radiation distribution. The incident radiation distributions of the three cases are shown in Figure 10 (a). The catalyst region with 40 mm thickness has the smallest inner surface, which means the radiant flux on the incoming boundary is the highest under the same power. Based on the CFD algorithm, the incident radiation includes the

receiving radiation for each cell, so the influence of re-radiation is also considered in the contours. Since the 20 mm catalyst has the shortest radial radiative transfer path, the re-radiation is the strongest. The catalyst volume-averaged incident radiations are 281 kW/m^2, 245 kW/m^2, and 246 kW/m^2 for the 20 mm, 30 mm, and 40 mm catalysts, which reflects on the contours as a higher and more uniform incident radiation distribution for the 20 mm catalyst.

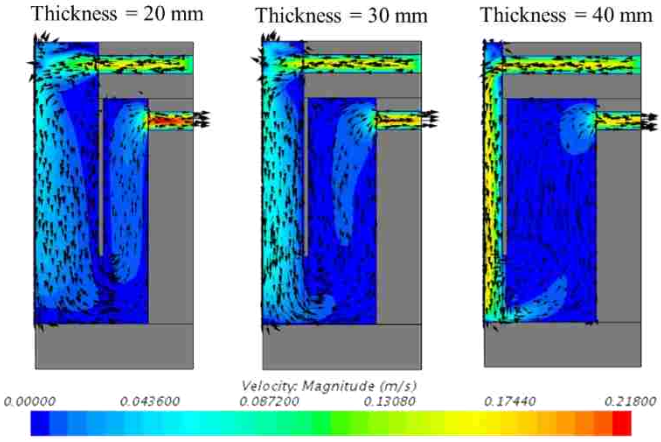

Figure 9. Velocity contours at 120 s for different catalyst thicknesses under uniform radiant flux.

Figure 10 (b) shows the temperature contours at 120 s considering the conjugated heat transfer. The higher temperature on the partition shown in the 30 mm catalyst is caused by the higher incident radiation on the boundary. The temperature is higher on the partition boundary in both 20 mm and 30 catalysts, but this is not consistent in the 40 mm catalyst. This can be explained as the opposite influences of convection and radiation. When convection dominates the heat transfer due to high cavity velocity, the partition accumulated energy is transferred to the cold fluid, which shows a lower temperature

profile near the partition. Thus, the entire temperature distribution appears lower than in the other two cases.

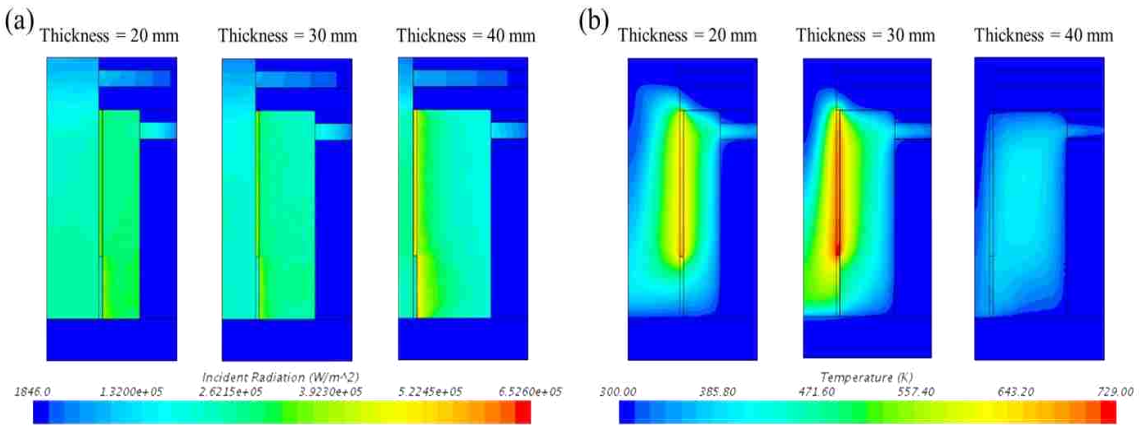

Figure 10. Variable contours at 120s of various catalyst thicknesses under uniform radiant flux: (a) incident radiation; (b) temperature.

Time-dependent average temperatures of the catalyst region are presented in Figure 11. The gas phase and particle surface temperatures (Figure 11 (a)) of the 20 mm and 30 mm catalyst regions are nearly equivalent, with the temperature for the 20 mm catalyst section being a little higher than the 30 mm region. However, the 40 mm catalyst section shows more variation for both gas phase and particle surface due to surface convection effects. The particle bulk temperatures are shown in Figure 11 (b). The temperature profiles are nearly consistent with the results of average incident radiation flux for each case. Under uniform radiant flux, the 20 mm catalyst section shows a better temperature distribution.

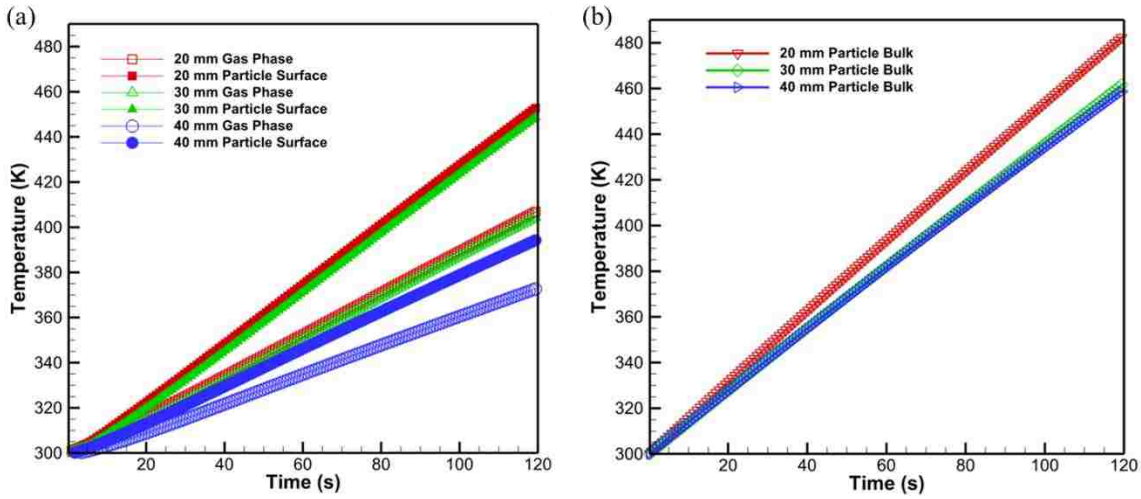

Figure 11. Time-dependent temperature profiles of different catalyst thicknesses under uniform radiant flux: (a) gas and particle surface phases; (b) particle bulk.

4.3.2. Concentrated Radiant Flux. The concentrated ray distributions of different catalyst thicknesses and corresponding boundary radiant fluxes are shown in Figure 12. The various catalyst thicknesses cause different distances between the focal plane and primary side ray distribution region shown in Figure 12 (a). With increasing catalyst thickness, the ratio between focal diameter and receptive cylinder diameter becomes larger and larger, which directs more rays to hit on the side region near the focal plane instead of being uniformly distributed on the entire side surface. The influence on the radiant flux is that catalyst thickness of 20 mm has a larger radiant absorption side area but lower flux. The radiant fluxes of 30 mm and 40 mm thickness increase by sacrificing the main absorption area.

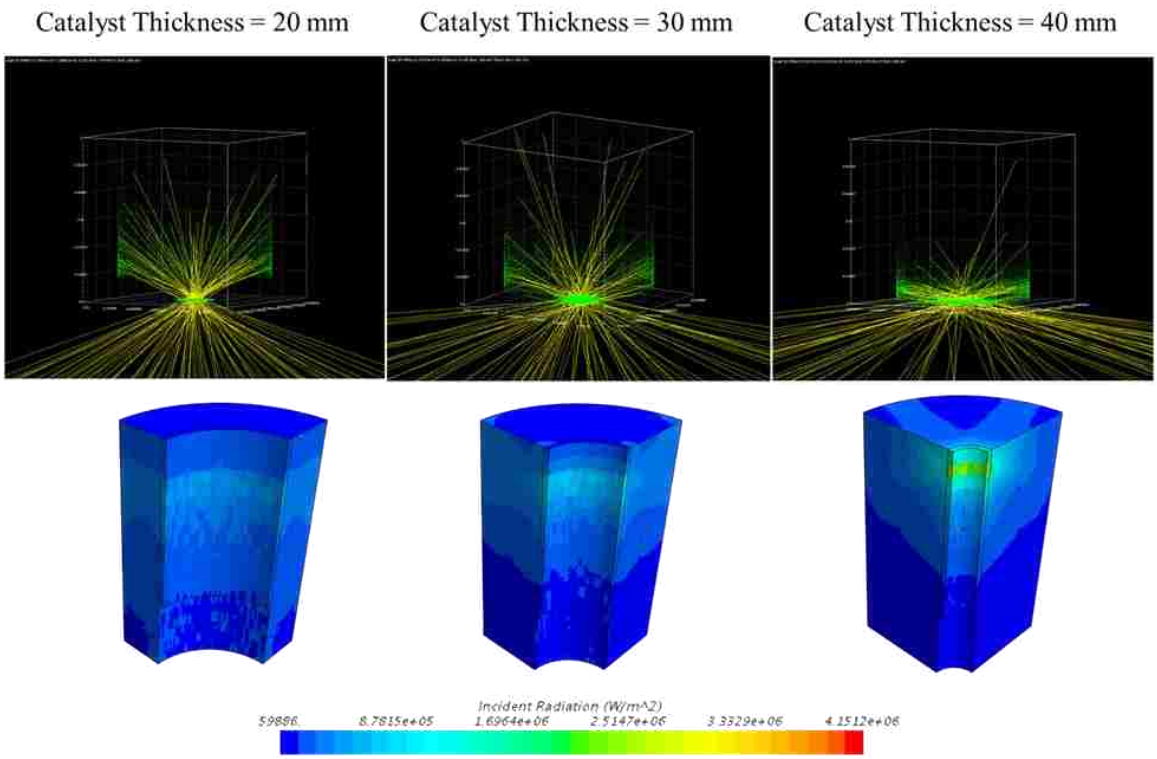

Figure 12. Concentrated radiant fluxes under different catalyst thickness: (a) ray distributions; (b) radiant fluxes.

A detailed study on the relation between radiant flux and position is presented in Figure 13. Two axial line probes on the catalyst inner surface and catalyst center are selected to describe the tendency of radiant absorption and transformation in the catalyst region (shown in Figure 13 (a)). In the *Y* direction, 0.1 m represents the focal plane, and 0 m represents the bottom of the catalyst. The incident radiation on the inner surface of the 40 mm catalyst has a much higher value than all other cases, which is as high as 1.75 MW/m^2 when 0.01 m away from the focal point. The peak radiant flux on the catalyst inner surface of the other two cases embodies a sharp decrease with a bottom shift of the position. The radiant fluxes of the catalyst center along the axial direction keep a relatively low level, around 0.2 to 0.4 MW/m^2, as the radiant flux of the catalyst center is

determined primarily by re-radiation instead of direct radiation. Thus, the center radiant flux variations along the axial direction are more inconspicuous than those of the catalyst inner surface. The radiant flux variation at the catalyst middle (0.05 m) along the radial direction is shown in Figure 13 (b), where 0 m represents the center of the reactor. The catalyst thickness of 20 mm shows a higher and more stable radiant flux in the catalyst region due to the contour shown in Figure 13 (b). The radiant flux rising near the catalyst outer surface is caused by the reflection of the insulation surface. With the catalyst thickness increasing, direct radiation is absorbed during radial transfer, which leads to a gradual decrease of the flux.

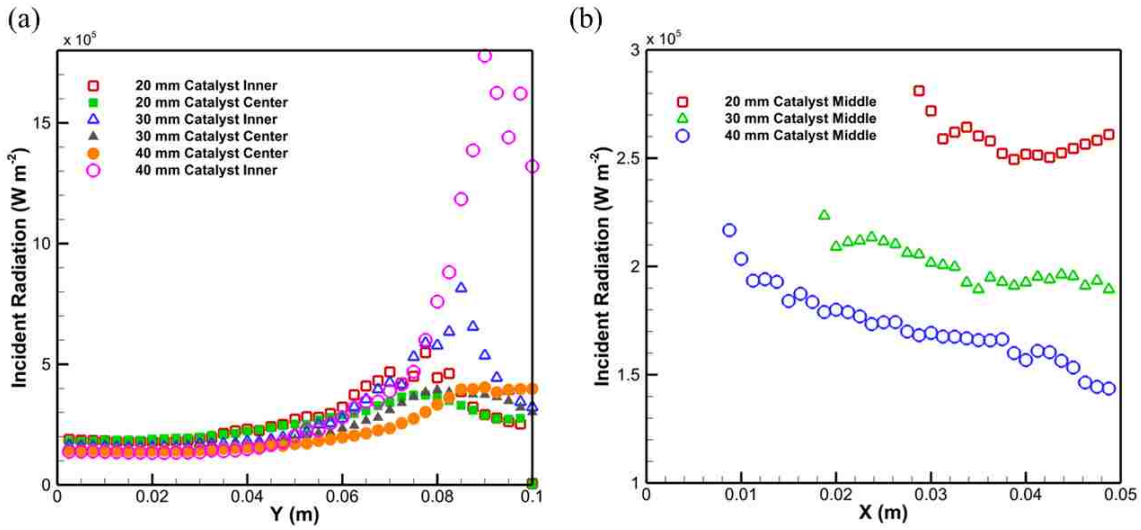

Figure 13. Radiant flux distributions under different catalyst thicknesses: (a) axial direction; (b) radial direction.

The temperature profiles of various catalyst thickness under concentrated radiant flux are shown in Figure 14. As discussed in the constant radiant flux case, the fluid flow strongly affects the temperature distribution of 40 mm catalyst thickness, which is also

shown under the concentrated radiant flux. The temperature contours of 20 mm and 30 mm catalyst thickness for gas phase and particle surface present the same tendency of radiant flux. Since the radiant flux is concentrated on the inner surface of the partition near the top region, the temperatures are correspondingly higher. Figure 14 (a) and (b) clearly present the temperature hot spots on the partition and particles near high flux region. Even though the 30 mm catalyst shows higher temperature in some regions, the time-dependent average temperatures of the gas phase and particle surface are extremely close (shown in Figure 14 (d) and (e)).

As the 20 mm catalyst has a thinner region with fewer particles, a better flow pattern and radiative transfer are derived which is beneficial for a relatively homogeneous temperature profile. Because of the uneven radiative distribution and thicker catalyst layer of 30 mm catalyst, the temperatures of the gas phase and particle surface present slightly lower than those of 20 mm catalyst. Because a larger number of particles are in the 30 mm catalyst region, the particle bulk temperature is lower, since particle bulk temperature is dominated by the radiative flux. Generally, the temperature differences between the 20 mm and 30 mm catalyst are not apparent enough. Both cases are considered in the two-step CO_2 splitting process.

4.4. TWO-STEP CO_2 SPLITTING

The CeO_2 reduction process is assumed to be initiated at 1273 K for 5 mins running time under the concentrated radiant flux described above. The oxygen evolution rate is shown in Figure 15. The 30 mm catalyst derives a higher reaction rate, around 0.45 mL/min/gCeO_2. As the reaction rate is a function of temperature, oxygen partial pressure,

and particle mass based on Eq. (24) and (25), the time-dependent temperature distributions and oxygen partial pressures at 5 mins are presented in Figure 16.

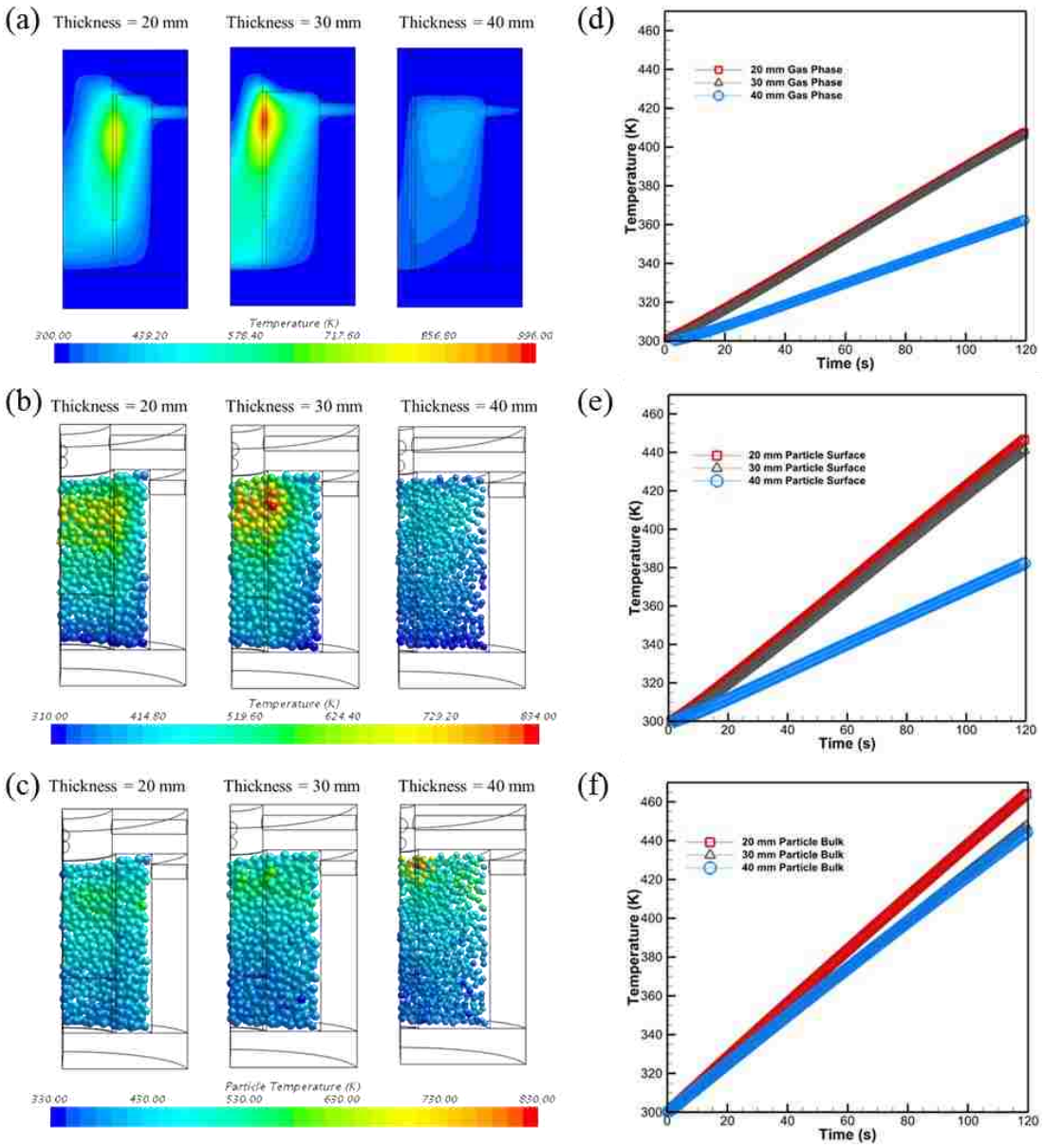

Figure 14. Temperature profiles of various catalyst thicknesses under concentrated radiant flux: (a) gas phase contour; (b) particle surface contour; (c) particle bulk contour; (d) gas phase time-dependent temperature; (e) particle surface time-dependent temperature; (f) particle bulk time-dependent temperature.

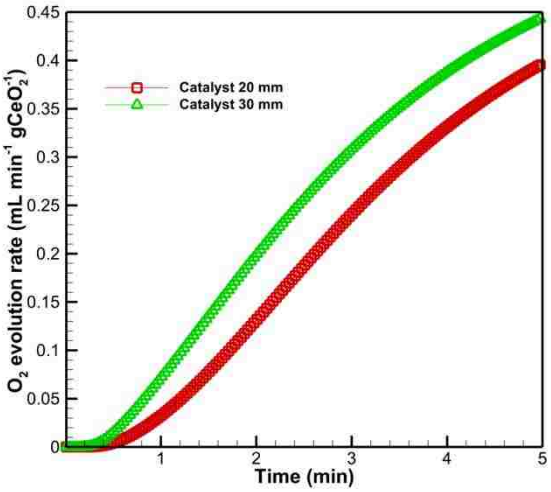

Figure 15. Oxygen evolution rates in the CeO_2 reduction process.

The temperature profiles in Figure 16 (a) show that the 20 mm catalyst can achieve higher temperatures for gas phase, particle surface, and particle bulk, which is consistent with the results for only heat transfer. However, considering the influence of O_2 partial pressure, the 30 mm catalyst presents a higher oxygen capacity. The overall oxygen generating amount in 5 mins for the two cases is 0.929 mL/gCeO_2 and 1.184 mL/gCeO_2 for the 20 mm and 30 mm catalysts, respectively. Considering the mass of the CeO_2 catalyst, the reactor with the 20 mm catalyst and 30 mm catalyst can produce 1179.8 mL and 1973.6 mL oxygen in 5 mins, respectively. From the reaction formula, the reaction rate between CO and O_2 can be summarized as $r_{CO} = 2r_{O_2}$, which can be used to predict the production of CO. The HHV of carbon monoxide is 12.64 MJ/m^3 (Khartchenko and Kharchenko, 2013). The theoretical solar-to-fuel efficiency of the two cases is 9.5% and 15.9% without considering the heat recovery. The results show that the 30 mm catalyst partition-cavity reactor has an advantage for CO_2 splitting.

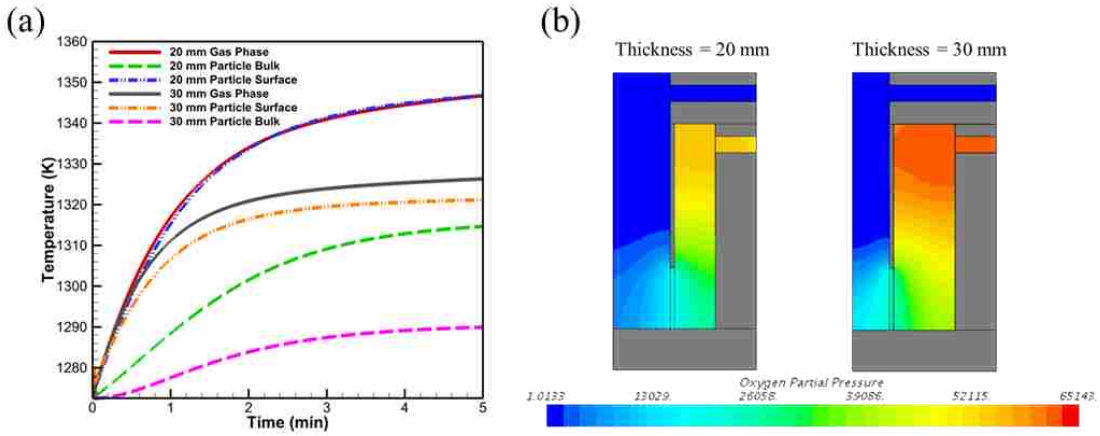

Figure 16. Factors that influence O_2 evolution rate: (a) temperature; (b) O_2 partial pressure.

5. CONCLUSIONS

The geometric factors of a partition-cavity solar thermochemical reactor are studied via three-dimensional transient CFD models. MCRT is combined with the DOM method to study heat transfer under concentrated solar radiation. The gap between the partition and insulation bottom affects the flow pattern and heat transfer among fluid, solids and particles. Inlet/outlet position has little influence on average heat transfer performance. Considering the preferences of boundary values, the top in/out is more favorable. For the partition-cavity reactor, a narrow cavity causes rapid cold fluid flow velocity and affects the heat transfer, which leads to an adverse temperature distribution. The radiant fluxes are divergent under different catalyst thicknesses. However, the temperature profiles are similar, with only a little advantage using the thinner catalyst. The oxygen evolution rate in the two-step CO_2 splitting process shows that the 30 mm

catalyst reactor has higher productivity with higher solar-to-fuel efficiency. The partition-cavity reactor is promising to increase the efficiency of the solar thermochemical process.

ACKNOWLEDGEMENT

We gratefully acknowledge the financial support from the Wayne and Gayle Laufer Foundation.

REFERENCES

Andre, S., Degiovanni, A., 1995. A theoretical study of the transient coupled conduction and radiation heat transfer in glass: phonic diffusivity measurements by the flash technique. International Journal of Heat and Mass Transfer 38(18), 3401-3412.

Anikeev, V.I., Kirillov, V.A., 1991. Basic design principles and some methods of investigation of catalytic reactors-receivers of solar radiation. Solar energy materials 24(1-4), 633-646.

Bader, R., Chandran, R.B., Venstrom, L.J., Sedler, S.J., Krenzke, P.T., De Smith, R.M., Banerjee, A., Chase, T.R., Davidson, J.H., Lipiński, W., 2015. Design of a solar reactor to split CO2 via isothermal redox cycling of ceria. Journal of Solar Energy Engineering 137(3), 031007.

Balomenos, E., Gianopoulou, I., Panias, D., Paspaliaris, I., 2009. ENEXAL: Novel technologies for enhanced energy and exergy efficiencies in primary aluminium production industry. Metalurgija 15(4), 203-217.

Baykara, S., 2004. Hydrogen production by direct solar thermal decomposition of water, possibilities for improvement of process efficiency. International Journal of Hydrogen Energy 29(14), 1451-1458.

Brewster, M.Q., 1992. Thermal radiative transfer and properties. John Wiley & Sons.

Bulfin, B., Lowe, A., Keogh, K., Murphy, B., Lubben, O., Krasnikov, S., Shvets, I., 2013. Analytical model of CeO2 oxidation and reduction. The Journal of Physical Chemistry C 117(46), 24129-24137.

Chambon, M., Abanades, S., Flamant, G., 2011. Thermal dissociation of compressed ZnO and SnO2 powders in a moving‐front solar thermochemical reactor. AIChE Journal 57(8), 2264-2273.

Chueh, W.C., McDaniel, A.H., Grass, M.E., Hao, Y., Jabeen, N., Liu, Z., Haile, S.M., McCarty, K.F., Bluhm, H., El Gabaly, F., 2012. Highly enhanced concentration and stability of reactive Ce3+ on doped CeO2 surface revealed in operando. Chemistry of Materials 24(10), 1876-1882.

Craig, K., Moghimi, M., Rungasamy, A., Marsberg, J., Meyer, J.P., 2016. Finite-volume ray tracing using Computational Fluid Dynamics in linear focus CSP applications. Applied energy 183, 241-256.

Crane, 1977. Flow of fluids: through valves, fittings, and pipe.

Cundall, P.A., Strack, O.D., 1979. A discrete numerical model for granular assemblies. geotechnique 29(1), 47-65.

Energysage, 2018. How is solar energy used? The 5 most common examples of solar power. https://news.energysage.com/most-common-solar-energy-uses/.

Furler, P., Scheffe, J., Gorbar, M., Moes, L., Vogt, U., Steinfeld, A., 2012. Solar thermochemical CO2 splitting utilizing a reticulated porous ceria redox system. Energy & Fuels 26(11), 7051-7059.

Furler, P., Steinfeld, A., 2015. Heat transfer and fluid flow analysis of a 4 kW solar thermochemical reactor for ceria redox cycling. Chemical engineering science 137, 373-383.

Gokon, N., Nakamura, S., Hatamachi, T., Kodama, T., 2014. Steam reforming of methane using double-walled reformer tubes containing high-temperature thermal storage Na2CO3/MgO composites for solar fuel production. Energy 68, 773-782.

Hanley, H.J., Ely, J.F., 1973. The viscosity and thermal conductivity coefficients of dilute nitrogen and oxygen. Journal of Physical and Chemical Reference Data 2(4), 735-756.

Hanley, H.J., McCarty, R.D., Sengers, J., 1974. Viscosity and thermal conductivity coefficients of gaseous and liquid oxygen.

Haynes, W.M., 2014. CRC handbook of chemistry and physics. CRC press.

Ishida, T., Gokon, N., Hatamachi, T., Kodama, T., 2014. Kinetics of thermal reduction step of thermochemical two-step water splitting using CeO2 particles: Master-plot method for analyzing non-isothermal experiments. Energy Procedia 49, 1970-1979.

Kaneko, H., Miura, T., Fuse, A., Ishihara, H., Taku, S., Fukuzumi, H., Naganuma, Y., Tamaura, Y., 2007. Rotary-type solar reactor for solar hydrogen production with two-step water splitting process. Energy & Fuels 21(4), 2287-2293.

Khartchenko, N.V., Kharchenko, V.M., 2013. Advanced energy systems. CRC Press.

Lapp, J., Davidson, J.H., LipiĹ, W., 2013. Heat transfer analysis of a solid-solid heat recuperation system for solar-driven nonstoichiometric redox cycles. Journal of Solar Energy Engineering 135(3), 031004.

Lathrop, K.D., Carlson, B.G., 1964. Discrete ordinates angular quadrature of the neutron transport equation. Los Alamos Scientific Lab., N. Mex.

Lichty, P., Liang, X., Muhich, C., Evanko, B., Bingham, C., Weimer, A.W., 2012. Atomic layer deposited thin film metal oxides for fuel production in a solar cavity reactor. international journal of hydrogen energy 37(22), 16888-16894.

Marxer, D., Furler, P., Takacs, M., Steinfeld, A., 2017. Solar thermochemical splitting of CO 2 into separate streams of CO and O 2 with high selectivity, stability, conversion, and efficiency. Energy & Environmental Science 10(5), 1142-1149.

McBride, B.J., Gordon, S., Reno, M.A., 1993. Coefficients for calculating thermodynamic and transport properties of individual species.

Meier, A., Gremaud, N., Steinfeld, A., 2005. Economic evaluation of the industrial solar production of lime. Energy conversion and management 46(6), 905-926.

Michalsky, R., Parman, B.J., Amanor-Boadu, V., Pfromm, P.H., 2012. Solar thermochemical production of ammonia from water, air and sunlight: thermodynamic and economic analyses. Energy 42(1), 251-260.

Miller, J.E., Allendorf, M.D., Ambrosini, A., Chen, K.S., Coker, E.N., Dedrick, D.E., Diver, R.B., Hogan, R.E., Ermanoski, I., Johnson, T.A., 2012. Final Report—Reimagining Liquid Transportation Fuels: Sunshine to Petrol. Sandia National Laboratories, Albuquerque, NM, Report No. SAND2012-0307.

Möller, S., Kaucic, D., Sattler, C., 2006. Hydrogen production by solar reforming of natural gas: a comparison study of two possible process configurations. Journal of Solar Energy Engineering 128(1), 16-23.

Muir, J.F., Hogan Jr, R.E., Skocypec, R., Buck, R., 1993. The CAESAR project: Experimental and modeling investigations of methane reforming in a Catalytically Enhanced Solar Absorption Receiver on a parabolic dish. Sandia National Labs., Albuquerque, NM (United States); Deutsche Forschungsanstalt fuer Luft-und Raumfahrt eV (DLR), Stuttgart (Germany). Inst. fuer Technische Thermodynamik.

Nicolau, V., Borges, M., Silva, L., 2002. Radiative properties of glass and coatings, The 3rd European Conference on Energy Performance & Indoor Climate in Building. pp. 835-840.

Panlener, R., Blumenthal, R., Garnier, J., 1975. A thermodynamic study of nonstoichiometric cerium dioxide. Journal of Physics and Chemistry of Solids 36(11), 1213-1222.

Petrasch, J., Steinfeld, A., 2007. Dynamics of a solar thermochemical reactor for steam-reforming of methane. Chemical engineering science 62(16), 4214-4228.

Piatkowski, N., Wieckert, C., Weimer, A.W., Steinfeld, A., 2011. Solar-driven gasification of carbonaceous feedstock—a review. Energy & Environmental Science 4(1), 73-82.

Richet, P., Bottinga, Y., Denielou, L., Petitet, J., Tequi, C., 1982. Thermodynamic properties of quartz, cristobalite and amorphous SiO2: drop calorimetry measurements between 1000 and 1800 K and a review from 0 to 2000 K. Geochimica et Cosmochimica Acta 46(12), 2639-2658.

Scheffe, J.R., Steinfeld, A., 2014. Oxygen exchange materials for solar thermochemical splitting of H2O and CO2: a review. Materials Today 17(7), 341-348.

Schunk, L.O., Haeberling, P., Wepf, S., Wuillemin, D., Meier, A., Steinfeld, A., 2008. A receiver-reactor for the solar thermal dissociation of zinc oxide. Journal of Solar Energy Engineering 130(2), 021009.

SEIA, 2018. Solar Industry Data. https://www.seia.org/solar-industry-data.

Shuai, Y., Xia, X.-L., Tan, H.-P., 2008. Radiation performance of dish solar concentrator/cavity receiver systems. Solar Energy 82(1), 13-21.

STAR-CCM+, 2017. Material Databases. Siemens AG.

Steinfeld, A., Kuhn, P., Karni, J., 1993. High-temperature solar thermochemistry: production of iron and synthesis gas by Fe3O4-reduction with methane. Energy 18(3), 239-249.

Tait, P.G., 1899. Newton's Laws of Motion. A. & C. Black.

Touloukian, Y.S., 1966. Thermophysical Properties of High Temperature Solid Materials. Volume 4. Oxides and Their Solutions and Mixtures. Part 1. Simple Oxygen Compounds and Their Mixtures. THERMOPHYSICAL AND ELECTRONIC PROPERTIES INFORMATION ANALYSIS CENTER LAFAYETTE IN.

Vidal, A., Denk, T., Steinfeld, L., Zacarías, L., Almería, T., 2010. Upscaling of a 500 kW solar gasification plant, Proceedings of 18th world hydrogen energy conference. pp. 177-181.

Wieckert, C., Epstein, M., Olalde, G., Santén, S., Steinfeld, A., 2009. Zinc electrodes: solar thermal production, Encyclopedia of Electrochemical Power Sources. Elsevier, pp. 469-486.

Wieckert, C., Obrist, A., Zedtwitz, P.v., Maag, G., Steinfeld, A., 2013. Syngas production by thermochemical gasification of carbonaceous waste materials in a 150 kWth packed-bed solar reactor. Energy & Fuels 27(8), 4770-4776.

Yadav, D., Banerjee, R., 2016. A review of solar thermochemical processes. Renewable and Sustainable Energy Reviews 54, 497-532.

Yaws, C.L., 2008. Thermophysical properties of chemicals and hydrocarbons. William Andrew.

Yu, T., Yuan, Q., Lu, J., Ding, J., Lu, Y., 2017. Thermochemical storage performances of methane reforming with carbon dioxide in tubular and semi-cavity reactors heated by a solar dish system. Applied Energy 185, 1994-2004.

Zimmermann, D., 2012. Flow Modeling of a Solar Thermogravimeter. Master Thesis ETH Zurich.

Zinkevich, M., Djurovic, D., Aldinger, F., 2006. Thermodynamic modelling of the cerium–oxygen system. Solid State Ionics 177(11-12), 989-1001.

III. SIMULATION OF STRUCTURAL EFFECTS OF MONOLITH CATALYST ON DRY REFORMING OF METHANE IN A SOLAR THERMOCHEMICAL REACTOR

Han Zhang and Joseph D. Smith

Department of Chemical and Biochemical Engineering, Missouri University of Science and Technology, Rolla, MO 65401, USA

ABSTRACT

Methane dry reforming (MDR) is a promising progress, as it not only solves the issue of greenhouse gas (CH_4, CO_2) emissions but also provides appropriate energy storage products (CO, H_2) for individual applications or further Fischer-Tropsch synthesis. The introduction of solar energy into the MDR process is an attractive approach to store solar energy to chemical fuels with eliminating the limitations in time and space. Since MDR is an endothermic process, concentrated solar energy can provide essential heat to maintain the process operation. Since MDR obeys surface chemistry, the catalyst structures affect the thermal and reactive performances. In this paper, computational fluid dynamic (CFD) numerical analysis is applied to study the effects of the lattice structure for the monolith catalyst in a three-dimensional (3D) annular fixed bed sample. Solar radiation is introduced as an energy source boundary condition with considering internal radiation via discrete ordinate method (DOM). Nickel-based catalyst is applied to simulate the MDR process. The structures of catalysts are further built in the catalyst region of the former reported solar partition cavity reactor to investigate the heat, mass transfer performance with energy conversion efficiency in a specific reactor.

Keywords: *Dry reforming of methane, Solar thermochemical reactor, Periodic open cellular structures, Heat and mass transfer, Computational fluid dynamics*

1. INTRODUCTION

The rapid growth of the economy in the world directly leads to an explosive demand for energy. It is predicted that a 48% increase in energy consumption will occur from 2012 to 2040 [1]. With this energy consumption increase, the relevant environmental problems follow, especially greenhouse gases (GHG) emission [2]. Carbon dioxide (CO_2) and methane (CH_4) are the two major sources of GHG [3]. Even though CO_2 and CH_4 have negative effects on the environment, they work well as carbon contributors to various processes [4–7]. Additionally, the CH_4 reserve is abundant in shale gas recovery, petroleum reserves, and biogas and landfill gases [8–11]. Due to the consideration of environment and energy, the technologies for conversion of CO_2 and CH_4 to further higher value chemicals are promising. Dry reforming of methane (DRM) provides an anticipated approach to convert CO_2 and CH_4 to syngas, synthesized by carbon monoxide (CO) and hydrogen (H_2). This process can be represented in the reaction below:

$$CH_4 + CO_2 \leftrightarrow 2CO + 2H_2 \qquad \Delta H^{\circ}_{298K} = +247\ \text{kJ/mol} \tag{1}$$

Along with this main reaction of DRM, a reverse water gas shift (RWGS) side reaction occurs simultaneously:

$$CO_2 + H_2 \leftrightarrow CO + H_2O \qquad \Delta H^{\circ}_{298K} = +41 kJ/mol \tag{2}$$

The syngas yield of DRM has a relatively lower H_2/CO ratio, which is desired to work as feedstock in the Fischer-Tropsch (FT) synthesis [12,13]. It is also clearly seen

that both reaction reactions are endothermic. Solar energy has the advantages of providing required energy in the DRM process, since it avoids the traditional energy supplied approach, which used combusted methane as the energy provider [14]. It is reported that the calorific value of incoming methane can be theoretically increased by 22~28% based on solar aided DRM [15]. On the other hand, the DRM also provides an option to store solar energy in the form of chemical fuels [16,17].

The design of solar reactors is one of the most important factors that influence the DRM performance. Due to the introduction of concentrated solar energy, the reactor types can be distinguished as the indirectly-irradiated reactor and the directly-irradiated reactor based on the heat transfer methods in the reactive region (radiation or conduction).

Heat pipes are the most common indirectly-irradiated reactors that are utilized in DRM. Solar radiation is absorbed by the pipes or the heat transfer medium materials among the pipes. The DRM reaction occurs in the pipe and derives the heat from conduction through the pipe. Yu et al. established a semi-cavity reactor with five stainless steel tubes, which tube walls are inscribed with the half circles of the semi-cavity [18]. Concentrated solar fluxes are distributed on the surfaces of the opaque tubes to provide energy for DRM using Ni/Al_2O_3 as the catalyst. The methane conversion is tested as 74.8% under 598.5 Direct normal irradiation (DNI). Some heat transfer medium, like air, sodium vapors, and molten salts, are introduced in the indirectly-irradiated solar reactors, especially the reactors with a group of pipes [19]. One of the representatives is the joint research project of Sandia National Laboratories and Weizmann Institute of Science (SNL-WIS) in the 1990s, which used sodium as the heat transfer medium [20]. Based on

the physical state change of sodium, the concentrated solar energy was converted to heat the reactor tubes. A maximum 70% methane conversion was reported under 7.8 kW power input. A double-walled tubular receiver reactor for the MoSTAR project was proposed by Kodama et al. [21]. Molten salts, like Na_2CO_3 and MgO, were filled in the annular gap between two walls to absorb solar energy and transfer heat via phase change. By adjusting the ratio of salts, the methane conversion maintained 90% under 0.9 kW. Dahl et al. proposed a fluid-wall aerosol flow reactor with the directly solar irradiated design [22]. Without adding catalysts for DRM, the CH_4 conversion can reach 70% under 2000K temperature. A carbon particle seeded directly irradiated solar reactor was designed for DRM by Klein et al. [23]. By drawing on the experience of entrained particles in the working gas flow [24], solar radiation is absorbed and reflected in the reactor to heat up the gas flow. The methane conversion is 90% at 1443K in this solar receiver [23]. Considering the goal to improve DRM performance and efficiency, the directly-irradiated reactor tends to be designed based on the concept of the volumetric reactor with metallic and ceramic absorbers [25]. The noble metal catalysts (Rh, Ru, Ni, etc.) are adopted on the metallic or ceramic foams or honeycombs to form structured catalyst absorbers, which provide the opportunity to absorb solar fluxes and activate reactions simultaneously [26]. Alumina support is one of the most popular absorbers, which has been selected as the supporter for different catalysts and proven to hold a stable activity and remarkable performances [27–30]. Some other porous supporters, such as SiC ceramic foam [31–33], Ni-Cr-Al metallic foam [34,35], Cu foam [33,36], and 316 stainless steel foam [37], also showed great potentials and attractive performances in solar DRM process.

The reaction kinetics of DRM is important to scale up the process for the accessibility of industrial applications. Different kinetic models were proposed and validated during the past few years. As Rh, Ru, and Ni are representative catalysts, numerous studies focused on the simulation of DRM using varies reaction kinetics. Fuqiang et al. [38] numerically studied the DRM performances over Ru/γ-Al_2O_3/metallic foams used Langmuir-Hinshelwood (LH) model in a solar thermochemical reactor. By comparing the influences of inlet velocity, heat flux distribution, and the composition of feedstock, the maximum energy storage efficiency can be derived when the CH_4/CO_2 ratio is 0.67. Gokon et al. [15] examined four representative DRM kinetic models (Basic, Eley–Rideal, Stepwise, and LH) against the reactions in a solar reformer under 600-750 °C. The results showed that the LH model best predicted the reforming rates and the corresponding parameters in the model were also derived. The reaction kinetics from Richardson and Paripatyadar [39] and the detailed elementary mechanism from McGuire et al. [40] were used in the DRM over Rh catalyst in different types of reactors (membrane reactor, fluidized-bed reactor, and packed-bed reactor) [41–43]. Ni-based catalyst becomes attractive in the DRM process, since it has a lower cost and relatively easy to achieve. Presently, three representative models are applied to Ni-based DRM reactions, which are power-law (PL) model, Eley Rideal (ER) model, and the Langmuir Hinshelwood–Hougen Watson (LHHW) model. PL model is the basic kinetic rate for DRM, which can be expressed as

$$r = k\left[P_{CH_4}\right]^m\left[P_{CO_2}\right]^n \tag{3}$$

where k is the reaction rate constant, P_{CH_4} and P_{CO_2} are the partial pressures of CH_4 and CO_2, m and n are the reaction rate coefficients. As the PL model is a simplified model, it

has the advantage to reduce the complexity of parameters and roughly estimate the DRM rate, more rigorous models should be used when the operation conditions change in a wider range [44]. Due to the convenience, the PL model were used in some packed bed reactor and solar-aided volumetric reactors [18,45,46]. The ER model is an improved mechanism for DRM with the basic rate expression as follow [47]:

$$r = k(P_{CH_4}P_{CO_2} - \frac{{P_{CO}}^2 {P_{H_2}}^2}{K}) \quad (4)$$

where P_{CO} and P_{H_2} are the partial pressure of CO and H_2, and K is the thermal equilibrium constant. Eq. (4) is based on the main reaction formula (shown in Eq. (1)). By assigning different rate-determining step (RDS) in the reaction mechanism, various expressions were derived and validated experimentally [48,49]. The LHHW model is the most common formalism to describe the reaction rate of the DRM, which generally includes the entire process from the reactants dissociative adsorption to the rate-determining surface reactions for products. In this model, only one step is assumed as the slow and rate-determining reaction followed by the other steps as thermodynamic equilibrium [47]. The possible elementary reactions were Zhu et al.[50] . Based on the various selection of RDS, a plentiful number of reaction rate expressions were proposed for different Ni-based catalysts and reaction conditions numerically and experimentally, which were summarized and deeply discussed in the review study of Kathiraser et al. [44].

Fixed-bed reactors, which are formed by filling the catalytic particles, are one of the most common reactors to realize the methane reforming process, especially for large-scale reforming [51]. Wehinger et al. focused on the studies of investigating the DRM

process with particle-resolved CFD model in fixed-bed reactors [43,52–56]. They used the discrete element method (DEM) to realize the particle parking in the fixed-bed reactors. By studying the influences of packing particle shapes, contact methods of particles, pore processes, and the microkinetics of the reactions, they gradually improve the particle-resolved model for the simulation of DRM. Beside the packed-bed reactors, the monolith reactors are attractive and widely applied in the different fields, especially the environmental applications, as monoliths have better heat and mass transfer performances due to larger void fractions and higher catalyst effectiveness factors [57]. Hettel et al. [58] proposed the numerical study of a honeycomb-structured Rh/Al_2O_3 monolith catalyst for the catalytic partial oxidation of methane process using the combination of OpenFOAM and DETCHEM. They discussed the heat and mass transfer performances in a single quadratic shape channel under 2D and 3D cases and revealed that their differences are tiny. The model was further extended to simulate an entire monolith catalyst. The numerical solution of temperature has a good agreement with the experimental data, however, the conversion of methane was underestimated due to the influences of boundary conditions. Inbamrung et al. [59] studied on the size optimization of a square-channel monolith reactor for the steam methane reforming using 3D model and the corresponding results were tested in the experiments. The results showed that a small channel height is more beneficial to the reactions, however, the complex chemistry analytic model needed to be revised to get better accuracy. Cui et al. [60] set up a 2D model to study the influences of geometric parameters on the thermal performances of the SMR reformer and proved the model has acceptable errors under the conditions without reactions. With the development of additive manufacturing (AM), the periodic

open cellular structures (POCS) are introduced in the catalytic reactors, as this kind of monolith provides a large specific surface area with a low pressure drop, a good heat transfer performance, and a high unit chemical activity [61–63]. Bianchi et al. [64] numerical studied the influences of strut morphology on the heat conduction in the catalytic reactor. They proved a small cross-section of the strut caused an increase of the thermal resistance and a constant cross-section led to a higher heat transfer performance, which is better than the conventional open-cell foams. Lucci et al. [65] compared the momentum and mass transfer performances of the equivalent real foam and the Kelvin cell lattice via CFD. The results indicated that the Kelvin cell lattice showed a lower pressure drop, a higher mass transfer coefficient, and a better trade-off, when the porosity is lower than 80%. Busse et al. [66] proposed the heat transfer correlation for the POCS and experimentally validated the correlation in a heat exchanger. The results showed the POCS has advantages on the heat transfer performances than packed-bed reactors, especially in a low flow rate. Papetti et al. [67] focused on numerically and experimentally analyzing the geometrical characteristics of the open cell polyhedral lattices in the application of automotive catalysts. It is shown that the lattice structure was more than twice higher mass transfer than that of honeycomb. Kramer et al. [68] experimentally tested the thermal performances of the monolith catalyst produced by AM and found a 34% increase of the effective thermal conductivity of the studied substrate model. The POCS has advantages on the heat and mass transfer in the catalytic reactor, however, few published works focused on the numerical study of DRM using the POCS.

In this paper, the finite volume method was used to investigate the heat and mass transfer performances of the POCS catalyst in a self-designed partition-cavity solar

thermochemical reactor. The effects of the POCS struct shapes and sizes were analyzed under a 3D heat transfer model with uniform radiative distribution on the boundary for a slice of the catalyst region. The operating conditions of the DRM, including the inlet gas flow rate, the feedstock composition, and the input radiative power, were further investigated based on their influences on the temperature distribution and the methane conversion.

2. DESCRIPTION OF POCS AND THE SOLAR THERMOCHEMICAL REACTOR

For the purpose to investigate the influences of the parameters of the POCS, three different struts were introduced based on the ideal cubic cell geometric unit. The diagrammatic sketches of the strut unit and the POCS catalyst slice are shown in Figure 1.

The three strut structures were constructed by the rectangular rod (RR), cylinder rod (CR), and spherical cut (SC), respectively. The elementary cell of the POCS is a 5 mm (d_{cell}) cube for RR and CR. The cell size of SC depends on the center distance (D_{dist}) of spheres. The study focused on the influences of d_{rod} and D_{dist} to the heat transfer performances of sliced Ni/Al_2O_3 (Ni-15%wt) catalyst region in the solar reactor (shown in Figure 2).

The DRM process was investigated in the self-design partition-cavity solar thermochemical reactor (shown in Figure 3). The reactor consists of the cavity for the heat and mass transfer the quartz window for solar radiation input. The solar radiation fluxes travel through the quartz window and reach the cavity of the receiver. The reactor

is divided into connected catalyst annular chamber and the center cavity by a transparent partition. With this unique design of the solar reactor, the incoming solar radiation can go through the catalyst region with pre-heated gases in the center cavity and prolonged gas-solid contact paths. The POCS lattices were settled in the annular catalyst chamber (100 mm height, 100 mm outer diameter, and 40 mm inner diameter). To maintain the reactor temperature and reduce the heat losses, the ceramic insulation material Al_2O_3-SiO_2 is enclosed outside the catalyst. The solar radiation was assumed uniformly distributed on the partition inner surface. A 3D steady-state model was set up to investigate the operating conditions that affect the DRM reaction rate and temperature distribution in the catalyst region using studied POCS.

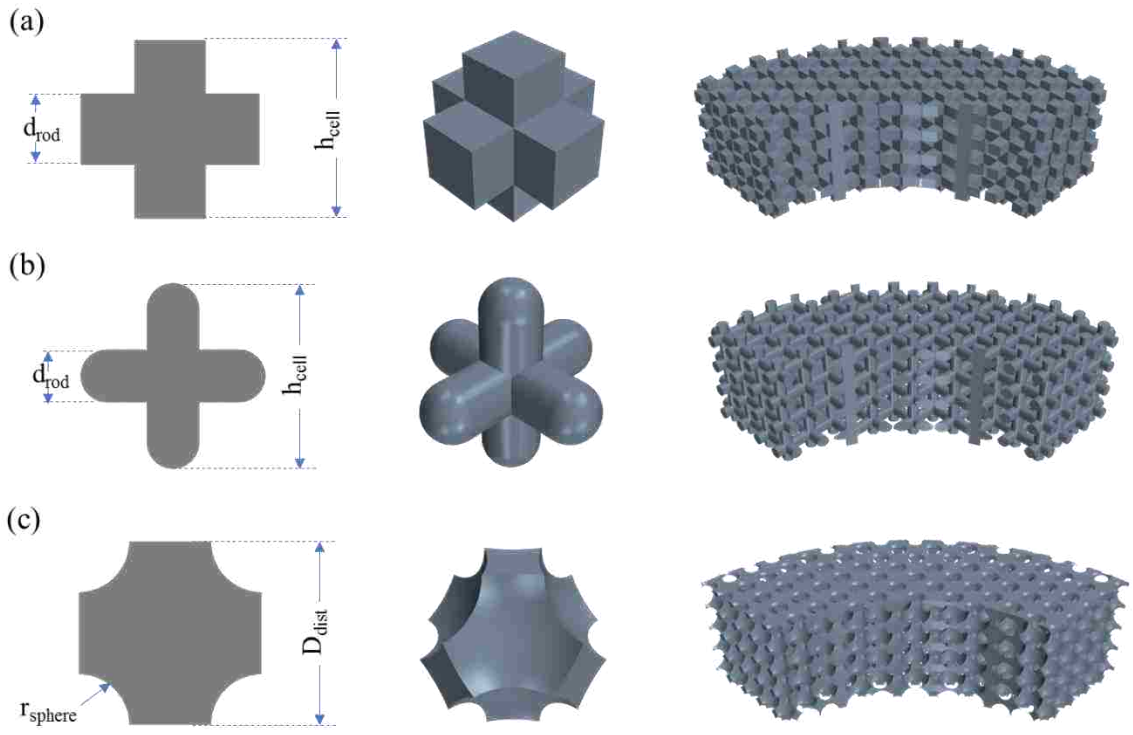

Figure 1. POCS diagrammatic sketches: (a) rectangular rod (RR), (b) cylinder rod (CR), (c) spherical cut (SC).

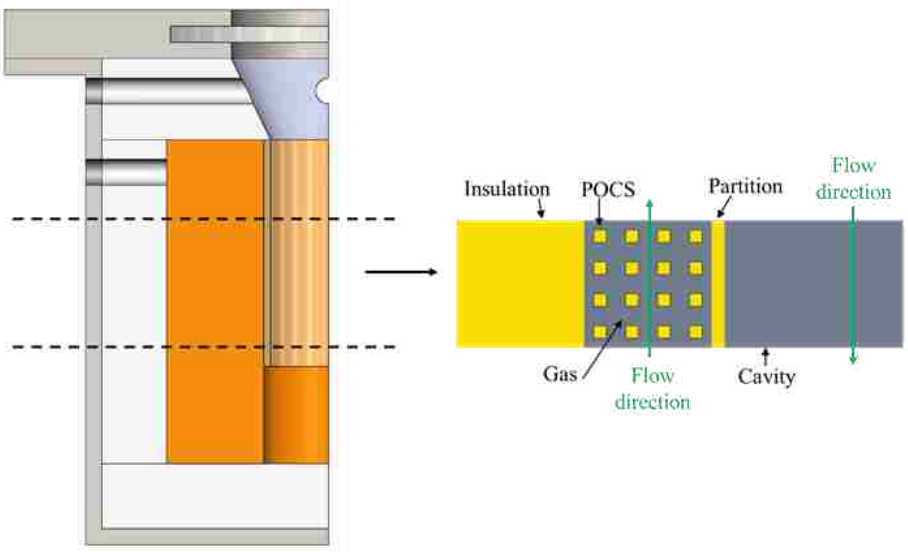

Figure 2. Schematic diagram for a sliced quarter of the reactor.

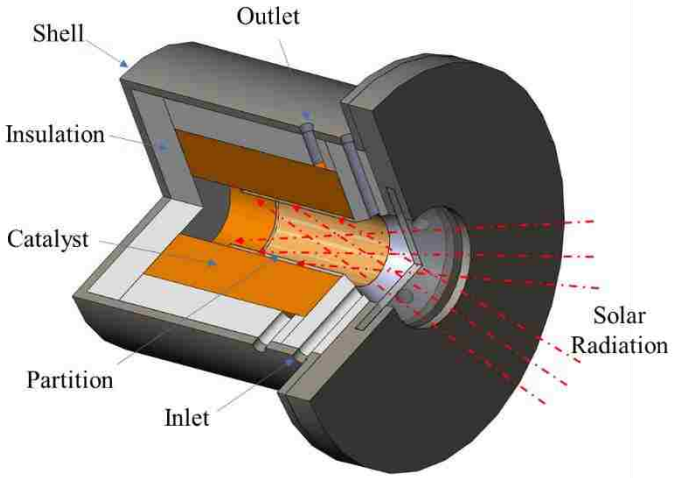

Figure 3. The schematic diagram of the partition-cavity solar thermochemical reactor.

3. METHODS

To introduce the solar radiation in the system, the discrete ordinate method (DOM) was introduced for the radiative heat transfer. The catalyst POCS was considered

as an absorbing, emitting and scattering material, which simulated via gray thermal model (the radiative properties are the same for all wavelength) [69]. A 3D flow and heat transfer model was developed to study the influences of the strut size to the flow pattern and temperature distribution. The comprehensive transfer model including the DRM reactions was further introduced in the quarter solar thermochemical reactor with steady-state laminar flow, and uniform radiative distribution. The fluid phase was divided into the non-reactive fluid region in the cavity and reactive fluid region between the partition and insulation. The solid phases include the transparent partition, the POCS, and the insulation.

3.1. MASS CONSERVATION EQUATION

The conservation equation of mass for the fluid phase is

$$\nabla \cdot \left(\rho_f \boldsymbol{v}\right) = 0 \tag{5}$$

where ρ_f is the fluid velocity, and $\boldsymbol{v}$ is the vector of fluid velocity.

3.2. MOMENTUM CONSERVATION EQUATION

The conservation equations of momentum for the non-reactive fluid phase in the cavity (Eq. (6)) and reactive fluid region are

$$\nabla\left(\rho_f \boldsymbol{v} \cdot \boldsymbol{v}\right) = -\nabla p + \nabla \cdot \left(\mu_f \nabla \boldsymbol{v}\right) + \rho g \tag{6}$$

$$\nabla\left(\rho_f \boldsymbol{v} \cdot \boldsymbol{v}\right) = -\nabla p + \nabla \cdot \left(\mu_f \nabla \boldsymbol{v}\right) + \rho g + S_m \tag{7}$$

where p is the pressure, μ_f is the fluid viscosity, g is the gravitational acceleration constant, and S_m is the momentum source term for the flow through the POCS. The

momentum source term considered the inertial and viscous resistance of the fluid flowing through the POCS, which is represented as:

$$S_m = -(\frac{\mu_f}{\alpha}\boldsymbol{v} + C_2\frac{1}{2}\rho_f|v|\boldsymbol{v}) \quad (8)$$

where α is the permeability, and C_2 is the inertial resistance coefficient. The coefficients for RR, CR, and SC can be derived from the previous works by Lacroix et al. [70] and Wu et al. [71].

3.3. ENERGY CONSERVATION EQUATION

The conservation equation of energy for the fluid regions can be written as:

$$\nabla(\rho_f H_f \boldsymbol{v}) = \nabla \cdot (k_f \nabla T_f) + q_{conv,fp} + \nabla \cdot q_r \quad (9)$$

$$\nabla(\rho_f H_f \boldsymbol{v}) = \nabla \cdot (k_{eff,f} \nabla T_f) + q_{conv,fs} + \nabla \cdot q_r + S_E \quad (10)$$

where is H_f the fluid enthalpy, k_f is the thermal conductivity of the fluid in the cavity, $k_{eff,f}$ is the effective thermal conductivity of the fluid in the catalyst region, T_f is the temperatures of the fluid phase, $q_{conv,fp}$ is the convective heat transfer between the fluid and the partition, $q_{conv,fs}$ is the convective heat transfer of fluid in the catalyst region, q_r is the radiant heat flux, and S_E is the energy source term due to the DRM reaction.

The energy conversation equations for solid regions (partition, POCS, and insulation) are listed below.

$$\nabla(\rho_p H_p) = \nabla \cdot (k_p \nabla T_p) + q_{conv,pf} + S_{rad} \quad (11)$$

$$\nabla(\rho_s H_s) = \nabla \cdot (k_{eff,s} \nabla T_s) + q_{conv,sf} + \nabla \cdot q_r \quad (12)$$

$$\nabla(\rho_n H_n) = \nabla \cdot (k_n \nabla T_n) + q_{conv,nf} \quad (13)$$

where the densities of partition, POCS, and insulation are demonstrated by ρ_p, ρ_s, and ρ_n, the enthalpies of the three regions are represented by H_p, H_s, and H_n, k_p and k_n are the thermal conductivity of the partition and the insulation, $k_{eff,s}$ is the solid effective thermal conductivity of the POCS, ∇T_p, ∇T_s, and ∇T_n separately represent the temperature of the partition, the POCS, and the insulation, $q_{conv,pf}$, $q_{conv,sf}$, and $q_{conv,nf}$ are the convective heat transfer of the partition, the POCS, and the insulation, S_{rad} is the radiation source term.

The effective thermal conductivity of the fluid and solid in the catalyst region can be computed as [72]:

$$k_{eff,f} = \chi k_f \tag{14}$$

$$k_{eff,s} = \frac{1}{3}(1-\chi)k_s \tag{15}$$

where χ is the porosity of the catalyst region, k_s is the thermal conductivity of the POCS. The general form of convective heat transfer in Eq. (9) – Eq. (13) can be expressed as

$$q_{conv,ij} = h_{conv,ij}(T_j - T_i) \tag{16}$$

where *i* represents the phase of the first letter in the subscript, and *j* represents the phase of the second letter.

The DOM approach was applied to simulate the radiative heat transfer in the system. To derive the S_{rad}, the radiative transfer equation (RTE) should be solved [73]:

$$\frac{dI}{ds} = -\beta I + \kappa_a I_b + \frac{\kappa_s}{4\pi}\int_{4\pi} I\Omega d(\Omega) \tag{17}$$

where I is the radiative intensity, I_b is the black body intensity, β is the extinction coefficient ($\beta = \kappa_a + \kappa_s$), κ_a and κ_s are the absorption coefficient and scattering coefficient, s is the distance in the Ω direction, and Ω is the solid angle.

The divergence of radiative heat flux can be expressed as [73]:

$$\nabla \cdot q_r = \kappa_a(4\pi I_b - \int_{4\pi} I \, d\Omega) \tag{18}$$

The energy source term due to the reaction (S_E) is based on the reaction rate and the reaction enthalpy, which can be shown as:

$$S_E = R_{DRM}H_{DRM} + R_{RWGS}H_{RWGS} \tag{19}$$

The H_{DRM} and H_{RWGS} are the reaction enthalpies, and R_{DRM} and R_{RWGS} are the reaction rate for the DRM and the side reaction RWGS, which are discussed in the following section.

3.4. SPECIES CONSERVATION EQUATION

The conservation equation for species mass transfer can be calculated as:

$$\nabla \cdot (\rho \boldsymbol{v} Y_i) = -\nabla \cdot \boldsymbol{J}_i + R_i \tag{20}$$

where Y_i is the species mass fraction, $\boldsymbol{J}_i$ is the diffusive mass flux, and R_i is the species reaction rate. The reaction rate of the DRM can be calculated based on regarding the reverse Boudouard reaction as the RDS [74], which is shown as the form of LH model:

$$R_{DRM} = \frac{k_1 P_{CH_4} P_{CO_2}}{(1 + K_1 P_{CH_4})(1 + K_2 P_{CO_2})} \tag{21}$$

where k_1 is the reaction rate constant, K_1 and K_2 are the equilibrium constants, P_{CH_4} and P_{CO_2} are the partial pressures for CH_4 and CO_2. The parameters can be derived from the

experimental data from the work of Wang et al. [74]. The reaction rate of the RWGS side reaction was considered as a volumetric reaction and expressed by the Arrhenius expression

$$k_{RWGS} = Ae^{-E_a/RT} \quad (22)$$

where k_{RWGS} is the reaction rate constant of the RWGS, A is the pre-exponential factor, E_a is the activation energy, and R is the gas constant. The values of reaction parameters are $A = 3.19 \times 10^4$ and $E_a = 16.3\ kJ\ mol^{-1}$ [75,76].

The methane conversion is a crucial parameter to describe the performance of the DRM, which can be calculated as:

$$X_{CH_4} = \frac{\dot{V}_{CH_{4,i}} - \dot{V}_{CH_{4,o}}}{\dot{V}_{CH_{4,i}}} \times 100\% \quad (23)$$

where $\dot{V}_{CH_{4,i}}$ and $\dot{V}_{CH_{4,o}}$ respectively represent the inlet and out methane volume flow rates, and X_{CH_4} is the methane conversion.

3.5. BOUNDARY CONDITIONS AND THERMAL PROPERTIES

For the sliced catalyst heat transfer study, the two fluid regions were considered with different flow directions with the same volume flow rate ($\dot{V}$= 4 L min^{-1}) of CH_4. The inlet temperature equals to 300 K. The outlet pressure was set as zero (the atmosphere pressure as the reference pressure). A uniform radiative flux (100 kW m^{-2}) was distributed on the partition inner surface. The periodic surface condition was used for the faces due to the quarter cut. The heat capacity (c_p) and thermal conductivity (k_f)of the CH_4 were temperature-dependent variable. The density, heat capacity, thermal

conductivity, and emissivity of the POCS catalyst is 2726 kg m^{-3}, 1045 J $kg^{-1}K^{-1}$, 3.92 W $m^{-1}K^{-1}$, and 0.92, respectively [45]. The densities of partition and insulation are 2500 kg m^{-3} and 560.65 kg m^{-3}, respectively [77,78]. The transparent partition has a transmissivity equals to 0.86 and the emissivity equals to 0.08 [79]. The thermal properties of the partition and the insulation are also temperature-dependent.

Table 1. Heat transfer coefficients for species.

Species	$A_{i,0}$	$A_{i,1}$	$A_{i,2}$	$A_{i,3}$	$A_{i,4}$	Range
CH_4	0.7787	0.0175	2.7834E-5	3.0497E-8	-1.2239E-11	200–1000 K
	1.6835	0.0102	-3.875E-6	6.7856E-10	-4.5034E-14	1000–5000 K
CO_2	2.2757	0.0099	-1.041E-5	6.8667E-9	-2.1173E-12	200–1000 K
	4.4536	0.0031	-1.278E-6	2.394E-10	1.6690E-14	1000–5000 K
CO	3.2625	0.0015	-3.8818E-6	5.5819E-9	-2.4749E-12	200–1000 K
	3.0251	0.0014	-5.6308E-7	1.0186E-10	-6.9109E-15	1000–5000 K
H_2	3.2981	8.2494E-4	-8.1430E-7	-9.4754E-11	4.1349E-13	200–1000 K
	2.9914	7.0006E-4	-5.6338E-8	-9.2316E-12	1.5828E-15	1000–5000 K
H_2O	3.3869	0.0035	-6.3547E-6	6.9686E-9	-2.5066E-12	200–1000 K
	2.6721	0.0031	-8.7303E-7	1.201E-10	-6.3916E-15	1000–5000 K
Partition	-0.173	0.1791	-0.0001	0	0	273–847 K
	61.717	0.0072	0	0	0	847–2000 K
Insulation	447.70	1.5987	1.3797E-3	4.0E-7	0	200–1480 K
	1118.44	0	0	0	0	1480–5000 K

For the reaction performance study in the quarter reactor, the inlet and outlet conditions are the same as the former study. The thermal properties of the gaseous

mixture were both temperature and composition-dependent, which are expressed in the form of polynomial in Eq. (24) and Eq. (25). The corresponding coefficients are listed in Table 1 [77,78,80] and Table 2 [46,78,81], respectively.

$$\frac{c_{p,i}}{R} = A_{i,0} + A_{i,1}T_f + A_{i,2}T_f^2 + A_{i,3}T_f^3 + A_{i,4}T_f^4 \quad (24)$$

$$k_i = B_{i,0} + B_{i,1}T_f + B_{i,2}T_f^2 + B_{i,3}T_f^3 \quad (25)$$

Table 2. Thermal conductivity coefficients for species.

Species	$B_{i,0}$	$B_{i,1}$	$B_{i,2}$	$B_{i,3}$
CH4	-1.869E-3	8.727E-5	1.179E-7	-3.614E-11
CO2	-7.215E-3	8.015E-5	5..477E-9	-1.053E-11
CO	5.067E-4	9.125E-5	-3.524E-8	8.199E-12
H2	8.099E-3	6.689E-4	-4.158E-7	1.562E-10
H2O	7.341E-3	-1.013E-5	1.801E-7	-9.100E-11
Partition	1.18	3.14E-3	$17966/T^4$	0
Insulation	0.019654	0.00012926	0	0

3.6. NUMERICAL IMPLEMENTATION AND VALIDATION

The transport equations with chemical reactions were solved by the finite volume method (FVM) in STAR-CCM+ v. 12.06. The polyhedral meshes were generated for studies regions. The second-order segregated flow solver (coupling the SIMPLE and PISO algorithms) was utilized for the pressure-velocity coupling. The segregated fluid enthalpy and segregated species solver were applied to solve the corresponding energy and species equations. The radiation was implemented by the DOM with S4 ordinate sets.

In order to reduce the influences of meshes to the results, the mesh independency analysis was applied to the study by considering the three types of the POCS, separately. The number of mesh cells was increased from 60,000 to 3,650,000 for a quarter of the reactor. The methane conversion and the average temperatures of fluid and the POCS catalyst are shown in Figure 4. It is clearly seen that the values of the studied variables change less than 1 % when the number of cells is larger than 1,100,000. Considering the accuracy of results and calculation cost, the 1,100,000 meshes were selected for the following studies.

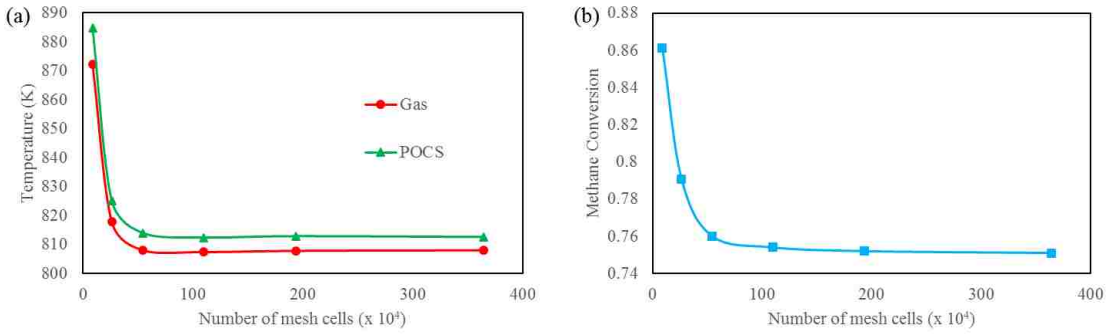

Figure 4. Mesh independency analysis for the quarter of the reactor.

The radiative and energy models were validated against the experimental work done by Wu et al. [71] in a volumetric solar reactor with adjusted solar concentrated fluxes with Gaussian distribution. The position-dependent temperature distributions of the numerical and experimental results are compared in Figure 5, which shows a satisfactory agreement. The chemical reaction model was verified by comparing the simulation results with experimental data derived from Lu et al. [45] in a tubular packed bed reactor. As presented in Figure 6, the predicted numerical results of methane

conversions are close to the values from the experiments in the range of 650 °C to 800 °C.

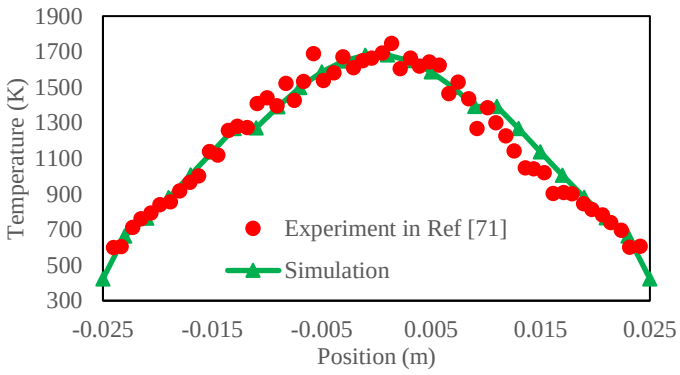

Figure 5. Temperature distribution for the validation of the radiative and energy model.

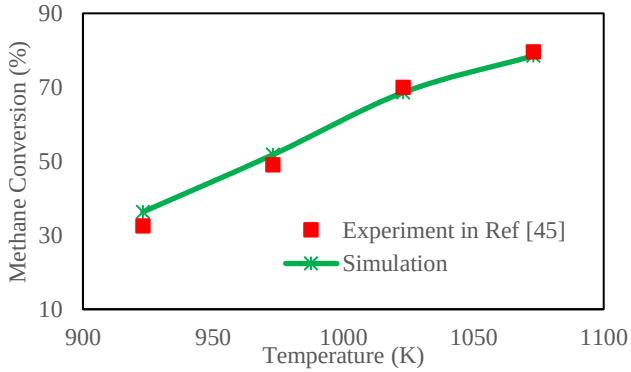

Figure 6. Methane conversion for the validation of the chemical reaction model.

4. RESULTS AND DISCUSSIONS

4.1. HEAT TRANSFER FOR THE SLICED QUARTER OF THE REACTOR

The heat transfer performances of the three types of the POCS (RR, CR, SC) lattices were investigated by varying the strut parameters in a sliced 20 mm height sliced reactor. Table 3 shows the parameters of the studied struts and the corresponding void

fraction (χ) and specific surface area (SSA) of the POCS lattices. The opposite flow directions in the cavity and catalyst region were used to capture the heat convection of both sides of the partition. The temperature contours of the side-section and the POCS lattices are shown in Figure 7. One of the obvious phenomena that can be found from the Figure 7 is that the case with a thinner strut (larger void fraction) shows a higher temperature gradient from the partition (direct radiation acceptor) to the insulation, which indicates that the conduction is the dominant in the entire heat transfer. To further investigate the influences, the incident radiation distributions of RR were shown in Figure 8. The incident radiation shows a higher value of the partition for the case with a thicker strut, which embodies the opposite trend with the temperature profile. Moreover, the thicker strut impedes the radiative transfer in the radial direction of the catalyst region due to the lower void fraction. Considering these two points, rthe adiative transfer can hardly play the key role in the comprehensive heat transfer, which reveals the predominance of conduction.

Comparing the temperature scales for different shapes of the struts, the SC performed higher temperature with similar values for the other two shapes. It is a bi-functional result of the conduction and the radiation. Comparing the thinnest strut for all shapes, as the contact area between the SC ($2.53 \times 10^{-4} m^2$) and the partition is larger than that of RR ($7.08 \times 10^{-5} m^2$) and CR ($9.36 \times 10^{-5} m^2$), it can capture more incoming radiative energy. However, the energy transfer in the SC is limited due to its volume, the accumulated energy is shared with the partition and causes a higher temperature.

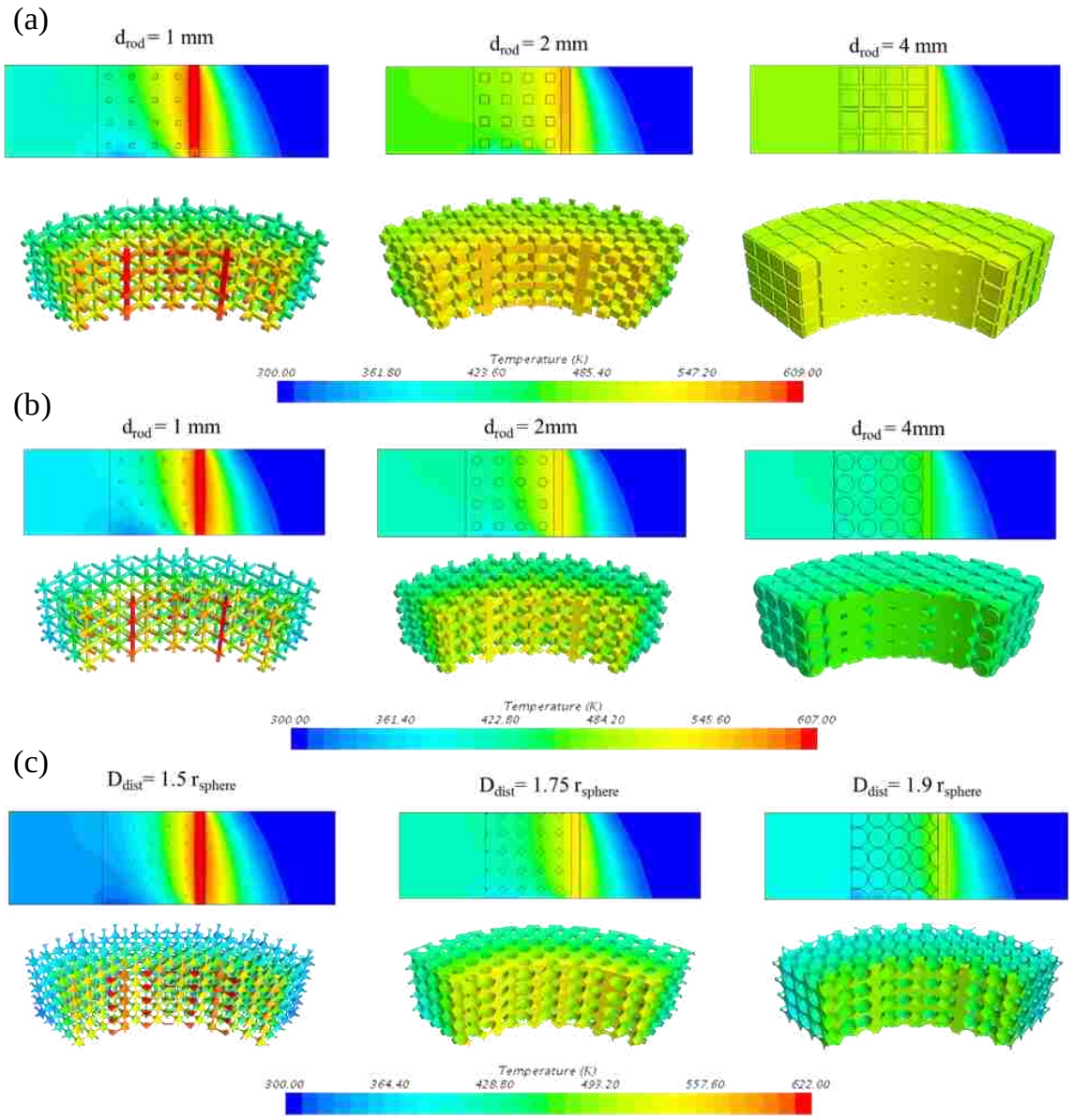

Figure 7. Temperature contours in the sliced quarter of the reactor with different POCS lattices: (a) RR; (b) CR; (c) SC.

To quantification the influences of the strut thicknesses to the temperature distribution, a line probe was implanted in the radial direction of the sliced reactor for each case and the results are shown in Figure 9. For the three different POCS, the temperature profiles show quite similar shapes. In the cavity region, the temperature stays

in the level of the inlet temperature in the range of 0.0 to 0.01 m. After that, the temperature experiences a sharp increase due to the radiation and boundary layer effect. The temperature reaches the peak value around 0.03 m (the partition surface) since the partition is the direct radiation acceptor. Furthermore, the temperature encounters a decrease in the catalyst region between 0.03 m to 0.05 m. In the insulation region, the temperature variation is almost inconspicuous in the insulation region. Considering the same shape of the POCS, the thinnest strut experiences the sharpest temperature descend ($\Delta T_{RR,1mm} = 204.5K$, $\Delta T_{CR,1mm} = 234.7K$, $\Delta T_{SC,1.5r_{sphere}} = 281.6K$). On the contrary, the temperature differences between the inner and outer of the catalyst annular are much smaller ($\Delta T_{RR,1mm} = 32.6K$, $\Delta T_{CR,1mm} = 44.2K$, $\Delta T_{SC,1.5r_{sphere}} = 97.1K$) for thicker struts. However, the reduced temperature differences sacrifice the input solar power to heat the insulation, which should be kept at a low temperature. Furthermore, the thick strut causes a low void fraction and SSA, which is disadvantageous to the subsequent DRM reactions. Considering the temperature distribution and effective porous structure for the reactions, the middle case of each type of the POCS were selected for the following study of the DRM reactions.

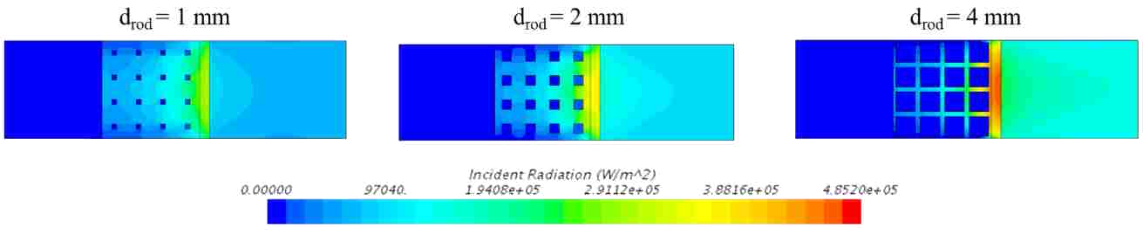

Figure 8. Incident radiation distribution of RR with different rod sizes.

Table 3. Parameters for the POCS lattices.

Rectangular rod (RR) lattice			
d_{rod} (mm)	h_{cell} (mm)	χ	SSA (m^2/kg)
1	5	0.896	1.352
2	5	0.648	0.6
4	5	0.104	0.157
Cylinder rod (CR) lattice			
d_{rod} (mm)	h_{cell} (mm)	χ	SSA (m^2/kg)
1	5	0.926	1.460
2	5	0.721	0.632
4	5	0.219	0.200
Spherical cut (SC) lattice			
r_{sphere} (mm)	D_{dist} (mm)	χ	SSA (m^2/kg)
2.5	1.5 r_{sphere}	0.924	1.746
2.5	1.75 r_{sphere}	0.722	0.794
2.5	1.9 r_{sphere}	0.623	0.639

From Table 3, the 2 mm CR and 1.75 r_{sphere} SC have rather close void fractions, the effects of the POCS shapes on the temperature profiles in the catalyst region would be attractive. The SC shows a higher peak and average temperatures (9 K differences from perk temperature and 5 K difference for average temperature), which means the SC is in the ascendant in the heat transfer under the same void fraction. As the 2 mm CR and the 1.9 r_{sphere} SC have similar SSA, the temperature profiles are compared to study the influences of the POCS shapes. The result is clear that 2 mm CR shows a prominent advantage on the temperature distribution in the catalyst region than the SC, which is owed to the larger void fraction. Hence, a larger void fraction of the POCS is favorable for the heat transfer under the same SSA.

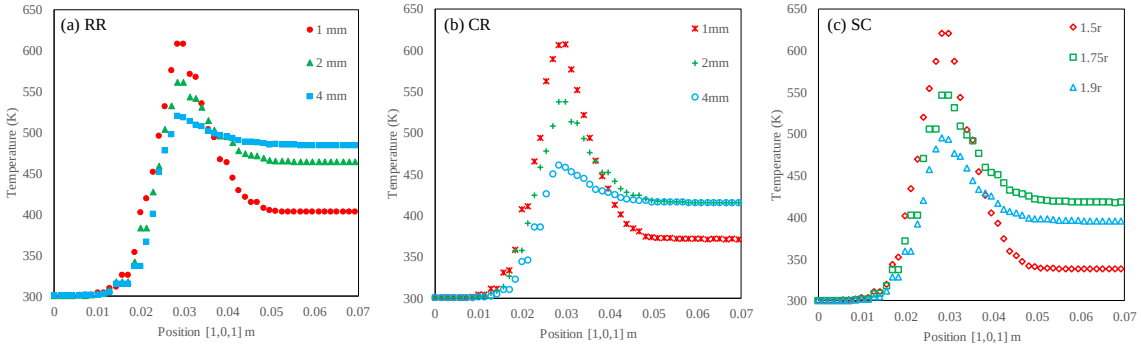

Figure 9. Temperature distributions in the radial direction.

4.2. DRM REACTIONS IN THE QUARTER OF THE REACTOR

4.2.1. Gas Flow Rate. The inlet gas flow rate is an important parameter that affects the temperature distribution in the reactor and the thermochemical reaction performances. The inlet gas flow rates in the range of 2 L min^{-1} to 8 L min^{-1} were investigated in this work. The 50 kW m^{-2} radiative flux was uniformly distributed on the partition inner surface. The CH_4 and CO_2 were equally fed into the reactor. The temperature contours for five selected gas flow rates (2 L min^{-1}, 4 L min^{-1}, 5 L min^{-1}, 6 L min^{-1}, 8 L min^{-1}) were shown in Figure 10. The 2 L min^{-1} flow rate has a remarkable advantage on deriving a higher temperature compared with the other cases for all the three types of the POCS. The temperature distributions experience a slow decrease from 4 L min^{-1} to 8 L min^{-1}.

To further investigate the temperature distribution in the catalyst region, the maximum, average, and minimum temperature of the catalyst region were monitored and shown in Figure 11. The maximum and average temperature curves show similar tendencies with the increase of gas flow rate for different POCS.

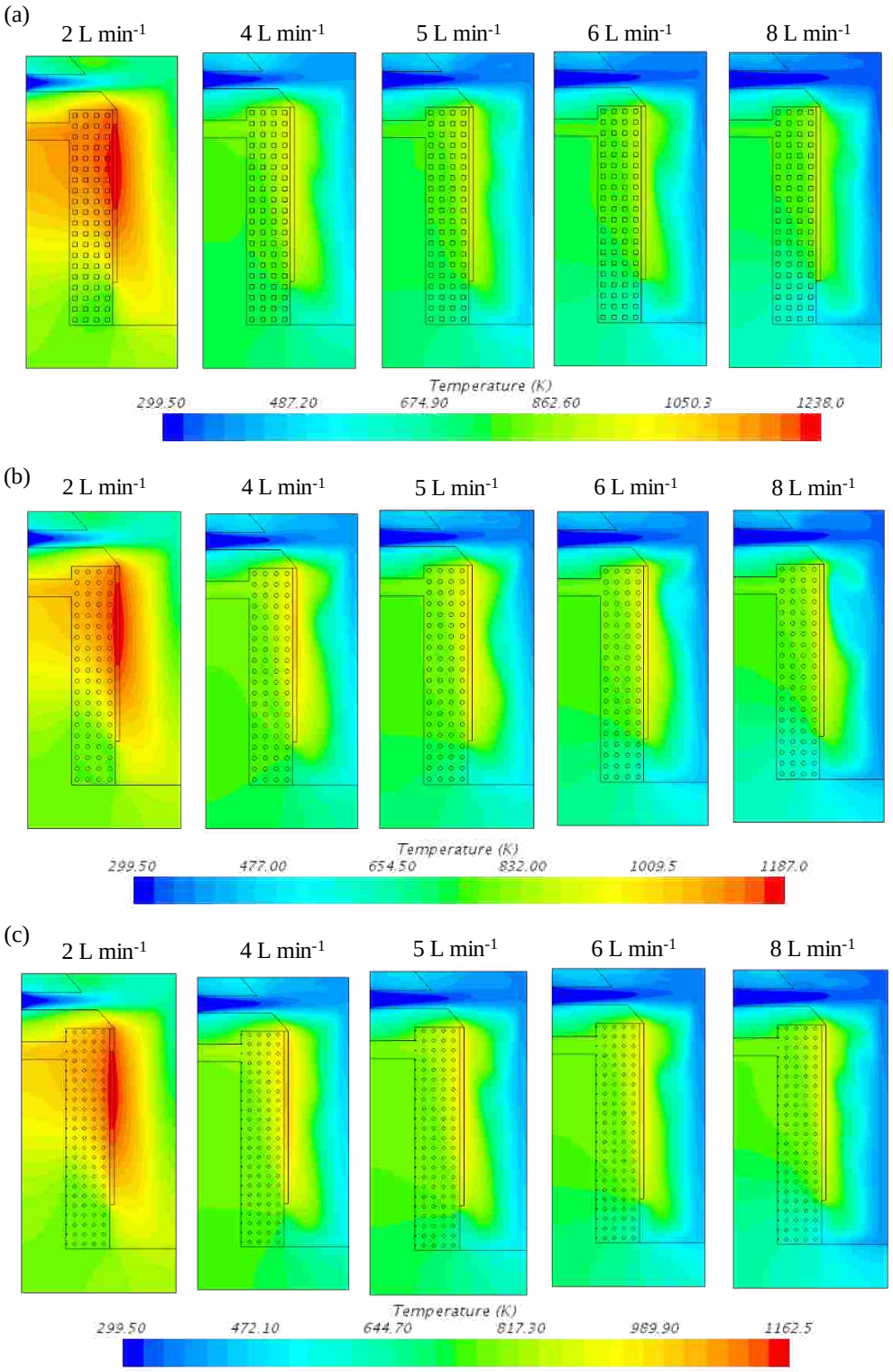

Figure 10. Temperature contours of different inlet gas flow rates for various types of POCS: (a) RR; (b) CR; (c) SC.

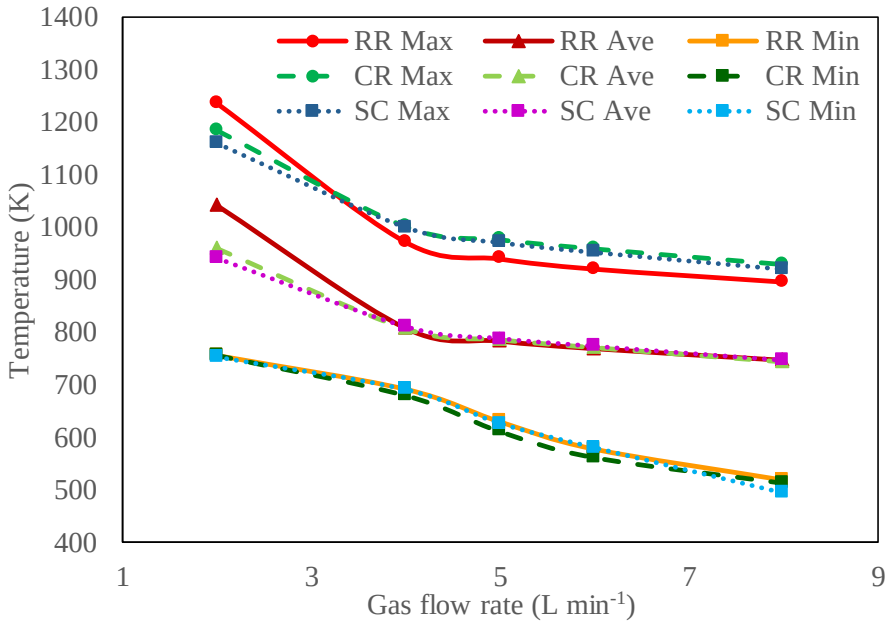

Figure 11. Effect of gas flow rate to the temperature distributions in the catalyst region with various POCS.

The temperature differences between 2 L min^{-1} and 4 L min^{-1} are around 200 K, however, only about 100 K temperature decrease occurs when the flow rate increases from 4 L min^{-1} to 8 L min^{-1}. The minimum temperature curves show diverse trends compared with the maximum and the average temperature curves, since the minimum temperature in the catalyst region is near the interfaces between the cavity and the catalyst region, which was affected by the heat transfer in the cavity region. A higher temperature derived from 2 L min^{-1} case indicates that the low gas flow rate is favorable for the pre-heating in the cavity region and simultaneously obtain a higher temperature in the catalyst region, which is beneficial for the reaction rates.

The temperature differences among the POCS lattices only reflect on the cases with 2 L min^{-1} flow rate. When the gas flow rate is larger than 4 L min^{-1}, the temperatures

are quite close to each other. As the temperature distribution is caused by the multifunctional results of the heat transfer, at a lower gas flow rate (2 L min^{-1}), the structures of the POCS lattice has an obvious influence on the temperature distribution, however, with the gas flow rate increase, this influence is weakened due to the enhancement of the convection.

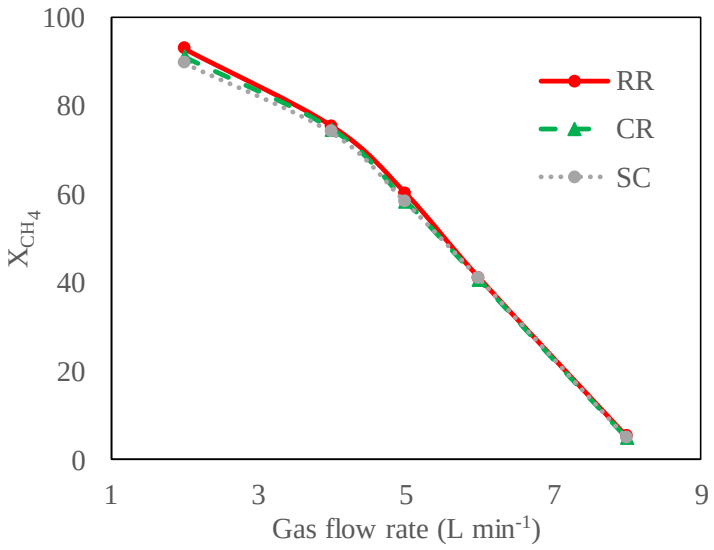

Figure 12. Methane conversion under different gas flow rates.

The methane conversions for the three POCS lattices under various gas flow rates were shown in Figure 12. With the gas flow rate increases, the methane conversions experience a continuous descend, which reduce from around 90% (2 L min^{-1}) to 5% (8 L min^{-1}). The low conversion of 8 L min^{-1} is mainly caused by the low temperature in the catalyst region. Generally, the DRM reactions were investigated around 973 K to 1273 K to derive an industrial comparable conversion [82]. Very seldom studies focused the DRM reactions with the temperature lower than 773 K [83]. In this study, the DRM

reactions were initiated when the temperature is higher than 773 K. Considering the temperature distribution of 8 L min^{-1} shown in Figure 11, the low methane conversion is due to the low temperature.

4.2.2. Radiant Flux. As DRM reactions are endothermic processes, the radiative fluxes, which work as the energy source, directly affect the temperature distributions in the reactor. Besides, the DRM reactions should be proceeded in the appropriate temperature ranges to ensure the reaction can occur but avoid the catalyst deactivation. Four different radiant fluxes (10 kW m^{-2}, 25 kW m^{-2}, 50 kW m^{-2}, 75 kW m^{-2}) were chosen to investigate their influences on the temperature profiles and the methane conversions. The CH_4 and CO_2 are equally feed in the reactor at a total volume flow rate of 4 L min^{-1}. The temperature contours of different radiant fluxes are shown in Figure 13. The catalyst region can obtain higher temperatures with the increase of the radiant fluxes. For the different types of POCS lattices, the temperature ranges are rather close to each other, but the RR shows a higher maximum temperature. The reason is just the same as discussed above that the RR has a lower void fraction which can absorb more energy. The methane conversions under various radiant fluxes are shown in Figure 14. From the figure, the conversion has little differences among the three types of the POCS when the radiant flux is less than 50 kW m^{-2}. Even though the RR has a lower void fraction and SSA compared with the other two types of the POCS, it drives to a higher conversion due to the higher temperature in the catalyst region. This result reveals that the temperature has a stronger influence on methane conversion. Moreover, the influence of radiant fluxes to the methane conversion is not linear. The differences of methane conversion between 50 kW m^{-2} and 75 kW m^{-2} are around 3%, which are much smaller than the growth with

less than 50 kW m^{-2} radiant fluxes. Considering the energy efficiency, it is better to increase the methane conversion by other approaches like the gas flow rate when the radiant fluxes reach certain values.

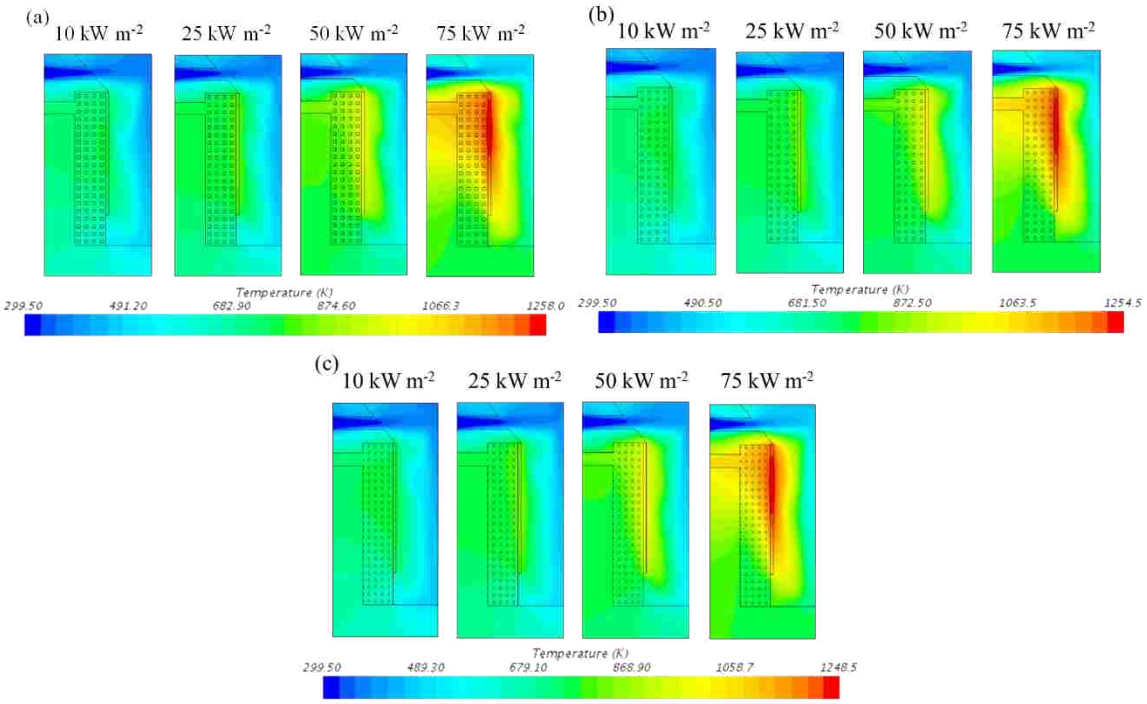

Figure 13. Temperature contours under different radiant fluxes: (a) RR; (b) CR; (c) SC.

4.2.3. Ratio of Reactants. The reactant ratio is crucial to reaction performances. Theoretically, the DRM can generate the syngas with an equal amount of CO and H_2 when the reactant feed is 1:1, however, the RWGS side reaction is hard to avoid during the entire thermochemical process. To investigate the influences of the ratio of reactants on the generation of products, the different proportions of CH_4 to CO_2 in the feedstock were tested (from 2:1 to 1:2). The inlet gas flow rate was 4 min^{-1} and the radiant flux was 50 kW m^{-2}. The methane conversions under different feed ratios are shown in Figure 15.

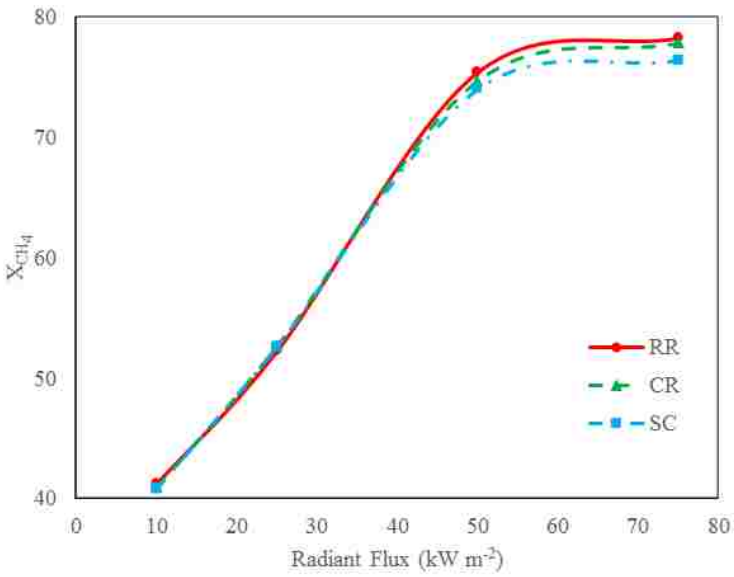

Figure 14. Methane conversions of various POCS lattices under different radiant fluxes.

Since the CO_2 is consumed in the RWGS reaction simultaneously, the excess CO_2 is favorable to increase the methane conversion. All the three types of the POCS show the highest methane conversion (over 90%) derived at the CH_4/CO_2 ratio equaling to 1/2. To further investigate the influences caused by the CH_4/CO_2 ratio, the relation between methane reaction rate and the temperature in the catalyst region is shown in Figure 16. A higher methane reaction rate corresponding to a lower temperature due to the endothermic DRM and RWGS reactions. When the ratio of CH_4/CO_2 equals to 1, the methane reaction rate is the highest. As the ratio is larger than 1, the insufficient CO_2 restrict the conversion of methane, which leads to a lower reaction rate. When the ratio is smaller than 1, though the excess CO_2 can lead to a higher methane conversion, the original concentration of methane is limited, which reduces the methane reaction rate. The influences of the POCS on the methane reaction rate are very small under the same

CH_4/CO_2 ratio. In this study, the chemical reaction mechanism did not include the effects of the active site, therefore, under the assumption of the equal amount sites, the influences of the SSA is limited to the reaction rate.

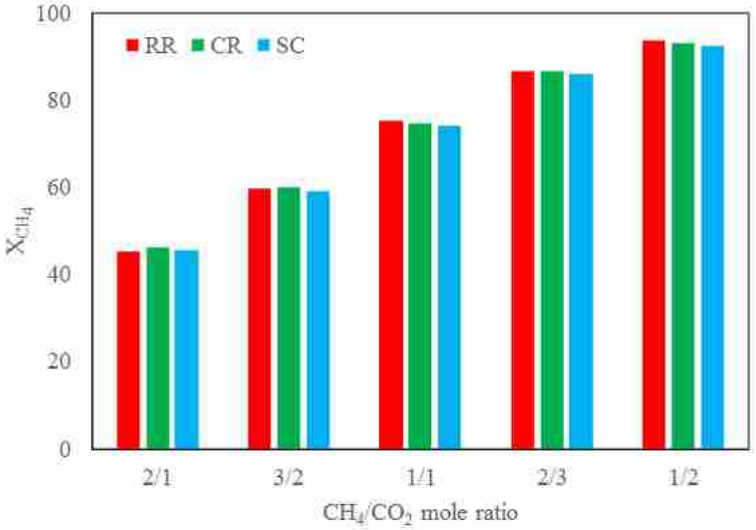

Figure 15. Effect of reactant feed ratio to the methane conversion.

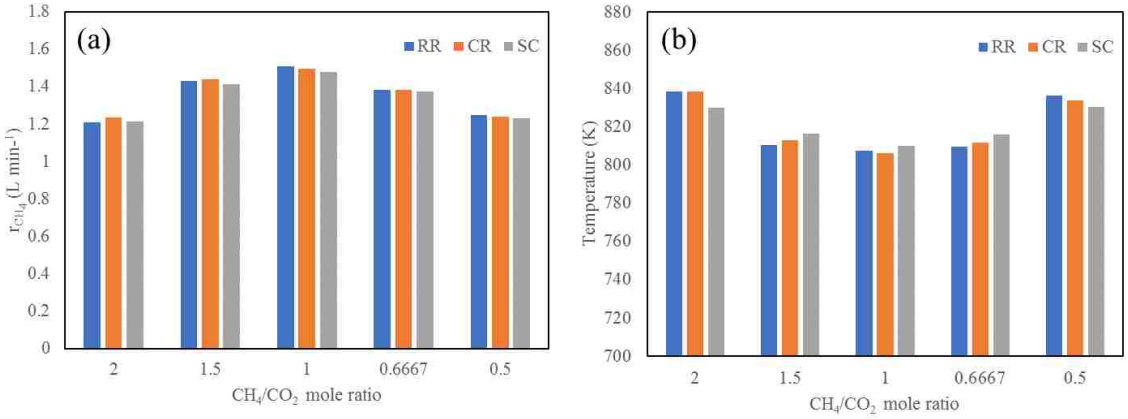

Figure 16. Effect of reactant feed ratio to the methane reaction rate and the temperature.

5. CONCLUSIONS

In this paper, the three different types of POCS lattices were studied in the partition-cavity solar thermochemical reactor for the DRM process via FVM. The numerical models were validated against previously published experimental works and show satisfactory agreements. The influences of the strut thickness on the heat transfer performances were investigated in the sliced solar reactor and the operating conditions of the DRM process were studied in the quarter of the solar thermochemical reactor with the POCS catalyst. The conclusions are drawn as follows:

(1) The heat conduction of the POCS plays a dominant role in the temperature distribution in the catalyst region.

(2) The SC lattice has the advantage to derive a higher perk and average temperature than the CR under the same void fraction, however, the CR performs better on the heat transfer than the SC when the SSA is the same.

(3) Under the same radiant fluxes, a slower gas flow rate is favorable to derive enough reaction temperature, which leads to a higher methane conversion.

(4) The relation between methane conversion and the radiant flux is not linear. After a certain radiant flux value, the methane conversion increases slow. For the purpose of energy efficiency, an appropriate radiant flux should be selected.

(5) Under the present reaction mechanisms, the influences of the POCS on the reaction rate and the methane conversion are not significant under the assumption of equal active sites. For further investigation, the microkinetics including site reactions should be taken into consideration in the future work.

ACKNOWLEDGEMENT

We gratefully acknowledge the financial support from the Wayne and Gayle Laufer Foundation.

REFERENCES

[1] J. Conti, P. Holtberg, J. Diefenderfer, A. LaRose, J.T. Turnure, L. Westfall, International energy outlook 2016 with projections to 2040, USDOE Energy Information Administration (EIA), Washington, DC, United States, 2016.

[2] USDOE Energy Information Administration (EIA), Where Greenhouse Gases Come From, (2018). https://www.eia.gov/energyexplained/index.php?page=environment_where_ghg_come_from.

[3] H. Tian, C. Lu, P. Ciais, A.M. Michalak, J.G. Canadell, E. Saikawa, D.N. Huntzinger, K.R. Gurney, S. Sitch, B. Zhang, The terrestrial biosphere as a net source of greenhouse gases to the atmosphere, Nature. 531 (2016) 225.

[4] M. De Falco, G. Iaquaniello, G. Centi, CO2: a valuable source of carbon, Springer, 2013.

[5] E. Alper, O.Y. Orhan, CO2 utilization: Developments in conversion processes, Petroleum. 3 (2017) 109–126.

[6] Y.-H. Luo, R. Chen, L.-L. Wen, F. Meng, Y. Zhang, C.-Y. Lai, B.E. Rittmann, H.-P. Zhao, P. Zheng, Complete perchlorate reduction using methane as the sole electron donor and carbon source, Environ. Sci. Technol. 49 (2015) 2341–2349.

[7] D. Bastviken, J. Ejlertsson, I. Sundh, L. Tranvik, Methane as a source of carbon and energy for lake pelagic food webs, Ecology. 84 (2003) 969–981.

[8] J. Baltrusaitis, W.L. Luyben, Methane conversion to syngas for gas-to-liquids (GTL): is sustainable CO2 reuse via dry methane reforming (DMR) cost competitive with SMR and ATR processes?, ACS Sustain. Chem. Eng. 3 (2015) 2100–2111.

[9] D.R. Caulton, P.B. Shepson, R.L. Santoro, J.P. Sparks, R.W. Howarth, A.R. Ingraffea, M.O.L. Cambaliza, C. Sweeney, A. Karion, K.J. Davis, Toward a better understanding and quantification of methane emissions from shale gas development, Proc. Natl. Acad. Sci. (2014) 201316546.

[10] U. Izquierdo, V.L. Barrio, J. Requies, J.F. Cambra, M.B. Güemez, P.L. Arias, Tri-reforming: a new biogas process for synthesis gas and hydrogen production, Int. J. Hydrogen Energy. 38 (2013) 7623–7631.

[11] R. Kadam, N.L. Panwar, Recent advancement in biogas enrichment and its applications, Renew. Sustain. Energy Rev. 73 (2017) 892–903.

[12] Z. Shang, S. Li, L. Li, G. Liu, X. Liang, Highly active and stable alumina supported nickel nanoparticle catalysts for dry reforming of methane, Appl. Catal. B Environ. 201 (2017) 302–309.

[13] X. Zhang, Y. Liu, Performance assessment of CO2 capture with calcination carbonation reaction process driven by coal and concentrated solar power, Appl. Therm. Eng. 70 (2014) 13–24.

[14] T.L. LeValley, A.R. Richard, M. Fan, Development of catalysts for hydrogen production through the integration of steam reforming of methane and high temperature water gas shift, Energy. 90 (2015) 748–758.

[15] N. Gokon, Y. Osawa, D. Nakazawa, T. Hatamachi, T. Kodama, Kinetics of CO2 reforming of methane by catalytically activated metallic foam absorber for solar receiver-reactors, in: ASME 2008 2nd Int. Conf. Energy Sustain. Collocated with Heat Transf. Fluids Eng. 3rd Energy Nanotechnol. Conf., American Society of Mechanical Engineers, 2008: pp. 371–383.

[16] D. Yadav, R. Banerjee, A review of solar thermochemical processes, Renew. Sustain. Energy Rev. 54 (2016) 497–532.

[17] T. Blumberg, T. Morosuk, G. Tsatsaronis, Exergy-based evaluation of methanol production from natural gas with CO2 utilization, Energy. 141 (2017) 2528–2539.

[18] T. Yu, Q. Yuan, J. Lu, J. Ding, Y. Lu, Thermochemical storage performances of methane reforming with carbon dioxide in tubular and semi-cavity reactors heated by a solar dish system, Appl. Energy. 185 (2017) 1994–2004.

[19] C. Agrafiotis, H. von Storch, M. Roeb, C. Sattler, Solar thermal reforming of methane feedstocks for hydrogen and syngas production—a review, Renew. Sustain. Energy Rev. 29 (2014) 656–682.

[20] R.B. Diver, J.D. Fish, R. Levitan, M. Levy, E. Meirovitch, H. Rosin, S.A. Paripatyadar, J.T. Richardson, Solar test of an integrated sodium reflux heat pipe receiver/reactor for thermochemical energy transport, Sol. Energy. 48 (1992) 21–30.

[21] T. Kodama, N. Gokon, S. Inuta, S. Yamashita, T. Seo, Molten-salt tubular absorber/reformer (MoSTAR) project: the thermal storage media of Na2CO3–MgO composite materials, J. Sol. Energy Eng. 131 (2009) 41013.

[22] J.K. Dahl, A.W. Weimer, A. Lewandowski, C. Bingham, F. Bruetsch, A. Steinfeld, Dry reforming of methane using a solar-thermal aerosol flow reactor, Ind. Eng. Chem. Res. 43 (2004) 5489–5495.

[23] H.H. Klein, J. Karni, R. Rubin, Dry methane reforming without a metal catalyst in a directly irradiated solar particle reactor, J. Sol. Energy Eng. 131 (2009) 21001.

[24] H.H. Klein, R. Rubin, J. Karni, Effect of particle consumption in a particle seeded solar receiver, in: 13th Sol. PACES Int. Symp. Seville, Spain, 2006.

[25] A. Wörner, R. Tamme, CO2 reforming of methane in a solar driven volumetric receiver–reactor, Catal. Today. 46 (1998) 165–174.

[26] E.J. Sheu, E.M.A. Mokheimer, A.F. Ghoniem, A review of solar methane reforming systems, Int. J. Hydrogen Energy. 40 (2015) 12929–12955.

[27] T. Kodama, H. Ohtake, K.I. Shimizu, Y. Kitayama, Nickel catalyst driven by direct light irradiation for solar CO2-reforming of methane, Energy & Fuels. 16 (2002) 1016–1023.

[28] M. Levy, R. Rubin, H. Rosin, R. Levitan, Methane reforming by direct solar irradiation of the catalyst, Energy. 17 (1992) 749–756.

[29] N. Gokon, Y. Yamawaki, D. Nakazawa, T. Kodama, Kinetics of methane reforming over Ru/γ-Al2O3-catalyzed metallic foam at 650–900° C for solar receiver-absorbers, Int. J. Hydrogen Energy. 36 (2011) 203–215.

[30] R. Buck, J.F. Muir, R.E. Hogan, Carbon dioxide reforming of methane in a solar volumetric receiver/reactor: the CAESAR project, Sol. Energy Mater. 24 (1991) 449–463.

[31] T. Kodama, T. Moriyama, T. Shimoyama, N. Gokon, H. Andou, N. Satou, Ru/Ni–Mg–O Catalyzed SiC-Foam Absorber for Solar Reforming Receiver-Reactor, J. Sol. Energy Eng. 128 (2006) 318–325.

[32] N. Gokon, Y. Yamawaki, D. Nakazawa, T. Kodama, Ni/MgO–Al2O3 and Ni–Mg–O catalyzed SiC foam absorbers for high temperature solar reforming of methane, Int. J. Hydrogen Energy. 35 (2010) 7441–7453.

[33] X. Chen, F. Wang, Y. Han, R. Yu, Z. Cheng, Thermochemical storage analysis of the dry reforming of methane in foam solar reactor, Energy Convers. Manag. 158 (2018) 489–498.

[34] T. Kodama, A. Kiyama, K.-I. Shimizu, Catalytically activated metal foam absorber for light-to-chemical energy conversion via solar reforming of methane, Energy & Fuels. 17 (2003) 13–17.

[35] T. Kodama, A. Kiyama, T. Moriyama, O. Mizuno, Solar methane reforming using a new type of catalytically-activated metallic foam absorber, J. Sol. Energy Eng. 126 (2004) 808–811.

[36] J. Qi, Y. Sun, Z. Xie, M. Collins, H. Du, T. Xiong, Development of Cu foam-based Ni catalyst for solar thermal reforming of methane with carbon dioxide, J. Energy Chem. 24 (2015) 786–793.

[37] L. Sang, B. Sun, H. Tan, C. Du, Y. Wu, C. Ma, Catalytic reforming of methane with CO2 over metal foam based monolithic catalysts, Int. J. Hydrogen Energy. 37 (2012) 13037–13043.

[38] W. Fuqiang, C. Ziming, T. Jianyu, Z. Jiaqi, L. Yu, L. Linhua, Energy storage efficiency analyses of CO2 reforming of methane in metal foam solar thermochemical reactor, Appl. Therm. Eng. 111 (2017) 1091–1100.

[39] J.T. Richardson, S.A. Paripatyadar, Carbon dioxide reforming of methane with supported rhodium, Appl. Catal. 61 (1990) 293–309.

[40] N.E. McGuire, N.P. Sullivan, O. Deutschmann, H. Zhu, R.J. Kee, Dry reforming of methane in a stagnation-flow reactor using Rh supported on strontium-substituted hexaaluminate, Appl. Catal. A Gen. 394 (2011) 257–265.

[41] B. Lee, S. Lee, H. Lim, Numerical modeling studies for a methane dry reforming in a membrane reactor, J. Nat. Gas Sci. Eng. 34 (2016) 1251–1261.

[42] L. Yin, S. Wang, H. Lu, J. Ding, R. Mostofi, Z. Hao, Simulation of effect of catalyst particle cluster on dry methane reforming in circulating fluidized beds, Chem. Eng. J. 131 (2007) 123–134.

[43] G.D. Wehinger, T. Eppinger, M. Kraume, Evaluating catalytic fixed‐bed reactors for dry reforming of methane with detailed CFD, Chemie Ing. Tech. 87 (2015) 734–745.

[44] Y. Kathiraser, U. Oemar, E.T. Saw, Z. Li, S. Kawi, Kinetic and mechanistic aspects for CO2 reforming of methane over Ni based catalysts, Chem. Eng. J. 278 (2015) 62–78.

[45] J. Lu, Y. Chen, J. Ding, W. Wang, High temperature energy storage performances of methane reforming with carbon dioxide in a tubular packed reactor, Appl. Energy. 162 (2016) 1473–1482.

[46] W. Fuqiang, T. Jianyu, J. Huijian, L. Yu, Thermochemical performance analysis of solar driven CO2 methane reforming, Energy. 91 (2015) 645–654.

[47] M.F. Mark, W.F. Maier, F. Mark, Reaction kinetics of the CO2 reforming of methane, Chem. Eng. Technol. Ind. Chem. Equipment ‐ Process Eng. 20 (1997) 361–370.

[48] E. Akpan, Y. Sun, P. Kumar, H. Ibrahim, A. Aboudheir, R. Idem, Kinetics, experimental and reactor modeling studies of the carbon dioxide reforming of methane (CDRM) over a new Ni/CeO2–ZrO2 catalyst in a packed bed tubular reactor, Chem. Eng. Sci. 62 (2007) 4012–4024.

[49] A.M. Becerra, M.E. Iriarte, A.E.C. Luna, Catalytic activity of a nickel on alumina catalyst in the CO 2 reforming of methane, React. Kinet. Catal. Lett. 79 (2003) 119–125.

[50] Y.-A. Zhu, D. Chen, X.-G. Zhou, W.-K. Yuan, DFT studies of dry reforming of methane on Ni catalyst, Catal. Today. 148 (2009) 260–267.

[51] T. Giroux, S. Hwang, Y. Liu, W. Ruettinger, L. Shore, Monolithic structures as alternatives to particulate catalysts for the reforming of hydrocarbons for hydrogen generation, Appl. Catal. B Environ. 56 (2005) 95–110.

[52] G.D. Wehinger, C. Fütterer, M. Kraume, Contact modifications for CFD simulations of fixed-bed reactors: cylindrical particles, Ind. Eng. Chem. Res. 56 (2016) 87–99.

[53] G.D. Wehinger, F. Klippel, M. Kraume, Modeling pore processes for particle-resolved CFD simulations of catalytic fixed-bed reactors, Comput. Chem. Eng. 101 (2017) 11–22.

[54] T. Eppinger, G.D. Wehinger, N. Jurtz, R. Aglave, M. Kraume, A numerical optimization study on the catalytic dry reforming of methane in a spatially resolved fixed-bed reactor, Chem. Eng. Res. Des. 115 (2016) 374–381.

[55] G.D. Wehinger, M. Kraume, V. Berg, O. Korup, K. Mette, R. Schlögl, M. Behrens, R. Horn, Investigating dry reforming of methane with spatial reactor profiles and particle ‐ resolved CFD simulations, AIChE J. 62 (2016) 4436–4452.

[56] N. Jurtz, M. Kraume, G.D. Wehinger, Advances in fixed-bed reactor modeling using particle-resolved computational fluid dynamics (CFD), Rev. Chem. Eng. 35 (2019) 139–190.

[57] A. Cybulski, J.A. Moulijn, Monoliths in heterogeneous catalysis, Catal. Rev. Eng. 36 (1994) 179–270.

[58] M. Hettel, C. Diehm, H. Bonart, O. Deutschmann, Numerical simulation of a structured catalytic methane reformer by DUO: The new computational interface for OpenFOAM® and DETCHEM^{TM}, Catal. Today. 258 (2015) 230–240.

[59] P. Inbamrung, T. Sornchamni, C. Prapainainar, S. Tungkamani, P. Narataruksa, G.N. Jovanovic, Modeling of a square channel monolith reactor for methane steam reforming, Energy. 152 (2018) 383–400.

[60] X. Cui, S.K. Kær, Two-dimensional thermal analysis of radial heat transfer of monoliths in small-scale steam methane reforming, Int. J. Hydrogen Energy. 43 (2018) 11952–11968.

[61] L. Giani, G. Groppi, E. Tronconi, Mass-transfer characterization of metallic foams as supports for structured catalysts, Ind. Eng. Chem. Res. 44 (2005) 4993–5002.

[62] K. Pangarkar, T.J. Schildhauer, J.R. van Ommen, J. Nijenhuis, F. Kapteijn, J.A. Moulijn, Structured packings for multiphase catalytic reactors, Ind. Eng. Chem. Res. 47 (2008) 3720–3751.

[63] E. Bianchi, T. Heidig, C.G. Visconti, G. Groppi, H. Freund, E. Tronconi, An appraisal of the heat transfer properties of metallic open-cell foams for strongly exo-/endo-thermic catalytic processes in tubular reactors, Chem. Eng. J. 198 (2012) 512–528.

[64] E. Bianchi, W. Schwieger, H. Freund, Assessment of Periodic Open Cellular Structures for Enhanced Heat Conduction in Catalytic Fixed‐Bed Reactors, Adv. Eng. Mater. 18 (2016) 608–614.

[65] F. Lucci, A. Della Torre, G. Montenegro, R. Kaufmann, P.D. Eggenschwiler, Comparison of geometrical, momentum and mass transfer characteristics of real foams to Kelvin cell lattices for catalyst applications, Int. J. Heat Mass Transf. 108 (2017) 341–350.

[66] C. Busse, H. Freund, W. Schwieger, Intensification of heat transfer in catalytic reactors by additively manufactured periodic open cellular structures (POCS), Chem. Eng. Process. Intensif. 124 (2018) 199–214.

[67] V. Papetti, P.D. Eggenschwiler, A. Della Torre, F. Lucci, A. Ortona, G. Montenegro, Additive Manufactured open cell polyhedral structures as substrates for automotive catalysts, Int. J. Heat Mass Transf. 126 (2018) 1035–1047.

[68] M. Kramer, M. McKelvie, M. Watson, Additive Manufacturing of Catalyst Substrates for Steam–Methane Reforming, J. Mater. Eng. Perform. 27 (2018) 21–31.

[69] STAR-CCM+ User Mannul v. 12.06, 2018.

[70] M. Lacroix, P. Nguyen, D. Schweich, C.P. Huu, S. Savin-Poncet, D. Edouard, Pressure drop measurements and modeling on SiC foams, Chem. Eng. Sci. 62 (2007) 3259–3267.

[71] Z. Wu, C. Caliot, G. Flamant, Z. Wang, Coupled radiation and flow modeling in ceramic foam volumetric solar air receivers, Sol. Energy. 85 (2011) 2374–2385.

[72] M.A. Schuetz, L.R. Glicksman, A basic study of heat transfer through foam insulation, J. Cell. Plast. 20 (1984) 114–121.

[73] STAR-CCM+ Theory Guid v. 12.06, Siemens AG, 2018.

[74] S. Wang, G.Q. (Max) Lu*, A comprehensive study on carbon dioxide reforming of methane over Ni/γ-Al2O3 catalysts, Ind. Eng. Chem. Res. 38 (1999) 2615–2625.

[75] R. Rubin, J. Karni, J. Yeheskel, Chemical kinetics simulation of high temperature hydrocarbons reforming in a solar reactor, in: ASME 2003 Int. Sol. Energy Conf., American Society of Mechanical Engineers, 2003: pp. 111–120.

[76] F. Wang, Y. Shuai, Z. Wang, Y. Leng, H. Tan, Thermal and chemical reaction performance analyses of steam methane reforming in porous media solar thermochemical reactor, Int. J. Hydrogen Energy. 39 (2014) 718–730.

[77] STAR-CCM+ Material Databases, Siemens AG, 2017.

[78] P. Furler, A. Steinfeld, Heat transfer and fluid flow analysis of a 4 kW solar thermochemical reactor for ceria redox cycling, Chem. Eng. Sci. 137 (2015) 373–383.

[79] V.P. Nicolau, M. Borges, L.M.S. Silva, Radiative properties of glass and coatings, in: 3rd Eur. Conf. Energy Perform. Indoor Clim. Build., 2002: pp. 835–840.

[80] P. Richet, Y. Bottinga, L. Denielou, J.P. Petitet, C. Tequi, Thermodynamic properties of quartz, cristobalite and amorphous SiO2: drop calorimetry measurements between 1000 and 1800 K and a review from 0 to 2000 K, Geochim. Cosmochim. Acta. 46 (1982) 2639–2658.

[81] S. Andre, A. Degiovanni, A theoretical study of the transient coupled conduction and radiation heat transfer in glass: phonic diffusivity measurements by the flash technique, Int. J. Heat Mass Transf. 38 (1995) 3401–3412.

[82] S. Sokolov, E. V Kondratenko, M.-M. Pohl, A. Barkschat, U. Rodemerck, Stable low-temperature dry reforming of methane over mesoporous La2O3-ZrO2 supported Ni catalyst, Appl. Catal. B Environ. 113 (2012) 19–30.

[83] D. Pakhare, J. Spivey, A review of dry (CO 2) reforming of methane over noble metal catalysts, Chem. Soc. Rev. 43 (2014) 7813–7837.

SECTION

2. CONCLUSIONS AND FUTURE WORK

2.1. CONCLUSIONS

A novel partition-cavity reactor is developed for solar thermochemical processes. By introducing the transparent partition structure, the reactor cavity is divided into the non-reactive domain and reactive domain. Incoming cold fluid can be preheated in the non-reactive domain before it enters the reactive domain. Additionally, the transparent partition can elevate the heat achievement of weak radiative absorption gases from heat convection between solid and fluid without apparent radiative flux loss for particles. With this improved reactor design, high-temperature CeO_2 reduction process is studied based on the operating conditions and particle parameters via CFD. The results reveal that the particle specific surface area is a dominant factor that affects the oxygen evolution rate. Under the same particle size condition, temperature strongly influence the reduction rate due to the reaction mechanism. Therefore, a higher particle specific surface area with loosing packing under a high radiant flux is appropriate to increase the CeO_2 reduction rate.

The reactor geometry determines the momentum and heat transfer in the reactor. A group of geometric factors of the partition-cavity reactor are studied to optimize reactor performances. Since the radiative distribution also influences the temperature profile in the reactor, a conceptual parabolic dish solar collector was designed to concentrate solar power by Monte Carlo ray tracing in Soltrace. The concentrated radiant flux results were introduced as a radiative flux boundary condition in CFD. The fluid and

particle surface temperature depend on the conjugate heat transfer, but the particle bulk temperature lies with radiant flux. Concentrated radiant fluxes lead to uneven flux distributions on the receiving surface. A larger receiving area can derive a lower but more uniform radiative flux, which manifests on a higher average temperature distribution.

The periodic open cellular structured catalyst is a novel monolith catalyst that is beneficial on the heat and mass transfer. The heat transfer performances were investigated with varying the strut thickness for three types of POCS in the sliced solar partition-cavity thermochemical reactor. The results indicate that the heat conduction of the strut plays the most important role in the temperature distribution in the catalyst region. Under the same void fraction, the POCS with the higher specific surface area is favorable to obtain a higher temperature. Under the same specific area, a larger void fraction is beneficial for the temperature distribution.

The influences of the operating conditions of the dry reforming of methane were tested in the solar thermochemical reactor with different POCS catalysts. The slow gas flow rate is favorable to derive a higher reaction temperature which leads to a higher methane conversion. Considering energy efficiency, the radiant flux has an optimum value. After that value, the methane conversion increase is finite. Due to the RWGS side reaction, the excess of the CO_2 is in favor of improving the methane conversion. Under the assumption of equal concentration of the catalyst active sites, the methane conversions of studied POCS catalysts have little difference, as the site concentration is not considered in the reaction expressions.

2.2. FUTURE WORK

As the cylindrical cavity inner surface is not beneficial to derive even radiant flux distribution, the conical inner surface is considered under concentrated radiant flux. As the conical angle is related to solar collector rim angle, the next work is focused on improving the current partition-cavity reactor with a conical inner surface with optimized radiant flux and temperature distribution. Besides, the current reaction temperature does not reach estimated due to the low solar power input. Hence, an improvement on the collector design should also be considered to concentrate a higher power.

Since the current reaction mechanism has a restriction to reveal the influences of different types of the POCS catalysts, the next step is implementing the microkinetics of the DRM reaction, including site reactions, in the solar thermochemical reactor. The relation between site concentration and the specific surface area should be established to take the structural factors into consideration.

In the present design of the solar thermochemical reactor, the structures of the POCS limit the radiative transfer in the catalyst region. The POCS catalysts with gradual changes of the lattice sizes are promising to improve the uniformity of the temperature distribution in the radial direction. The study will focus on the correlation of the lattice size distribution with the concentrated solar radiation directions.

Furthermore, the experimental study of the solar thermochemical process is necessary to validate the numerical results and improve the simulation models. The future work should focus on the implementation of the two-step redox cycles and the dry reforming of methane experimentally.

BIBLIOGRAPHY

1. Welte, M., *Solar Particle-Transport Reactor Technology for the Thermal Reduction of Ceria*. 2017, ETH Zurich.

2. Parida, B., S. Iniyan, and R. Goic, *A review of solar photovoltaic technologies.* Renewable and sustainable energy reviews, 2011. **15**(3): p. 1625-1636.

3. Steinfeld, A., *Solar thermochemical production of hydrogen—a review.* Solar energy, 2005. **78**(5): p. 603-615.

4. Duffie, J.A. and W.A. Beckman, *Solar engineering of thermal processes*. 2013: John Wiley & Sons.

5. Yadav, D. and R. Banerjee, *A review of solar thermochemical processes.* Renewable and Sustainable Energy Reviews, 2016. **54**: p. 497-532.

6. Baykara, S. and E. Bilgen, *An overall assessment of hydrogen production by solar water thermolysis.* International journal of hydrogen energy, 1989. **14**(12): p. 881-891.

7. Baykara, S., *Experimental solar water thermolysis.* International Journal of Hydrogen Energy, 2004. **29**(14): p. 1459-1469.

8. Graves, C., et al., *Sustainable hydrocarbon fuels by recycling CO2 and H2O with renewable or nuclear energy.* Renewable and Sustainable Energy Reviews, 2011. **15**(1): p. 1-23.

9. Steinfeld, A., *Solar hydrogen production via a two-step water-splitting thermochemical cycle based on Zn/ZnO redox reactions.* International Journal of Hydrogen Energy, 2002. **27**(6): p. 611-619.

10. Palumbo, R., et al., *The production of Zn from ZnO in a high-temperature solar decomposition quench process—I. The scientific framework for the process.* Chemical Engineering Science, 1998. **53**(14): p. 2503-2517.

11. Loutzenhiser, P.G. and A. Steinfeld, *Solar syngas production from CO2 and H2O in a two-step thermochemical cycle via Zn/ZnO redox reactions: Thermodynamic cycle analysis.* international journal of hydrogen energy, 2011. **36**(19): p. 12141-12147.

12. Stamatiou, A., A. Steinfeld, and Z.R. Jovanovic, *On the effect of the presence of solid diluents during Zn oxidation by CO2.* Industrial & Engineering Chemistry Research, 2013. **52**(5): p. 1859-1869.

13. Sibieude, F., et al., *High temperature experiments with a solar furnace: the decomposition of Fe3O4, Mn3O4, CdO.* International journal of hydrogen energy, 1982. **7**(1): p. 79-88.

14. Nie, J., et al. *Numerical modeling of vapor condensation during cadmium quenching process in a solar receiver*. in *ASME 2009 3rd International Conference on Energy Sustainability collocated with the Heat Transfer and InterPACK09 Conferences*. 2009. American Society of Mechanical Engineers.

15. Charvin, P., et al., *Experimental study of SnO2/SnO/Sn thermochemical systems for solar production of hydrogen.* AIChE Journal, 2008. **54**(10): p. 2759-2767.

16. Abanades, S., et al., *Novel two-step SnO2/SnO water-splitting cycle for solar thermochemical production of hydrogen.* International Journal of Hydrogen Energy, 2008. **33**(21): p. 6021-6030.

17. Abanades, S., *CO2 and H2O reduction by solar thermochemical looping using SnO2/SnO redox reactions: Thermogravimetric analysis.* international journal of hydrogen energy, 2012. **37**(10): p. 8223-8231.

18. Leveque, G., et al., *Characterization of two-step tin-based redox system for thermochemical fuel production from solar-driven CO2 and H2O splitting cycle.* Industrial & Engineering Chemistry Research, 2014. **53**(14): p. 5668-5677.

19. Kang, K.-S., et al., *Novel two-step thermochemical cycle for hydrogen production from water using germanium oxide: KIER 4 thermochemical cycle.* international journal of hydrogen energy, 2009. **34**(10): p. 4283-4290.

20. Alxneit, I., *Assessing the feasibility of separating a stoichiometric mixture of zinc vapor and oxygen by a fast quench–Model calculations.* Solar Energy, 2008. **82**(11): p. 959-964.

21. Nakamura, T., *Hydrogen production from water utilizing solar heat at high temperatures.* Solar energy, 1977. **19**(5): p. 467-475.

22. Charvin, P., et al., *Two-step water splitting thermochemical cycle based on iron oxide redox pair for solar hydrogen production.* Energy, 2007. **32**(7): p. 1124-1133.

23. Gokon, N., et al., *Iron-containing yttria-stabilized zirconia system for two-step thermochemical water splitting.* Journal of Solar Energy Engineering, 2008. **130**(1): p. 011018.

24. Juan, L., L.S. Chen, and S.Y. Chen, *Study on the cycle decomposition of CO2 over NiCr0. 08Fe1. 92O4 and the microstructure of products.* Materials chemistry and physics, 2007. **105**(1): p. 122-126.

25. Abanades, S. and H.I. Villafan-Vidales, *CO2 and H2O conversion to solar fuels via two-step solar thermochemical looping using iron oxide redox pair.* Chemical engineering journal, 2011. **175**: p. 368-375.

26. Stamatiou, A., P. Loutzenhiser, and A. Steinfeld, *Solar syngas production via H2O/CO2-splitting thermochemical cycles with Zn/ZnO and FeO/Fe3O4 redox reactions.* Chemistry of materials, 2009. **22**(3): p. 851-859.

27. Muhich, C.L., et al., *Efficient generation of H2 by splitting water with an isothermal redox cycle.* Science, 2013. **341**(6145): p. 540-542.

28. Scheffe, J.R., J. Li, and A.W. Weimer, *A spinel ferrite/hercynite water-splitting redox cycle.* International Journal of Hydrogen Energy, 2010. **35**(8): p. 3333-3340.

29. Arifin, D., et al., *CoFe 2 O 4 on a porous Al 2 O 3 nanostructure for solar thermochemical CO 2 splitting.* Energy & Environmental Science, 2012. **5**(11): p. 9438-9443.

30. Coker, E.N., et al., *Ferrite-YSZ composites for solar thermochemical production of synthetic fuels: in operando characterization of CO2 reduction.* Journal of Materials Chemistry, 2011. **21**(29): p. 10767-10776.

31. Gokon, N., et al., *Monoclinic zirconia-supported Fe3O4 for the two-step water-splitting thermochemical cycle at high thermal reduction temperatures of 1400–1600° C.* International Journal of Hydrogen Energy, 2009. **34**(3): p. 1208-1217.

32. Kodama, T., et al., *Thermochemical hydrogen production by a redox system of ZrO2-supported Co (II)-ferrite.* Solar Energy, 2005. **78**(5): p. 623-631.

33. Kodama, T., Y. Nakamuro, and T. Mizuno, *A two-step thermochemical water splitting by iron-oxide on stabilized zirconia.* Journal of solar energy engineering, 2006. **128**(1): p. 3-7.

34. Chueh, W.C. and S.M. Haile, *A thermochemical study of ceria: exploiting an old material for new modes of energy conversion and CO2 mitigation.* Philosophical Transactions of the Royal Society of London A: Mathematical, Physical and Engineering Sciences, 2010. **368**(1923): p. 3269-3294.

35. Panlener, R., R. Blumenthal, and J. Garnier, *A thermodynamic study of nonstoichiometric cerium dioxide.* Journal of Physics and Chemistry of Solids, 1975. **36**(11): p. 1213-1222.

36. Scheffe, J.R. and A. Steinfeld, *Oxygen exchange materials for solar thermochemical splitting of H2O and CO2: a review.* Materials Today, 2014. **17**(7): p. 341-348.

37. Scheffe, J.R., D. Weibel, and A. Steinfeld, *Lanthanum–strontium–manganese perovskites as redox materials for solar thermochemical splitting of H2O and CO2.* Energy & Fuels, 2013. **27**(8): p. 4250-4257.

38. McDaniel, A.H., et al., *Sr-and Mn-doped LaAlO 3− δ for solar thermochemical H 2 and CO production.* Energy & Environmental Science, 2013. **6**(8): p. 2424-2428.

39. Jiang, Q., et al., *Thermochemical CO2 splitting reaction with supported LaxA1− xFeyB1− yO3 (A= Sr, Ce, B= Co, Mn; 0⩽ x, y⩽ 1) perovskite oxides.* Solar energy, 2014. **103**: p. 425-437.

40. Chueh, W.C. and S.M. Haile, *Ceria as a thermochemical reaction medium for selectively generating syngas or methane from H2O and CO2.* ChemSusChem, 2009. **2**(8): p. 735-739.

41. Furler, P., J.R. Scheffe, and A. Steinfeld, *Syngas production by simultaneous splitting of H2O and CO 2 via ceria redox reactions in a high-temperature solar reactor.* Energy & Environmental Science, 2012. **5**(3): p. 6098-6103.

42. Furler, P., et al., *Thermochemical CO 2 splitting via redox cycling of ceria reticulated foam structures with dual-scale porosities.* Physical Chemistry Chemical Physics, 2014. **16**(22): p. 10503-10511.

43. Marxer, D., et al., *Demonstration of the entire production chain to renewable kerosene via solar thermochemical splitting of H2O and CO2.* Energy & Fuels, 2015. **29**(5): p. 3241-3250.

44. Le Gal, A., S. Abanades, and G. Flamant, *CO2 and H2O splitting for thermochemical production of solar fuels using nonstoichiometric ceria and ceria/zirconia solid solutions.* Energy & Fuels, 2011. **25**(10): p. 4836-4845.

45. Le Gal, A., et al., *Reactivity of doped ceria-based mixed oxides for solar thermochemical hydrogen generation via two-step water-splitting cycles.* Energy & fuels, 2013. **27**(10): p. 6068-6078.

46. Takacs, M., et al., *Oxygen nonstoichiometry, defect equilibria, and thermodynamic characterization of LaMnO3 perovskites with Ca/Sr A-site and Al B-site doping.* Acta Materialia, 2016. **103**: p. 700-710.

47. McNaughton, R. and W. Stein, *Improving efficiency of power generation from solar thermal natural gas reforming.* 2009.

48. Gokon, N., et al., *Double-walled reformer tubes using high-temperature thermal storage of molten-salt/MgO composite for solar cavity-type reformer.* international journal of hydrogen energy, 2009. **34**(17): p. 7143-7154.

49. Abanades, S., H. Kimura, and H. Otsuka, *Hydrogen production from thermo-catalytic decomposition of methane using carbon black catalysts in an indirectly-irradiated tubular packed-bed solar reactor.* International Journal of Hydrogen Energy, 2014. **39**(33): p. 18770-18783.

50. Lichty, P., et al., *Atomic layer deposited thin film metal oxides for fuel production in a solar cavity reactor.* international journal of hydrogen energy, 2012. **37**(22): p. 16888-16894.

51. Bader, R., et al., *Design of a solar reactor to split CO2 via isothermal redox cycling of ceria.* Journal of Solar Energy Engineering, 2015. **137**(3): p. 031007.

52. Villermaux, J., *Les réacteurs chimiques solaires.* Entropie, 1979. **85**: p. 25-31.

53. Alonso, E. and M. Romero, *Review of experimental investigation on directly irradiated particles solar reactors.* Renewable and sustainable energy reviews, 2015. **41**: p. 53-67.

54. Steinfeld, A., et al., *A solar chemical reactor for co-production of zinc and synthesis gas.* Energy, 1998. **23**(10): p. 803-814.

55. Nikulshina, V., et al., *CO2 capture from air and co-production of H2 via the Ca (OH) 2–CaCO3 cycle using concentrated solar power–Thermodynamic analysis.* Energy, 2006. **31**(12): p. 1715-1725.

56. Kogan, M. and A. Kogan, *Production of hydrogen and carbon by solar thermal methane splitting. I. The unseeded reactor.* International Journal of Hydrogen Energy, 2003. **28**(11): p. 1187-1198.

57. KANEKO, H. *Two-step water splitting with concentrated solar heat using rotary-type solar furnace*. in *13th Solar PACES International Symposium, SolarPaces, Seville, Spain, June 20-23, 2006*. 2006.

58. Hogan Jr, R.E., et al., *Innovative solar thermochemical water splitting*. 2008, Sandia National Laboratories.

59. Lapp, J., J.H. Davidson, and W. LipiĹ, *Heat transfer analysis of a solid-solid heat recuperation system for solar-driven nonstoichiometric redox cycles.* Journal of Solar Energy Engineering, 2013. **135**(3): p. 031004.

60. Chambon, M., S. Abanades, and G. Flamant, *Thermal dissociation of compressed ZnO and SnO2 powders in a moving ‐front solar thermochemical reactor.* AIChE Journal, 2011. **57**(8): p. 2264-2273.

61. Müller, R., P. Haeberling, and R.D. Palumbo, *Further advances toward the development of a direct heating solar thermal chemical reactor for the thermal dissociation of ZnO (s).* Solar Energy, 2006. **80**(5): p. 500-511.

62. Abanades, S., P. Charvin, and G. Flamant, *Design and simulation of a solar chemical reactor for the thermal reduction of metal oxides: case study of zinc oxide dissociation.* Chemical Engineering Science, 2007. **62**(22): p. 6323-6333.

63. Chueh, W.C., et al., *High-flux solar-driven thermochemical dissociation of CO2 and H2O using nonstoichiometric ceria.* Science, 2010. **330**(6012): p. 1797-1801.

64. Bulfin, B., et al., *Analytical model of CeO2 oxidation and reduction.* The Journal of Physical Chemistry C, 2013. **117**(46): p. 24129-24137.

65. Zinkevich, M., D. Djurovic, and F. Aldinger, *Thermodynamic modelling of the cerium–oxygen system.* Solid State Ionics, 2006. **177**(11-12): p. 989-1001.

66. Ishida, T., et al., *Kinetics of thermal reduction step of thermochemical two-step water splitting using CeO2 particles: Master-plot method for analyzing non-isothermal experiments.* Energy Procedia, 2014. **49**: p. 1970-1979.

67. McDaniel, A.H., et al., *Nonstoichiometric perovskite oxides for solar thermochemical H2 and CO production.* Energy Procedia, 2014. **49**: p. 2009-2018.

68. Scheffe, J.R. and A. Steinfeld, *Thermodynamic analysis of cerium-based oxides for solar thermochemical fuel production.* Energy & Fuels, 2012. **26**(3): p. 1928-1936.

69. Bader, R., et al., *Unsteady Radiative Heat Transfer Model of a Ceria Particle Suspension Undergoing Solar Thermochemical Reduction.* Journal of Thermophysics and Heat Transfer, 2018. **33**(1): p. 63-77.

70. Lunsford, J.H., *Catalytic conversion of methane to more useful chemicals and fuels: a challenge for the 21st century.* Catalysis Today, 2000. **63**(2-4): p. 165-174.

71. Carvalho, L.S., et al., *Preparation and characterization of Ru/MgO-Al2O3 catalysts for methane steam reforming.* Catalysis Today, 2009. **142**(1-2): p. 52-60.

72. Wang, S., G. Lu, and G.J. Millar, *Carbon dioxide reforming of methane to produce synthesis gas over metal-supported catalysts: state of the art.* Energy & fuels, 1996. **10**(4): p. 896-904.

73. Zhou, W., et al., *The deactivation of Co/SiO2 catalyst for Fischer–Tropsch synthesis at different ratios of H2 to CO.* Fuel Processing Technology, 2006. **87**(7): p. 609-616.

74. Dry, M.E., *The fischer–tropsch process: 1950–2000.* Catalysis today, 2002. **71**(3-4): p. 227-241.

75. Sheu, E.J., E.M. Mokheimer, and A.F. Ghoniem, *A review of solar methane reforming systems.* international journal of hydrogen energy, 2015. **40**(38): p. 12929-12955.

76. Spiewak, I., C.E. Tyner, and U. Langnickel, *Applications of solar reforming technology*. 1993, Sandia National Labs., Albuquerque, NM (United States).

77. Wang, H. and E. Ruckenstein, *Carbon dioxide reforming of methane to synthesis gas over supported rhodium catalysts: the effect of support.* Applied Catalysis A: General, 2000. **204**(1): p. 143-152.

78. Carrara, C., et al., *Kinetic and stability studies of Ru/La 2 O 3 used in the dry reforming of methane.* Topics in Catalysis, 2008. **51**(1-4): p. 98-106.

79. Barroso-Quiroga, M.M. and A.E. Castro-Luna, *Catalytic activity and effect of modifiers on Ni-based catalysts for the dry reforming of methane.* International Journal of Hydrogen Energy, 2010. **35**(11): p. 6052-6056.

80. Schuurman, Y., et al., *Bifunctional pathways in the carbon dioxide reforming of methane over MgO-promoted Ru/C catalysts.* Catalysis letters, 2000. **66**(1-2): p. 33-37.

81. García-Diéguez, M., et al., *RhNi nanocatalysts for the CO2 and CO2+ H2O reforming of methane.* Catalysis Today, 2011. **172**(1): p. 136-142.

82. Steinhauer, B., et al., *Development of Ni-Pd bimetallic catalysts for the utilization of carbon dioxide and methane by dry reforming.* Applied Catalysis A: General, 2009. **366**(2): p. 333-341.

83. Pakhare, D. and J. Spivey, *A review of dry (CO 2) reforming of methane over noble metal catalysts.* Chemical Society Reviews, 2014. **43**(22): p. 7813-7837.

84. Kathiraser, Y., et al., *Kinetic and mechanistic aspects for CO2 reforming of methane over Ni based catalysts.* Chemical Engineering Journal, 2015. **278**: p. 62-78.

85. Gokon, N., et al. *Kinetics of CO2 reforming of methane by catalytically activated metallic foam absorber for solar receiver-reactors*. in *ASME 2008 2nd International Conference on Energy Sustainability collocated with the Heat Transfer, Fluids Engineering, and 3rd Energy Nanotechnology Conferences*. 2008. American Society of Mechanical Engineers.

86. Richardson, L.F., *IX. The approximate arithmetical solution by finite differences of physical problems involving differential equations, with an application to the stresses in a masonry dam.* Phil. Trans. R. Soc. Lond. A, 1911. **210**(459-470): p. 307-357.

87. Jeppson, R.W., *Limitations of some finite difference methods in solving the strongly nonlinear equation of unsaturated flow in soils.* 1972.

88. Courant, R., *Variational methods for the solution of problems of equilibrium and vibrations.* Bulletin of the American mathematical Society, 1943. **49**(1): p. 1-23.

89. Evans, M.W., F.H. Harlow, and E. Bromberg, *The particle-in-cell method for hydrodynamic calculations*. 1957, LOS ALAMOS NATIONAL LAB NM.

90. Gentry, R.A., R.E. Martin, and B.J. Daly, *An Eulerian differencing method for unsteady compressible flow problems.* Journal of Computational Physics, 1966. **1**(1): p. 87-118.

91. Bakker, A., *Lecture 5-Solution Methods Applied Computational Fluid Dynamics.* Lectures of Fluent Instructor, 2002: p. 41-43.

92. STAR-CCM+, *User Guide*. 2017.

93. Cundall, P.A. and O.D. Strack, *A discrete numerical model for granular assemblies.* geotechnique, 1979. **29**(1): p. 47-65.

94. Zhao, T., *Coupled DEM-CFD Analyses of Landslide-Induced Debris Flows*. 2017: Springer.

95. Luding, S., *Introduction to discrete element methods: basic of contact force models and how to perform the micro-macro transition to continuum theory.* European Journal of Environmental and Civil Engineering, 2008. **12**(7-8): p. 785-826.

96. Potyondy, D. and P. Cundall, *A bonded-particle model for rock.* International journal of rock mechanics and mining sciences, 2004. **41**(8): p. 1329-1364.

97. Cundall, P.A., *Evolution of elastic moduli in a deforming granular assembly.* S ELECTE, 1989: p. 59.

98. Jiang, M., H.-S. Yu, and D. Harris, *A novel discrete model for granular material incorporating rolling resistance.* Computers and Geotechnics, 2005. **32**(5): p. 340-357.

99. Peng, B., *Discrete element method (DEM) contact models applied to pavement simulation*. 2014, Virginia Tech.

100. Chandrasekhar, S., *Selected Papers, Volume 2: Radiative Transfer and Negative Ion of Hydrogen*. Vol. 2. 1989: University of Chicago Press.

101. Modest, M.F., *Radiative heat transfer*. 2013: Academic press.

102. Lathrop, K.D. and B.G. Carlson, *Discrete ordinates angular quadrature of the neutron transport equation*. 1964, Los Alamos Scientific Lab., N. Mex.

VITA

The author, Han Zhang was born in China. She entered Beijing University of Chemical Technology, China in 2008. She received her B.E degree in Chemical Engineering and Technology from Beijing University of Chemical Technology in July 2012. She earned her M.S. in Chemical Engineering from the University of Southern California in 2014. She received a Doctor of Philosophy degree in Chemical Engineering from the Missouri University of Science and Technology in May 2019. Her research focused on using the discrete element method (DEM) and the concept of additive manufacturing in the computational fluid dynamics (CFD) simulation of catalyst structures to improve the accuracy of radiation performances for the solar thermochemical processes.